

UNIVERSITY OF SOUTHERN QUEENSLAND



**Numerical Human Head Modelling and Investigation
for Precise tDCS Applications**

A Thesis Submitted by

Bo Song

Master, University of New South Wales, 2013

Bachelor, Henan University, 2011

For the award of

Doctor of Philosophy

2016

Copyright

By

Bo Song

2016

Abstract

As a non-invasive and sub-convulsive functional stimulation technique, transcranial direct current stimulation (tDCS) generates a relatively weak current intensity and applies the moderate current to the brain to modulate the level of cortical excitability. This neuromodulatory technique has been extensively used as a potential clinical treatment for various neuropsychiatric conditions, ranging from depression, addition to schizophrenia and Parkinson's disease. Recently, tDCS has also been researched as a promising alternative treatment to alleviate neuropathic pain of cancer patients.

The focus of this project is to numerically investigate the precise applications of tDCS based on a series of high resolution realistic human head model using finite element methods. Specifically, the influence of brain shift caused by gravity was firstly pre-validated using real shaped human head model. After that, this study focuses on the investigation of tDCS applications on the brain cancer patients in order to treat their neuropsychiatric conditions and neuropathic pain caused by the brain tumors. Thirdly, the role of blood vessels in shaping the induced current distributions within the cortex during tDCS was thoroughly investigated and addressed.

The outcomes of this project highlight the importance of head orientation during the clinical application of tDCS. The results also clear the safety concern in applying tDCS to the patients with brain cancer. In addition, this project provides positive supports on the introduction of brain blood vessels during the precise human head modelling for tDCS though considerable workload will be involved.

Certification of Dissertation

This thesis is entirely the work of ***Bo Song*** except where otherwise acknowledged. The work is original and has not previously been submitted for any other award, except where acknowledged.

Student and supervisors signatures of endorsement are held at USQ.

Associate Professor Yan Li

Principal Supervisor

Associate Professor Peng Wen

Associate Supervisor

Acknowledgement

My time at the University of Southern Queensland has been a challenging but rewarding learning experience and I would like to express my sincere gratitude to a number of people for their guidance and assistance.

Firstly I am extremely grateful to my supervisors A/Professor Yan Li, A/Professor Peng Wen and A/Professor Tony Ahfock for their unparalleled help, continuous encouragement and great patience. Without their invaluable suggestions, discussions and confidence in my work, it is impossible for me to complete my PhD program.

Apart from my supervisors, I would like to thank Dr. Salman Shahid for his help at the beginning of my program and Miss Marilia Oliveira for her helpful discussions. I would also like to acknowledge the technical and administrative supports from the Faculty of Health, Engineering and Sciences and the ICT Service team of USQ.

Last but certainly not the least, my special gratitude goes to my beloved family members, who have always been there for me with their unconditional love. Particular thanks goes to my wife Shuaifang (Rebecca) Wang for her consistent understanding and love.

List of related publications

The following papers, associated with this project and included in this dissertation, have been published or submitted for publication.

JOURNAL PAPERS

Song, B., Wen, P., Ahfock, T. and Li, Y., 2016, Numeric Investigation of Brain Tumor Influence on the Current Distributions during Transcranial Direct Current Stimulation. *IEEE Transactions on Biomedical Engineering*, 63(1), pp.176-187.

Shahid, S.S., Song, B., Salman, H., de Oliveira, M.M. and Wen, P., 2015, Use of electric field orientation as an index for estimating the contribution of model complexity in transcranial direct current stimulation forward head model development. *IET Science, Measurement & Technology*, 9(5), pp.596-605.

Wang, S., Zhu, G., Li, Y., Wen, P. and Song, B., 2014, Analysis of epileptic EEG signals with simple random sampling J48 algorithm. *International Journal of Bioscience, Biochemistry and Bioinformatics*, 4(2), p.78.

JOURNAL PAPERS SUBMITTED

Song, B., Wen, P., Ahfock, T. and Li, Y., The Impact of Lateral Head Orientations on the Current Distributions During tDCS, under review at *IET Science, Measurement & Technology*

Song, B., Wen, P., Ahfock, T. and Li, Y., A Gyri Precise Numerical Study of the Brain Blood Vessels System Influence on the Current Distributions during tDCS, under review at *NeuroImage*

Table of Contents

| | |
|--|-------------|
| ABSTRACT | III |
| CERTIFICATION OF DISSERTATION | IV |
| ACKNOWLEDGEMENT | V |
| LIST OF RELATED PUBLICATIONS | VI |
| TABLE OF CONTENTS..... | VII |
| LIST OF TABLES | XII |
| LIST OF FIGURES | XIII |
| 1. INTRODUCTION..... | 1 |
| 1.1. NEUROMODULATION AND COMPUTATIONAL TDCS | 1 |
| 1.2. RESEARCH OBJECTIVES | 4 |
| 1.3. RESEARCH SCOPE | 4 |
| 1.4. PROPOSED METHODOLOGY..... | 6 |
| 1.5. RESEARCH OUTCOMES..... | 6 |
| 1.6. DISSERTATION OUTLINE | 7 |
| 2. BRAIN STIMULATIONS AND ELECTRICAL THERAPIES | 10 |
| 2.1. HISTORICAL APPLICATIONS OF BRAIN STIMULATIONS..... | 10 |
| 2.2. CONTEMPORARY BRAIN STIMULATIONS TECHNIQUES..... | 13 |
| 2.2.1. Vagus Nerve Stimulation and Deep Brain Stimulation | 13 |
| 2.2.2. Transcranial Magnetic Stimulation and Electroconvulsive Therapy ... | 15 |
| 2.2.3. Transcranial Direct Current Stimulation..... | 17 |
| 2.3. ELECTRICAL THERAPEUTIC TREATMENTS FOR BRAIN TUMORS..... | 20 |
| 3. COMPUTATIONAL HUMAN HEAD MODELLING..... | 23 |

| | | |
|-----------|--|-----------|
| 3.1. | THE ADVANCEMENT OF HUMAN HEAD MODELLING | 23 |
| 3.1.1. | Early Analytical Human Head Models | 23 |
| 3.1.2. | Finite Element Spherical Human Head Models..... | 24 |
| 3.1.3. | Low-Resolution Realistic Human Head Models | 25 |
| 3.1.4. | High-Resolution Realistic Human Head Models..... | 26 |
| 3.2. | COMPUTATIONAL BIOELECTROMAGNETISM | 27 |
| 3.2.1. | Quasi-static Approximation | 27 |
| 3.2.2. | Infinitesimal Volume Conductor..... | 28 |
| 3.2.3. | Boundary Conditions Assignment | 30 |
| 3.3. | TDCS ORIENTATED COMPUTATIONAL HIGH RESOLUTION REALISTIC HUMAN HEAD MODELLING..... | 30 |
| 3.3.1. | MRI Image Processing..... | 31 |
| 3.3.2. | Electrode Montage Configurations | 35 |
| 3.3.3. | Electrical Conductivity Assignment | 36 |
| 3.3.4. | Mesh Generation and Computation | 36 |
| 3.3.5. | Workflow Summary..... | 38 |
| 4. | IMPACT OF BRAIN SHIFT ON CURRENT DISTRIBUTIONS | 39 |
| 4.1. | INTRODUCTION | 39 |
| 4.2. | METHODS | 41 |
| 4.2.1. | Quasi-static Approximation and Boundary Conditions..... | 41 |
| 4.2.2. | Conductivity Assignment and Geometric Dimensions | 42 |
| 4.2.3. | Electrode Montages and Stimulation Parameters | 43 |
| 4.2.4. | Finite Element Model Mesh and Data Computation | 43 |

| | | |
|-----------|--|-----------|
| 4.3. | RESULTS AND ANALYSIS..... | 44 |
| 4.3.1. | Analysis of Control Models for C3-C4 and C3-Fp2 Montages | 44 |
| 4.3.2. | Analysis of Models with C3-C4 Montage | 45 |
| 4.3.3. | Analysis of Models with C3-Fp2 Montage | 48 |
| 4.4. | DISCUSSIONS..... | 51 |
| 4.4.1. | Model Formulation | 51 |
| 4.4.2. | Comparison of Two Electrode Montages | 51 |
| 4.4.3. | Variations of Brain Displacement | 52 |
| 4.5. | CONCLUSIONS..... | 53 |
| 5. | INFLUENCE OF BRAIN TUMOR ON THE INDUCED CURRENT DISTRIBUTION PATTERN..... | 54 |
| 5.1. | INTRODUCTION | 55 |
| 5.2. | METHOD AND MODEL DESIGN..... | 56 |
| 5.2.1. | Image Segmentation and Mesh Generation | 56 |
| 5.2.2. | Electrode Montages and Tumor Locations | 57 |
| 5.2.3. | Electrical Properties and Tissue Conductivity | 58 |
| 5.2.4. | Simulation Parameters and Models Notation..... | 60 |
| 5.3. | COMPUTATIONS AND RESULTS | 61 |
| 5.3.1. | Influence of the RFL Brain Tumor | 62 |
| 5.3.2. | Influence of the RFL Brain Tumor | 67 |
| 5.4. | DISCUSSION | 71 |
| 5.4.1. | Variations of the Electrode Montage and Tumor Location | 71 |
| 5.4.2. | Tumors in Different Grades | 72 |

| | | |
|-----------|---|-----------|
| 5.4.3. | Current Limitations and Future Improvements..... | 72 |
| 5.5. | CONCLUSION..... | 73 |
| 6. | CURRENT DISTRIBUTIONS IN LOW GRADE BRAIN TUMOR | 74 |
| 6.1. | INTRODUCTION | 74 |
| 6.2. | MODEL DESIGN AND IMPLEMENTATION | 76 |
| 6.2.1. | Image Processing and Model Construction | 77 |
| 6.2.2. | Boundary Conditions and Electrical Properties | 78 |
| 6.3. | COMPUTATIONAL RESULTS..... | 79 |
| 6.4. | DISCUSSION | 81 |
| 6.5. | CONCLUSION..... | 81 |
| 7. | BRAIN BLOOD VESSEL MODELLING AND INFLUENCE ON CURRENT DISTRIBUTIONS..... | 83 |
| 7.1. | INTRODUCTION | 83 |
| 7.2. | BRAIN BLOOD VESSELS AND MODELLING | 84 |
| 7.2.1. | Image Registration and Segmentation | 85 |
| 7.2.2. | Montage Modelling and Electrical Property Assignment..... | 88 |
| 7.3. | GLOBAL INFLUENCE OF BLOOD VESSELS SYSTEM ON THE CEREBRAL CURRENT DISTRIBUTIONS | 91 |
| 7.4. | GYRI SPECIFIC INFLUENCE OF BLOOD VESSELS SYSTEM ON THE CURRENT DISTRIBUTIONS DURING TDCS | 94 |
| 7.5. | DISCUSSION | 96 |
| 7.5.1. | The Value and Cost of Brain Model Complexity | 96 |
| 7.5.2. | Limitations and Future Directions | 97 |
| 7.6. | CONCLUSION..... | 98 |
| 8. | CONCLUSIONS AND FUTURE DIRECTIONS..... | 99 |

| | |
|--|------------|
| 8.1. MAJOR CONTRIBUTIONS | 99 |
| 8.2. LIMITATIONS AND FUTURE DIRECTIONS | 100 |
| REFERENCES..... | 103 |

List of Tables

| | |
|---|----|
| Table 3.1 Scanning parameters of the MRI and MRA datasets..... | 32 |
| Table 3.2 Electrical conductivity of the normal tissue types included in the control models of this project..... | 37 |
| Table 4.1 Twenty-six models applied with different montages, head orientations and brain displacements. Notation M C3 – C4Right[0.5] represents a model applied with C3-C4 electric montage and right lateral head orientation while the brain displacement is 0.5 mm towards the ground..... | 40 |
| Table 4.2 Parameters assigned to all layers (Scalp dimension is derived from real subject)..... | 40 |
| Table 4.3 Four feature values of the current density distribution (A/m^2) in the brain surface of control models with C3-C4 and C3-Fp2 electrode configurations | 45 |
| Table 5.1 Conductivity of Electrodes and Tissues..... | 59 |
| Table 5.2 Conductivity of the Brain Tumor Conductivity assigned to the tumor confined regions in the control models and tumors components of different grades in other proposed models..... | 60 |
| Table 5.3 Notations for All Models | 61 |
| Table 6.1 Conductivity of the Cancerized Brain Tumor Components and Adjacent Edematous Tissues..... | 79 |
| Table 6.2 Boost rates of TA in the proposed models compared to their control model without edema..... | 79 |
| Table 7.1 Conductivity values for the electrodes and tissues..... | 89 |
| Table 7.2 The peak and TA values of the most influenced target brain gyri under all proposed tDCS montages after the modelling of blood vessels system..... | 95 |

List of Figures

| | |
|--|----|
| Figure 2.1 The first non-invasive therapeutic application of transcranial direction current brain stimulation.(Aldini 1804) | 10 |
| Figure 2.2 Early transcranial magnetic stimulation carried out by Silvanus Phillips Thompson (Thompson 1910)..... | 11 |
| Figure 2.3 Lucio Bini was applying ECT to the patient in the Rome University psychiatric clinic in 1940. (Shorter and Healy 2007) | 12 |
| Figure 2.4 Diagrammatic view of implanted VNS device (seizures.dolyan.com 2016) | 14 |
| Figure 2.5 X-Ray scan illustration of the implanted electrodes and wires of DBS in the skull in the treatment of Parkinson’s Disease (Hellerhoff 2016)..... | 15 |
| Figure 2.6 Demonstrations of the TMS device and working mechanisms. (Myers 2004, Neuroscience 2012)..... | 16 |
| Figure 2.7 Demonstrations of the ECT application coupling with other monitoring devices. (Myers 2010)..... | 17 |
| Figure 2.8 Illustrations of a typical tDCS components (left panel) and a classical electrode configuration with C3-Fp2 montage. (DaSilva, Volz et al. 2011, GmbH 2016) | 18 |
| Figure 2.9 Electrode locations of International 10-20 system for EEG recording (トマ トン 124 2010) | 20 |
| Figure 2.10 Illustration of the TTFs device worn on the head. (Moore 2016) | 22 |
| Figure 3.1 Early analytical model (Rush and Driscoll 1968)..... | 24 |
| Figure 3.2 Finite element spherical model (Drechsler, Wolters et al. 2009) | 24 |
| Figure 3.3 Low-resolution realistic model (Bai, Loo et al. 2012) | 26 |

| | |
|---|----|
| Figure 3.4 High-resolution realistic model (Shahid, Wen et al. 2013) | 26 |
| Figure 3.5 The net current out of the block in x direction | 28 |
| Figure 3.6 A simplified typical workflow in the development of high resolution realistic human head models. | 31 |
| Figure 3.7 Demonstrations of the final segmentation outcomes for the study of blood vessel systems. (A): Sagittal 2D slice view. (B): 3D render view | 33 |
| Figure 3.8 Demonstrations of the final segmentation for the study of brain tumors. (A): 3D render view of major human head tissue types. (B.1) - (B.9): 3D render views of inner brain structures..... | 33 |
| Figure 3.9 Demonstration of the manual correction operations..... | 34 |
| Figure 3.10 Electrode montages constructed in the study of blood vessel systems... | 35 |
| Figure 3.11 Electrode montages constructed in the study of brain tumors..... | 36 |
| Figure 3.12 Mesh generations for the studies of blood vessels system (A) and brain tumors (B). | 38 |
| Figure 4.1 Four layers included in this study (Image modified from (Blaus 2014)). | 40 |
| Figure 4.2 Electrode locations of International 10-20 system for EEG recording (Modified from (トマトシ 124 2010))..... | 40 |
| Figure 4.3 Electric potential distributions in the control models of C3-C4 (a) and C3-Fp2 (b) montages | 46 |
| Figure 4.4 Current density distributions on the brain surface of models with incremental brain displacements under C3-C4 electrode montage and right lateral head orientation (a: The distributions of three key features of current density; b: The fraction volume distributions of Log_{10} normalised current density) | 46 |
| Figure 4.5 Current density distributions on the brain surface of models with incremental brain displacements under C3-C4 electrode montage and left lateral head | |

orientation (a: The distributions of three key features of current density; b: The fraction volume distributions of Log_{10} normalised current density) 47

Figure 4.6 Plot of current density distributions on the brain surface of all the models listed in Table 4.1 and the right square pads in all four groups are the anode electrode placed at C3 location while the left ones are cathode electrode configured at C4 (G1, G2) and Fp2 (G3, G4) locations respectively 49

Figure 4.7 Current density distributions on the brain surface of models with incremental brain displacements under C3-Fp2 electrode montage and right lateral head orientation (a: The distributions of three key features of current density; b: The fraction volume distributions of Log_{10} normalised current density)..... 49

Figure 4.8 Current density distributions on the brain surface of models with incremental brain displacements under C3-Fp2 electrode montage and left lateral head orientation (a: The distributions of three key features of current density; b: The fraction volume distributions of Log_{10} normalised current density) 50

Figure 5.1 Illustration of a brain tumor (Highlighted with red circle) harbored in the left frontal lobe in transverse, sagittal and coronal planes. 55

Figure 5.2 Demonstration of tumor locations (Black green bulk: Tumor in RFL; Light green bulk: Tumor in LOL) and electrodes for five montages (Cathode electrode: blue pad in Fp2 and yellow pad in C4; Anode electrode: grey pad in F3, magenta pad in C3 and red pad in P3). 58

Figure 5.3 The current density J (A/m^2) distributions for simulations of the RFL brain tumor in different grades under C3-Fp2 montage. The first row (R1) shows the 3D brain plots and the 55-degree slice of right frontal brain (green plane) is shown in R2. R3 demonstrates the sliced tumor (black and red contours), normal surrounding GM (grey contour) and WM (magenta contour) whereas R4 zooms in the ROI (green squared region in R3). Black cones in R3 and R4 depict the current directions; the percentage statistics in R1 and R2 are the TA of GM and WM whereas the values in R3 and R4 represent TA and peak current density of tumor, normal adjacent GM and WM in their corresponding contour color..... 62

| | |
|--|----|
| Figure 5.4 Demonstration of the median current density (a), peak current density (b) of the normal GM and WM in the models with the RFL brain tumor under all proposed electrode configurations in unit $e-2 \text{ A/m}^2$ and $e-1 \text{ A/m}^2$ | 65 |
| Figure 5.5 Demonstration of the median current density (a), peak current density (b) of the adjacent GM (AdjGM) and adjacent WM (AdjWM) to the RFL brain tumor in the models configured with all proposed electrode montages in unit $e-2 \text{ A/m}^2$ and $e-1 \text{ A/m}^2$ | 65 |
| Figure 5.6 Demonstration of the peak and median current density within the RFL brain tumor in the model configured with different tumor grades and electrode montages. (Unit: $e-1 \text{ A/m}^2$) | 66 |
| Figure 5.7 The current density J (A/m^2) distribution for simulations of the LOL brain tumor in different grades under C3-Fp2 montage. (The notation follows the one used in Figure 5.3)..... | 67 |
| Figure 5.8 Demonstration of the median current density (a), peak current density (b) of the normal GM and WM in the models with the LOL brain tumor under all proposed electrode configurations in unit $e-2 \text{ A/m}^2$ and $e-1 \text{ A/m}^2$ | 68 |
| Figure 5.9 Demonstration of the median current density (a), peak current density (b) of the adjacent GM (AdjGM) and adjacent WM (AdjWM) to the LOL brain tumor in the models configured with all proposed electrode montages in unit $e-2 \text{ A/m}^2$ and $e-1 \text{ A/m}^2$ | 69 |
| Figure 5.10 Demonstration of the peak and median current density values within the LOL brain tumor in the model configured with different tumor grades and electrode montages. (Unit: $e-1 \text{ A/m}^2$)..... | 70 |
| Figure 6.1 Demonstration of brain tumor (renal cell brain metastasis) and extensive surrounding edema from post-contrast T1 weighted MRI scan (www.aboutcancer.com 2016) | 74 |

Figure 6.2 Demonstration of brain tumor (metastatic lung carcinoma) and extensive peritumoral brain edema from human brain coronal slice with enlarge view of the region of interest. This image is modified from (Agamanolis 2016)..... 75

Figure 6.3 Demonstration of current density J (A/m^2) within the brain tumor tissues and surrounding edematous tissues under all the proposed electrode configurations in the control and proposed models. The number below each slice is the maximum peak current density among the tumor and adjacent tissues (they are unanimously from CGM due to its high conductivity). 80

Figure 7.1 The image processing work flow for blood vessels segmentation. (A): The original MRA image. (B): The filtered MRA image generated by Frangi filter (present with default boundary range values). (C): The original MRA was registered to T1-MRI using both rigid and landmark registration approaches. (D): The filtered MRA image was registered to T1-MRI using the transform matrix obtained from operations in (C). (E): The final segmentation result of blood vessels (further tuning was applied to the filtered and registered MRA image). 85

Figure 7.2 The demonstration of key features from the constructed models in this study. (A): The preliminary segmentation result of major intracranial blood vessel obtained without tuning operations. (B): The final segmentation outcome of blood vessels system within the proposed human head models (red mask: intracranial blood vessel obtained after tuning, yellow mask: blood vessels in the eye organ; blue mask: other extracranial blood vessel in the scalp). 86

Figure 7.3 The demonstration of tDCS montages selected in this study. 88

Figure 7.4 The illustration of current density distributions under all the proposed electrode montages. The first two columns are the demonstrations for the current density distribution patterns within the brain of the control and proposed models while the third column particularly presents the blood vessels system from the proposed model. The fourth and fifth columns are the sliced brain of the control and posed models, which are shown as grey plants in the first two columns. The numbers in the first two columns are the TA changing rates of GM (black color) and WM (grey color)

while the numbers in the last two columns are the TA changing rates of the inner brain (yellow color) and hindbrain (green color) structures, respectively. 90

Figure 7.5 The peak, median and TA values of the current density within WM and GM in all models. 92

Figure 7.6 The peak, median and TA values of the current density within the inner brain and hindbrain in all models. 93

Figure 7.7. The TA (%) of cerebral lobes for all montages with contrast of the control and proposed groups. The underlined numbers over the paired columns are the boosting rate of TA for each lobe region under the proposed electrode configuration when the blood vessels system was considered. 94

1. INTRODUCTION

Electrical associated neuromodulation is an ancient technique with notable history and it can date back to 46 AD when Roman physician utilized the bioelectric discharge generated by the fishes possessing electric organs to alleviate headache symptoms, which was subsequently extended as a remedy for the treatment of seizures, depression and pain until the beginning of ninetieth century (Kellaway, 1946, Rossi, 2003, Sironi, 2011). After numerous rudimentary experiments on animals and pioneering studies of human trials in the followed two centuries, many novel electrical brain stimulation techniques have been developed and became widely known in the treatment of various neurological diseases as well as in the enhancement of motor and cognitive functions (George and Aston-Jones, 2010, Clark and Parasuraman, 2014, Hoy and Fitzgerald, 2010, Blank, 2016). Among these techniques, tDCS is one of the most prominent techniques and continual studies were carried out to explore its mechanisms and applications. At the same time, a proliferation of analytical and computational human head models based on finite element method (FEM) for tDCS were developed with varied model complexity in the representation of anatomical features, which were proposed during the investigations of the induced current distribution patterns within the brain to explore the underlying mechanisms and provide meaningful guidance for the clinical trials (Rush and Driscoll, 1968, Miranda et al., 2006, Wagner et al., 2007a, Sadleir et al., 2010, Bai et al., 2014, Song et al., 2016b, Grandori and Rossini, 1988, Weaver et al., 1976, Saypol et al., 1992).

1.1. Neuromodulation and Computational tDCS

Transcortically applied weak electrical current has long been administrated as a promising approach in the modulation of behavioural activities and cortical excitabilities in many early animal experiments and human involved studies (Olds and Milner, 1954, Reynolds, 1969, Goddard et al., 1969, CLARK and WARD, 1948, Harris, 1937, Richardson and Akil, 1977, Doty, 1969, Delgado et al., 1954). After continual development, particularly in the past three decades, it has evolved several clinically approved and trailing approaches, including electroconvulsive therapy (ECT), vagus nerve stimulation (VNS), transcranial magnetic stimulation (TMS),

deep brain stimulation (DBS), transcranial alternating current stimulation (tACS), tDCS and etc. (Abrams, 2002, Schachter and Saper, 1998, Wassermann, 1998, Mayberg et al., 2005, Antal et al., 2008a, Gandiga et al., 2006). Those techniques were generally reported as encouraging treatments for a wide range of neuropsychiatric disorders, ranging from seizure, major depression, Parkinson's disease to headache and pain perception (Krystal and Weiner, 1994, Marangell et al., 2002, O'Reardon et al., 2007, Berney et al., 2002, Boggio et al., 2006b, Magis et al., 2012, Antal et al., 2008b, Gungor and Empting, 2016). In addition, electrical based therapies were also proposed in combination with other forms of traditional treatments, like electroporation in gene transfer, electrochemotherapy (EChT) in the antitumor drug delivery, tumor treating fields (TTFs) and low level direct current therapy (DCT) in tumor growth control applications (Belehradek et al., 1993, Omar, 2014, Neumann et al., 1982, Griffin et al., 1994).

tDCS is one of the most promising non-invasive brain modulation techniques. It was under intensive research especially in the past three decades. At the same time, with the advancement of imaging techniques in Magnetic Resonance Angiogram (MRA), Diffusion Tensor Imaging (DTI) and Magnetic Resonance Imaging (MRI), a series of image based multimodal high resolution realistic human head models containing detailed anatomical features were constructed for precision requested studies of tDCS in exploring the current distribution within the cortex and specific regions of interest. Such high resolution human head models are significant for the customized stimulation therapies because those models optimize the stimulation parameters to avoid unexpected outcomes, especially for the patients with particular physical conditions, like brain lesions, skull defect and etc. (Parazzini et al., 2016, Datta et al., 2011, Song et al., 2016a, Datta et al., 2010, Truong et al., 2013, Hesse et al., 2007).

Though high resolution realistic human head models utilized in the most recent studies already achieved unprecedented accuracy in the history of human head modelling, they are still far from perfect due to the unreliable assignment of tissue electrical properties, almost ineluctable simplifications in some compartment classification and tissue segmentations. So far, considerable attempts have been made in assigning anisotropic conductivities to the skull, muscle, WM in order to improve the tissue conductivity assignment. A general trend could also be observed in overcoming the simplification

by enhancing the anatomical complexities of high resolution realistic human head models. Therefore, building multimodal high resolution realistic human head models with increasing model complexities are expected to address the precision required tDCS applications and studies.

However, building such models takes considerable work in both model construction and computations, especially when it is designed to accommodate extra brain compartments and tissue types or proposed to consider customized patients and conditional scenarios, or other precision applications of tDCS. Though the majority of most recent studies showed preference in such models with higher model complexity and chose to undertake the extra workload burden, warnings were still issued to the relationship between increasing the model complexity and yielding the model accuracy with clinical guidance meaning (Bikson et al., 2012a, Bikson et al., 2012b, Bikson et al., 2015). Even so, no negative statement was ever made to object the attempts of improving model complexity for precision application of tDCS and it is still of great value for both clinical and academic studies of precision required in tDCS applications as long as the model complexity and model accuracy could be rationally balanced.

Therefore, multimodal high resolution realistic human head models with reasonable model complexities are still under demand for the studies of precision applications of tDCS, and on the other hand, the value and cost concern on increasing the model complexity need to be addressed before setting a new baseline for the model complexity requirement. Those attempts should have both clinical and academic meaning in setting the model complexity baseline for precisions required in stimulation studies.

1.2. Research Objectives

The focus of this project is to numerically investigate the precise applications of tDCS based on a series of high resolution realistic human head models using finite element methods. The objectives of this project are multi-folded.

The first objective is to pre-validate the influence of brain shift caused by the gravity on the current distributions during tDCS using a series of real shaped human head models with incremental brain shift according to the proposed head orientations.

The second objective is to investigate the current distribution patterns within the cortex when tDCS is applied to the patients with brain tumors, which will answer the safety concerns and further understand the influence of brain tumors on the current distributions.

Thirdly, the role of blood vessels in defining the current distributions within the cortex during tDCS is investigated in this project. The value and cost by introducing the blood vessels for precise tDCS modelling is also addressed.

Fourthly, the long term of this project is to develop a framework for constructing MRI and MRA image based multimodal high resolution human head models with gyri precision.

1.3. Research Scope

tDCS is still not a precise neuromodulation technique and some researchers already challenged the reported promising outcomes of tDCS experiments as the case dependent positive results could be cancelled out by each other (Horvath et al., 2015b, Horvath et al., 2015a).. What is more, as a non-invasive brain stimulation technique, the present of skull and the customer depended variations of brain gyri also make it difficult to carry out precise application of tDCS according to customized scenarios (Antal et al., 2015, Benwell et al., 2015, Li et al., 2015, Fertoni and Miniussi, 2016). As a consequence, inter-individual factors are expected to be included in the studies of tDCS and the need for customized tDCS application is highlighted. Meanwhile, MRI based high resolution realistic human head model is increasingly recognized as a

standard solution to guide and optimize the precise application of tDCS, especially when the patients are in particular physical conditions. Therefore, considerable scope is left to the development of tDCS modelling for precise application and in particular, high resolution realistic human head model with reasonable model complexities are highly desired.

It is easy to understand that most of the tDCS applications are carried out when the subjects are seated with no lateral head orientations. But for most current MRI based modelling studies of tDCS, their MRI datasets are obtained while the subject is laying down in the MRI scanning machine. The necessities of brain shift correction for tDCS modelling have never been raised though it is reported to have potential influence on the neuromodulations. Consequently, apart from the motion corrections and anti-eddy effects steps, this study could contribute another fundamental step on whether brain shift corrections are necessary in tDCS application. In addition, increasingly more studies are using MRI machine compatible tDCS kits to carry out the real time studies of tDCS, which obtains the MRI dataset while the tDCS application is in progress. All these factors formed the research scope of head orientation investigations for tDCS modelling.

Considering that increasing the model complexity involves substantial more workload during the modelling and requires more computation resources, it is of significant value in balancing the value and cost before introducing any tissues as a new requirement and setting a new baseline of model complexity for the tDCS modelling and computation. So, the model complexity and cost are addressed in including and defining the role of blood vessels during tDCS modelling.

Validation of such high resolution realistic human head model based computational tDCS simulations was still reported as a research challenge because the unavailability of the in vivo measurements for the induced current distribution during tDCS. Such limitation could be another interesting research topic but it was not the focus of this project because the workflows for the model constructions and computations utilized in this project were already widely accepted by the peer reviewed works. Nonetheless, the detailed geometry information of the model and encapsulated tissues were also clearly presented for verification purposes.

1.4. Proposed Methodology

To explore the possible influence of brain shift caused by lateral head orientations during tDCS, a series of real shaped human head models are proposed for pre-validation purpose.

To address the precise application of tDCS on the patients with brain tumors and investigate the influence of brain tumors on the induced current distributions within the brain tumor and healthy cortex, a series of MRI derived high resolution realistic human head models configured with varied montages and inter-electrode distance, different tumor locations (superficial frontal lobe and buried occipital lobe) and tumor grades (I–IV) have been designed and investigated using FEM solvers.

Another set of high resolution realistic human head models based on MRI and MRA are constructed to study the precise influence of blood vessels in shaping the current distribution patterns within the brain and define its role in the model complexity.

1.5. Research Outcomes

Firstly, the influence of brain shift caused by head orientations during tDCS on the current distributions was pre-validated, the downward movement of brain caused by gravity showed its influence in the precision required tDCS modellings, and further detailed explorations based on high resolution realistic human head are required to precisely determine its role in different applications including tDCS. This pre-validation study points out the importance of head orientations during tDCS in defining the current distributions and the preliminary results also indicated the necessity of brain shift corrections for the MRI datasets obtained with lateral head orientations, especially when the dataset is acquired for precise modelling of tDCS applications.

Secondly, the precise application of tDCS on the patients with brain tumors were investigated for the first time in tDCS forward human head modelling and the presence of brain tumors in defining the induced current distribution patterns within the brain were studied in conjunction with tumors and tumor locations, which is a meaningful result for researchers and clinical doctors to modulate patients' neuropsychiatric conditions or control the acute and chronic pain caused by brain tumors.

Finally, the role of blood vessels in high resolution realistic human head modelling was defined and its influence on the current distributions during tDCS were investigated. The results showed that the blood vessels should not be ignored in the precise tDCS modelling studies, though considerable extra workload is expected. This finding highlighted the meaning of blood vessels system in multimodal high resolution realistic human head modellings and this work should set a new baseline of the model complexity for precise tDCS applications.

1.6. Dissertation Outline

This dissertation is organised into eight chapters. It starts with Chapter 1 Introduction, which provides an overview for the whole project and the entire dissertation. Chapter 2 and 3 introduce the big picture about human head modelling development and the work flow of multimodal high resolution realistic human head modelling in this study. Chapter 4 includes the exploration of the influence of head orientations during tDCS based on the real shaped human head model. Chapters 5 – 7 report the core work where we systematically investigate the precise application of tDCS on the patients with brain tumors and the introduction of blood vessels into high resolution realistic human head models. The conclusions are drawn and the future directions of this study are indicated in Chapter 8.

Chapter 1 provides an overview of the entire dissertation, which includes the broad background information of brain modulations and tDCS, the research objectives and corresponding methodologies proposed in this study, a summary of the research outcomes and implications in clinical trials and academic studies.

Chapter 2 focuses on literature review on the brain stimulation techniques (ECT, VNS, TMS, DBS, tACS and tDCS) and electrical treatments for brain tumors control (EChT, TTFs and DCT). A comprehensive literature review and comparison between tDCS and other brain stimulation techniques are also conducted in this chapter. In addition, the precise applications of tDCS on patients with brain tumors are also rationalized with feasible medical reasons.

Chapter 3 briefly describes the development of human head modelling for tDCS, ranging from the analytical model to the most sophisticated high resolution realistic

human models. As one of the most fundamental methodologies proposed in this study, a workflow chart for constructing high resolution realistic human head models is presented in this chapter. Furthermore, the electrical properties of human head tissues are considered as another crucial element in the simulations studies of tDCS and such information utilized in this study is also presented in Chapter 3.

Chapter 4 explores the influence of brain shift caused by gravity in shaping the outcomes of tDCS. In this chapter, a series of real shaped human head models are constructed to pre-validate such hypothesis. According to the simulation result, brain shift during tDCS influences the current distributions of tDCS and the head orientations should be considered during the precise application of tDCS. Meanwhile, considering that most of the current MRI datasets are obtained with lateral head orientations, corresponding image correction operations are expected to adjust the brain shift effects during the image processing procedures for tDCS modellings.

Chapter 5 investigates the influence of brain tumor on the induced current distribution patterns within the cortex and other regions of interest during tDCS. The work is carried out using a series of high resolution realistic human head models. These models were configured under five electrode montage (F3-Fp2, C3-C4, C3-Fp2, P3-C4 and P3-Fp2), two tumor locations (superficial right frontal lobe and buried left occipital lobe) and four tumor grades according to the World Health Organization classification (I–IV). Then, the proposed experiments are conducted in calculations and the results were obtained and analysed based on the tumor grades and locations in conjunction with proposed montages.

Chapter 6 is a further study of tDCS application on the patients with brain tumors which focuses on the low grade brain tumors and the current distribution patterns within the cancerized tissues (cancerized GM and cancerized WM) and surrounding edematous tissues (edematous GM and edematous WM). The detailed current distribution information on the proposed tumors is obtained and analysed, which defines the role of surrounding edema of brain tumors in shaping the current distributions during tDCS.

Chapter 7 focuses on the role of blood vessels in shaping the current distribution patterns during tDCS. A series of paired high resolution realistic human head models

with gyri precision are constructed with five electrode configurations (P4-P3, C3-C4, Oz-Cz, C3-Fp2 and Fp1-Oz) to define the role of the blood vessels in the high resolution realistic human head modelling. The value and cost concern on introducing this extra anatomical feature is also analysed and discussed in this chapter. The development of a framework for constructing MRI and MRA image based multimodal high resolution human head models with gyri precision is also included in this chapter.

Chapter 8 summarizes the whole work and draws conclusions. All the important results and outcomes obtained in this study are presented. The future directions of precise applications of tDCS are also indicated in the future work section.

2. BRAIN STIMULATIONS AND ELECTRICAL THERAPIES

As an antiquated technique with distinguished history records, electrical brain modulation technique was firstly documented in 46 AD when Roman physician applied the bioelectric discharge of the electric fish to treat human headaches. After approximately two-centaury's development, many innovative and contemporary brain stimulation techniques were evolved as promising remedies for the treatment of a broad range of neuropsychiatric disorders.

2.1. Historical Applications of Brain Stimulations

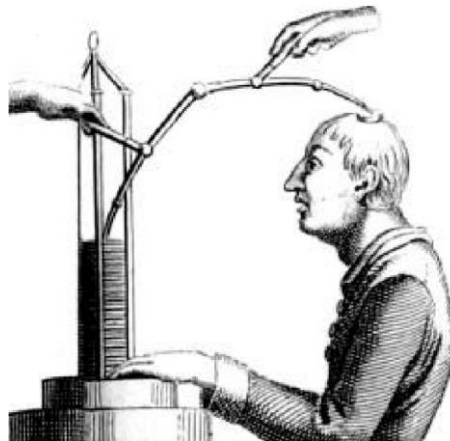


Figure 2.1 The first non-invasive therapeutic application of transcranial direct current brain stimulation.(Aldini, 1804)

In the middle of eighteenth century, Albrecht von Haller (1708-1777), a famous Swiss physiologist, emphasized that various human body tissues, nerves and muscles in particular, were sensitive to the electrical stimulations, which was agreed by several scientists from the same period. After pre-validation experiments on animals, Italian physician Luigi Aloisio Galvani (1737-1798) demonstrated and concluded that electricity can be an efficient and powerful stimulus for nerves and muscles. Later on, Galvani's nephew Giovanni Aldini (1762-1834) performed the first electrical stimulation on one hemisphere of the cerebral cortex in a sacrificed criminal and observed the contralateral facial grimaces, which led his famous conclusion that cortical surface could be electrically stimulated. Such findings provided positive

influence on the exploration of electricity as therapeutic alternations in the treatments of many neuropsychiatric disorders. As the pioneer of transcranial direct current brain stimulation, he then applied it to psychiatric patients, including those effected with depression, by stimulating the shaved parietal area. Figure 2.1 demonstrates the early form of tDCS. Such tDCS application was then extended to stimulate the whole cerebral cortex by Sir Victor Horsley (1888-1903) and further exploited by later researchers. (Arle and Shils, 2011, Bullock et al., 2006, Sironi, 2011, Parent, 2004)



Figure 2.2 Early transcranial magnetic stimulation carried out by Silvanus Phillips Thompson (Thompson, 1910).

From 1889, French physician and physicist, Jacques-Arsène d'Arsonval (1851-1940) did a series of experiments of the alternating current on the human body and explored the induced physiological influences on the human. Later in 1896, He reported the perceiving of flickering visual sensation when the head of a subject was placed in a strong time-varying magnetic fields, which was powered by a large coil with 32A alternating current in 42Hz. Such stimulation outcome of the retina was named as magnetophosphenes by Jacques and this stimulation was regarded as the first magnetic stimulation of the nervous system. Years later, Silvanus Phillips Thompson (1851-1916), the Fellow of Royal Society, investigated the influence of magnetic field on the brain and officially published his research on the visual sensation (magnetophosphenes) of electromagnetic filed in 1910. As show in Figure 2.2, Thompson carried out such study using himself as the experiment subject. In this experiment, the peak value of magnetic flux density was up to 140mT while the

frequency was 50Hz though recent studies pointed out that the stimulation of retina (magnetophosphenes) could be achieved by much weaker magnetic field (10mT magnetic flux density and 20Hz frequency). Owing to his pioneering work on magnetic stimulations, Thompson was deemed as the precursor of transcranial magnetic stimulation. (Thompson, 1910, Krawczyk and Łada-Tondyra, 2010, Malmivuo and Plonsey, 1995)

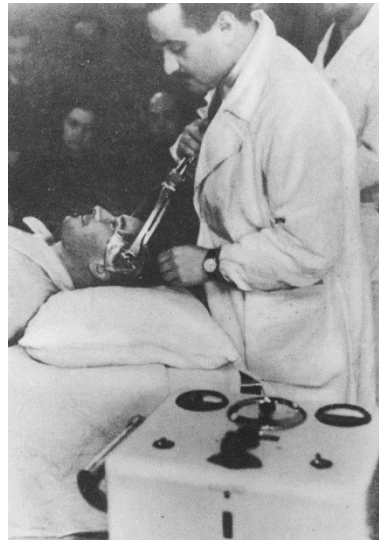


Figure 2.3 Lucio Bini was applying ECT to the patient in the Rome University psychiatric clinic in 1940. (Shorter and Healy, 2007)

Even with the emerging of electrical and magnetic stimulation therapies, the principal remedies for psychiatric conditions were still psychodynamic based treatments until the 1930s. Several novel treatments were proposed during that time period but only electroshock, which was later known as ECT, was still in actions in our modern lives. The historical electrical applications are generally believed irrelevant to the evolution of electroshock therapy. Italian neurologist Ugo Cerletti (1877-1963) is believed to be the originator of the ECT with the application of electric current to provoke a seizure for a short period of time. In 1934, Cerletti's student Angelo Chiauzzi published their work in the journal of *Pathologica* and in their text, they demonstrated that seizures could be introduced in animals by an electrical stimulus (50Hz 220V) for 0.25 second through the electrodes placed in the mouth and rectum. Similar results based on animal experiments were repeated by later researcher Lucio Bini (1908–1964) and safety issues were also identified in the studies, which was resolved by changing the mouth-rectum electrode configuration to temple-temple montage. The first patient involved

human study of ECT was carried out in 1938 to treat the schizophrenia, which was conducted with the present of Cerletti and Bini. The patient was fully recovered after a series of ECT applications and this case report demonstrated that ECT could be applied safely, reliably and affordably, which constituted the advancement of ECT and promoted the swift spread of this uniquely effective therapeutic modality. (Abrams, 2002, Endler, 1988, Shorter and Healy, 2007, Bini, 1938, Linington and Harris, 1988)

2.2. Contemporary Brain Stimulations Techniques

After continual development of brain stimulation techniques, early forms of tDCS, TMS and ECT had evolved with new application facilities and well agreed manipulation protocols. Several novel brain stimulation techniques, like vagus nerve stimulation, deep brain stimulation, transcranial alternating current stimulation and etc., were also developed based on early explorations and intensive researches in the past fifty years.

2.2.1. Vagus Nerve Stimulation and Deep Brain Stimulation

Vagus nerve stimulation is a non-pharmacological treatment for depression and epilepsy. Recent studies have reported VNS as a safe, tolerable, and effective adjunctive remedy for the control of refractory epilepsy. In 2005, it was also approved by the American Food and Drug Administration (FDA) for the treatment of severe, recurrent depression. Early observation of VNS could be dated back to 1880s when manual massage was applied to suppress seizures by compressing the carotid artery in the cervical regions of the neck, which was deemed as the naïve stimulation outcome of VNS. The earliest well documented studies of VNS were carried out by American psychiatrist Percival Bailey (1892-1973) and French neuropathologist Frédéric Bremer (1892–1982) in 1938, later researchers Dell and Olson in 1951. After that, a wide range of animal involved experiments were conducted in the followed decades till 1999. Those studies confirmed the application of VNS in seizure control as promising outcomes were obtained in attenuating the seizure frequency and severity, even the suppression of seizure duration and interictal spikes. The encouraging preliminary studies led to the first application of implantable VNS device on the patient to treat the drug-resistant epilepsy in 1988, which was then followed by more

human implant studies. (Dell and Olson, 1951, Bailey and Bremer, 1938, Lanska, 2002, Zabara, 1985, Lockard et al., 1990, McLachlan, 1993, Woodbury and Woodbury, 1990, Lulic et al., 2009, Weiner et al., 2013, Kuba, 2013)

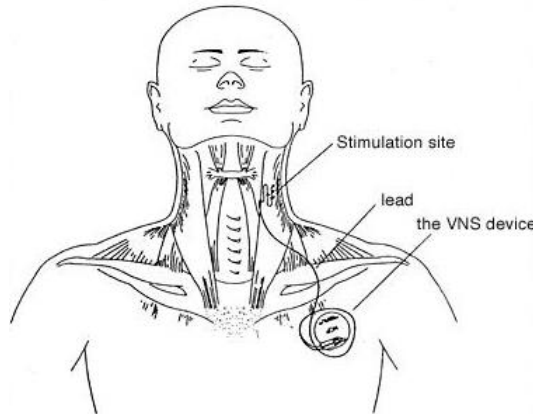


Figure 2.4 Diagrammatic view of implanted VNS device (seizures.dolyan.com, 2016)

Deep Brain Stimulation is a neurosurgical treatment in the control of various mental disorders, which involves the implantation of a neurostimulator in the chest, stimulating electrodes in the target regions of the brain and connection wires between them. The original DBS appeared in 1930s in the mapping of cortical functions, and in the following two decades, neurosurgeons began the investigation of the influence of deeper cortical structure stimulating with the help of newly invented human stereotaxic devices. In 1966, Sem-Jacobsen implanted a bundle of electrode wires deep in the brain and left them in place delivering the stimulations for weeks in the pursuit of locating the optimized target for a subsequent lesion. Even though the objective of such experiment was for the guidance of lesion, it was still considered as the earliest documented deeper brain stimulations using implanted electrodes. Decade later in 1987, the first DBS operation was performed by Professor Alim-Louis Benabid in his clinic and his team also released the first report on the treatment of Parkinson's Disease using DBS later in 1993. Followed studies also reported DBS as an effective treatments for various drug-resist mental disorders and consequently, FDA approved DBS as an alternation treatment for essential tremor and Parkinson's disease in 1997, dystonia in 2003 and severe obsessive-compulsive disorder in 2009. (Benabid, 2003, Penfield and Boldrey, 1937, Spiegel et al., 1947, Sem-Jacobsen, 1966, Benabid et al.,

1988b, Benabid et al., 1988a, Perlmutter and Mink, 2006, Administration, 2015a, Administration, 2009)

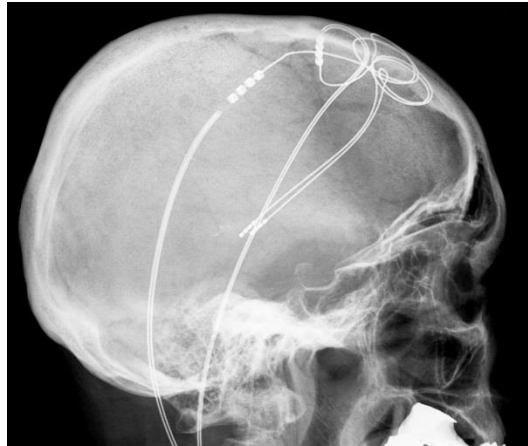


Figure 2.5 X-Ray scan illustration of the implanted electrodes and wires of DBS in the skull in the treatment of Parkinson's Disease (Hellerhoff, 2016).

2.2.2. Transcranial Magnetic Stimulation and Electroconvulsive Therapy

Transcranial Magnetic Stimulation is based on the principle of electromagnetic induction, which induces electrical current flow within the target regions of the brain by the time-varying magnetic field generated in TMS device. Nowadays, both the TMS application protocol and the device are quite different from those utilized in the historical experiments. Current TMS is a mild form of brain stimulation that induces no seizures of the patient and a typical TMS session takes approximately 20-30 minutes. Repeat sessions, known as repetitive Transcranial Magnetic Stimulation (rTMS), will be applied over consecutive weeks, which is normally under restrict regulations based on the specific situations of the patients. As shown in Figure 2.6, the state-of-art TMS device is generally made in the shape of figure eight and the butterfly coils are embedded into it allowing the electrical current flows in the opposite directions around each winding and summing the current at the joining point in the center. With the well developed and managed regulatory protocol of TMS, the evaluation of psychiatric condition is essentially carried out before the stimulation and it brings minimal side effects. FDA has approved the clinical application of TMS in the treatment of migraine in 2013 and major depressive disorder in 2015. (O'Shea and

Walsh, 2007, Administration, 2008, Administration, 2015b, Loo and Mitchell, 2005, Wassermann and Lisanby, 2001)

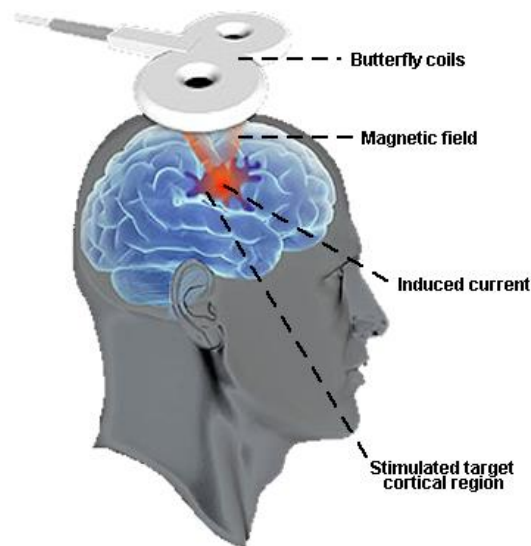


Figure 2.6 Demonstrations of the TMS device and working mechanisms. (Myers, 2004, Neuroscience, 2012)

Electroconvulsive Therapy is an important therapeutic treatment for several serious neuropsychiatric disorders, including Parkinson’s disease, schizophrenia and depression. In addition, it is also under intensive research for its influence on the memory tasks as cognitive impairment still remains a common side effect of ECT with brief pulse. As a convulsive treatment, ECT involves the application of electricity to the brain through the scalp electrodes to induce seizure activity of the patients. Till now, the Neurological Devices Advisory Panel of FDA recommends ECT devices in the Class III device category as high risk devices except for patients suffering from catatonia. However, ECT is still of great importance for the patients who are unsuitable for the drug therapies, especially for the patients with severe psychiatric disorders in the pregnancy period. ECT is reported to increase cortical GABA concentrations and enhance serotonergic function. It also demonstrates influences on the hypothalamic–pituitary–adrenal axis, thus normalizing the dexamethasone suppression test result. The functional brain activations are also altered as Neuronal structure and synaptic plasticity also appear to be influenced (Tharyan and Adams, 2005, Greenberg and Kellner, 2005, Fraser et al., 2008, Lisanby, 2007, Ingram et al., 2008, Leiknes et al., 2015)

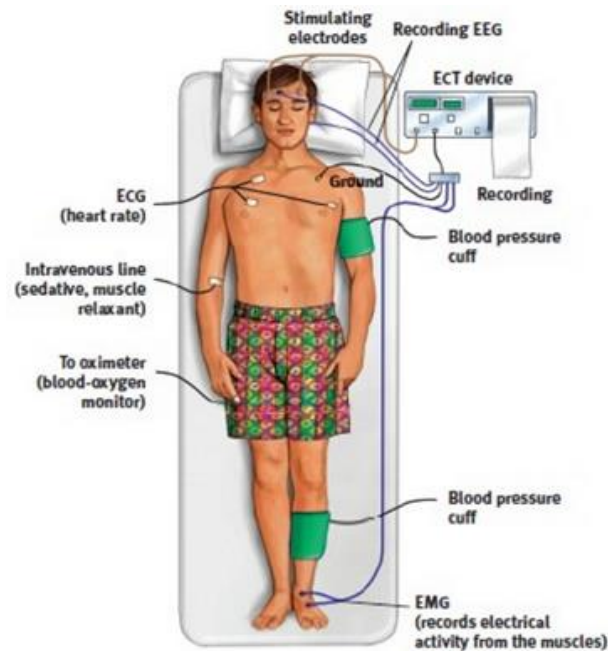


Figure 2.7 Demonstrations of the ECT application coupling with other monitoring devices. (Myers, 2010)

2.2.3. Transcranial Direct Current Stimulation

As introduced before, it has quite a long history using the application of transcranial Direct Current Stimulation or tDCS to modulate brain activities and after intensive research in the past several decades, tDCS has been reported as an effective brain stimulation technique in the control a variety of neurological diseases, ranging from neuron-rehabilitation, tinnitus, chronic pain, focal epilepsy to schizophrenia, depression, stroke and Alzheimer disease. As a non-invasive, painless and sub-convulsive electrotherapy technique, tDCS applies a relatively weak current (0.5-2 mA) through the scalp utilizing saline-soaked sponge electrodes (25-35 cm²) in order to modulate the underlying cerebral functions. It can generate up to 0.08 mA/cm² current densities in the scalp surface and each stimulation session takes about 10-20 minutes. The target stimulated brain region is determined by the proposed electrode configuration, which are normally complied with the 10-20 EEG system. In contrast with TMS, DBS and VNS that are delivered by sophisticated devices, tDCS can be administered with devices already manufactured and used in pain and cosmetic medicine, making tDCS affordable and readily accessible. Currently, tDCS generally contains a battery-driven device, two sponge electrodes and several other components

as shown in Figure 2.8 (left panel). (DaSilva et al., 2011a, Sadleir et al., 2010, Antal et al., 2004b, Antal et al., 2011, Nitsche and Paulus, 2000)

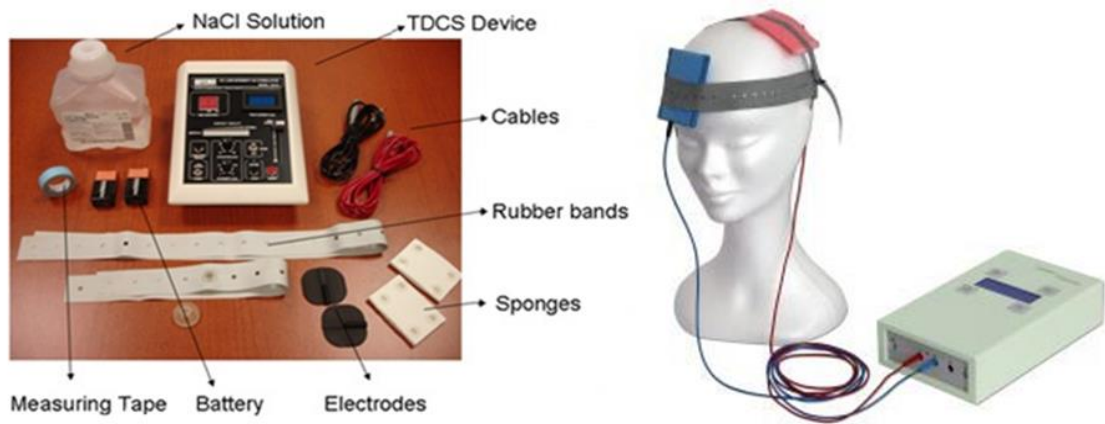


Figure 2.8 Illustrations of a typical tDCS components (left panel) and a classical electrode configuration with C3-Fp2 montage. (GmbH, 2016, DaSilva et al., 2011b)

However, tDCS is still not a precise neuromodulation application compared with DBS and some researchers already challenged the reported promising outcomes of tDCS experiments as the case dependent positive results could be cancelled out by each other (Horvath et al., 2015b, Horvath et al., 2015a). Such varied outcomes were due to the vast targeting regions within the brain and the non-uniformed regulations of tDCS application, including the precise montage placement and dose determination. What is more, as a non-invasive brain stimulation technique, the present of skull and the customer depended variations of brain gyri also make it difficult to achieve exactly the same stimulation outcomes among all the subjects, which calls for the cauterized applications of tDCS as a possible solution. (Antal et al., 2015, Benwell et al., 2015, Li et al., 2015, Fertoni and Miniussi, 2016)

While tDCS was believed to induce particular changes in the neuropsychologic, psychophysiologic and motor activities of the targeted cerebral areas, many animal based experiments and human involving studies have been conducted to explore the mechanisms of tDCS on neuroplasticity shaping during the past decades. So far, agreements have been reached that tDCS works by modulating the spontaneous neuronal network activities, rather than triggering the neuronal firing by suprathreshold neuronal membrane depolarization as TMS and ECT do. At the neuronal level, though anodal DCS is associated with the enhancement of cortical

activity and excitability while cathodal DCS demonstrates suppressing influences, the primary mechanism of action is still believed to be a tDCS polarity-dependent shift (polarization) of the membrane potential in resting state (Brunoni et al., 2012, Nitsche et al., 2008, Bindman et al., 1964b, Purpura and McMurtry, 1965).

However, the mechanisms of tDCS is not merely because of changes of the electrical neuronal membrane potential. Recent researchers also found that tDCS demonstrated the abilities in the modification of microenvironment for synapses. Specifically, both the synaptic activation of the N-methyl-d-aspartate (NMDA) receptor and GABAergic activity are influenced (Liebetanz et al., 2002, Stagg et al., 2009).

In addition, the tDCS induced electrolysis within the brain generates OH^- and H^+ and they are supposed to alter the acid-base balance of both extracellular environment and intracellular environment (Chesler, 2003, Arul-Anandam and Loo, 2009). Moreover, anodal stimulation was found to be associated with the long lasting accumulation of Ca^{2+} within the rat cortex, hippocampus and thalamus for up to 3 days after 1 day of the stimulation. As a consequence of Ca^{2+} accumulation, the increased pH environment stimulates the neuron and boosts their activities while the low pH associated acidosis suppresses neuronal activity. The latest research on mouse brain stimulation confirmed the dramatic surge of astrocytic Ca^{2+} across the entire cortex after tDCS, which revealed the glial involvement in tDCS induced plasticity. All those findings supported the pH alteration within the cortex after tDCS. Therefore, the changes of both synaptic microenvironment and cortex metaplasticity are also attributed as the mechanisms of tDCS (Monai et al., 2016).

Transcranial Alternating Current Stimulation is different from tDCS by applying oscillating electrical currents to stimulate the brain and modulate the cortical excitability and activity, though the device of tACS is generally similar to tDCS. Many recent studies reported that tACS could represent a more targeted stimulation paradigm for the enhancement of cortical oscillations. According to Manoli's numerical study based on a realistic human head model in 2012, tACS at 10Hz was believed to result 2.5 times greater electrical fields than tDCS and the induced electrical fields was even more focused compared to tDCS. However, with the increasing of alternating current frequency from 10 Hz to 100 Hz and 1000 Hz, the generated electric field became

smaller while the induced cerebral fields also became less focused. (Antal and Paulus, 2013, Ali et al., 2013, Manoli et al., 2012)

For both tDCS and tACS, their electrode montage configurations complies with the international 10-20 EEG positioning system, which is the most commonly used in the placement of scalp montage. Different electrode configurations are expected to induce varied electrical filed within the brain.

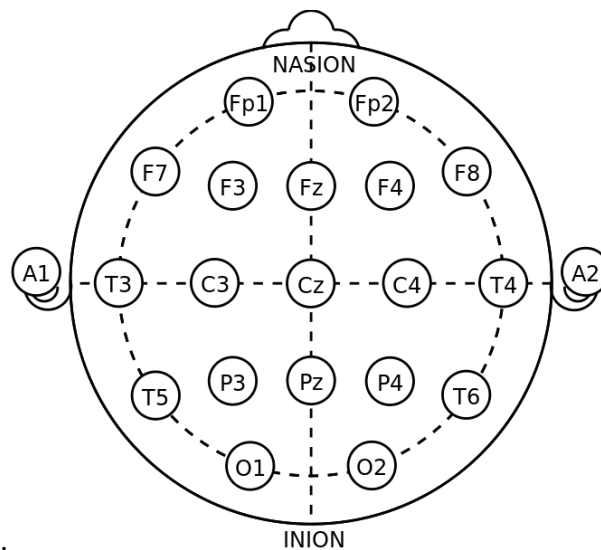


Figure 2.9 Electrode locations of International 10-20 system for EEG recording (トマソン 124, 2010)

2.3. Electrical Therapeutic Treatments for Brain Tumors

According to the latest collaborative report released by American Cancer Society, National Cancer Institute, the Centers for Disease Control and Prevention, and the North American Association of Central Cancer Registries in 2016, brain cancer has surpassed leukemia as the leading cause of cancer death among children and adolescents (aged birth – 19 years) because of the dramatic therapeutic advances against leukemia. While leukemia accounts for 30% of all childhood cancers, including benign/borderline brain tumors, tumors within the brain and other nervous system are still considered as the second most deadly cause of children motility (26%) (Siegel et al., 2016).

As for the treatment of brain tumors, the therapies are highly depended on the tumor type, size, grade as well as the physical condition of the patients. In general, removal

of the brain tumor by surgery is referred as the first treatment, especially for the patients with low grade brain tumors. Besides, traditional therapies for brain tumor control, including radiation therapy and chemotherapy, are also usually applied as the following up treatments after brain tumor removal surgeries. Apart from the conventional therapies for brain tumors, several novel treatments for tumor control are becoming increasingly accepted after clinical trials. Specifically, they are Electrochemotherapy and Tumor Treating Fields. Both of them are utilizing low level electricity during their applications. Moreover, Low Level Direct Current Therapy was proved to be an effective therapeutic approach to the control of tumor growth as well based on animal involving experiments. Such findings highlighted the promising effect of electrical current on the tumor treatment. (Serša et al., 2006, Rehman et al., 2015, Griffin et al., 1994)

Tumor Treating Fields, also known as alternating electric field therapy, is an FDA-approved novel antimitotic and frequency-tuned electric field therapeutic option with the application of low intensity (1 – 2 V/cm) and intermediate frequency (100 – 300 kHz) alternating fields in controlling of brain tumor growth (Pless and Weinberg, 2011, Davies et al., 2013). TTFs also demonstrates supplementary or collaborative relationship with the conventional chemotherapy during the combination treatments for brain tumors, especially for malignant tumors, like recurrent glioblastoma multiforme (GBM). Compared with the traditional solely applied chemotherapy to control the growth of brain tumors, TTFs is supposed to provide a more affirmative approach with better safety insurance. Furthermore, several case reports also confirmed that TTFs was able to provide better life quality for the patients and even extend their survival time (Kirson et al., 2004, Kirson et al., 2009, Schneiderman et al., 2010, Kirson et al., 2007).

According to the conclusions made in the experimental studies and clinical trials, alternating electrical current has demonstrated a broad range of influences on the living tissues. In the low frequency range under 1 kHz, alternating electrical fields stimulate the living tissues by membrane depolarization while the stimulation effect diminishes with further increasing the frequency of alternating electrical fields because of the cancellation effects of the alternating cell membrane hyper-depolarization cycles integration. Over the very high frequency range measured in MHz, tissue heating

phenomenon becomes increasingly predominant with the increase of alternating electrical field frequency, intensity and tissue dissipation factor due to the dielectric losses. However, for the electrical fields in intermediate frequency (100kHz-MHz), only minute dielectric losses or heating influence could be generated. With properly tuned low-intensity intermediate-frequency electrical fields in TTFs, arrested cancer cell proliferation and proposed tumor destruction could be achieved without detectable influences on the surrounding normal tissues by disrupting the microtubules of the mitotic spindle and the electric focusing the field in the dividing cells (Kirson et al., 2004).

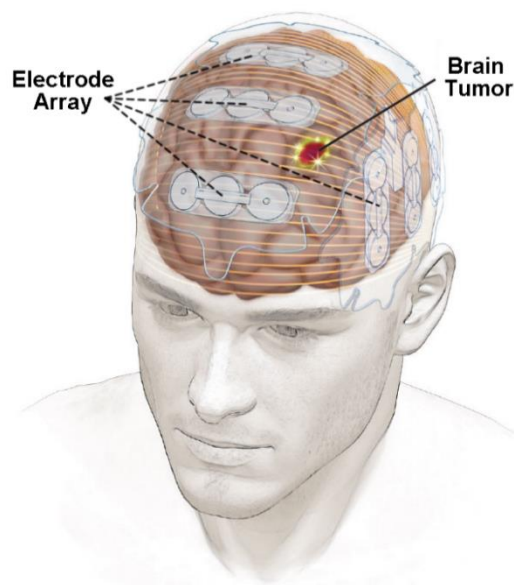


Figure 2.10 Illustration of the TTFs device worn on the head. (Moore, 2016)

In this chapter, from the development of brain stimulations and other electrical therapies, it is obvious to conclude that tDCS stands out by its non-invasive, sub-convulsive manner and affordable applications. Apart from the common neurological diseases, tDCS shows promising effects on the control of chronic and acute pain, including cancerous pain (Antal et al., 2010, Antal et al., 2008b, Lefaucheur et al., 2008). In addition, tDCS also demonstrates capabilities in enhancing drug delivery and brain intracellular pH (Minhas et al., 2010, Rae et al., 2013). Therefore, it should be an encouraging clue to explore the applications of tDCS on the patient with brain tumors to treat their neuropsychiatric conditions and pre-validate the possible suppressing influence of tDCS induced electrical fields on the tumor growth.

3. COMPUTATIONAL HUMAN HEAD MODELLING

The development of tDCS and other relevant transcranial electrical stimulations is coupled with the advancement of human head models to assist the understanding of induced current patterns within the cortex and predicating the proposed stimulation outcomes.

3.1. The Advancement of Human Head Modelling

The development of stimulation orientated human head models can be divided into four stages, analytical model, spherical model, low-resolution realistic human head model and high-resolution realistic human head model (Bai et al., 2013a).

3.1.1. Early Analytical Human Head Models

The early analytical models adopt Legendre polynomials to solve the differential equations for the distributions of electrical potential within the human head models. As demonstrated in Figure 3.1, the most representative one of such models is Rush and Driscoll's model developed in 1969. This model is composed by three concentric spherical layers to represent the scalp, skull and brain. Each layer is considered as homogeneous and assigned with isotropic conductivity. The electrical potential generated in this model can be expressed by a series of Legendre polynomials while the current density is calculated by the production of potential gradient and the brain conductivity. These models are simple, but they still provide important information for the current distributions within the human head, which can also be confirmed by more sophisticated models afterwards (Rush and Driscoll, 1968, Weaver et al., 1976, Grandori and Rossini, 1988, Saypol et al., 1991).

Though analytical models can provide insight previews of system behaviours, these models only include several simple geometries because the analytical functions are awkward to applied in models contracted with complex geometries. In contrast to the analytical models, computational models utilize numerical approximation to simulate

physical phenomena within biological systems, which works for models with complex structures.

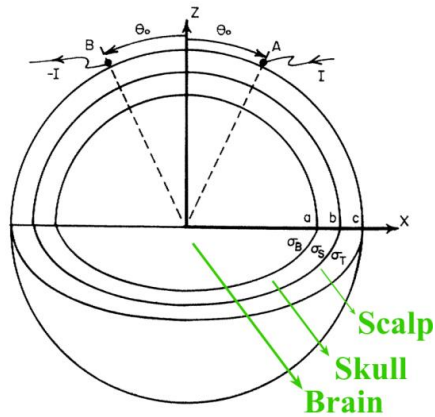


Figure 3.1 Early analytical model (Rush and Driscoll, 1968)

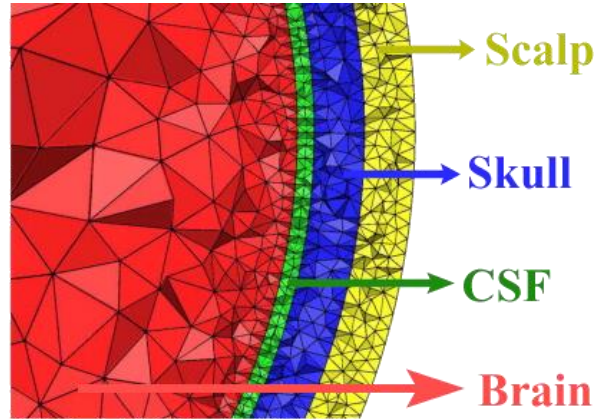


Figure 3.2 Finite element spherical model (Drechsler et al., 2009)

3.1.2. Finite Element Spherical Human Head Models

Advanced by the mature of computational devices, a proliferation of numerical methods are used in the human head modelling associated with transcranial Electrical Stimulation (tES), which results in the finite element method to simulate the tES. Therefore, it becomes possible to handle the complex geometries and boundary conditions by the image segmentation techniques and colossal finite element data processing capacities (Bai et al., 2013a).

Finite element (FE) spherical models are almost the same compared with the early analytical models and they also contain several concentric spherical layers representing different brain structures (scalp, skull, CSF, WM and GM) according to varied research purposes. For many studies, the models they use are based on the original Rush-Driscoll model and three typical layers (scalp, skull and brain) are included and their dimensional features are derived from human subjects (Miranda et al., 2006, Datta et al., 2009, Faria et al., 2011, Deng et al., 2011). Electrodes are generally modelled as separated part attached to the scalp and their electrical conductivities are assigned according to the real material's property. The boundary conditions applied for the anode and cathode are inward current boundary condition and potential ground boundary condition, separately, while electrical insulating is

applied to the other external boundaries and continual current is applied to all tissue-tissue boundaries. In the mesh generation of the model, the tetrahedral quality metric are generally used, which are robust and known to correlate well with the element quality metrics used without increasing the computational workload.

FE spherical models provide the foundation for many researches, which result in several important outcomes (Miranda et al., 2006, Faria et al., 2011, Deng et al., 2011, Deng et al., 2008). Some studies show that more current will be able to penetrate the scalp and skull, and reach the target regions with the distance increase between stimulation electrodes, which enables the current to reach deeper target regions with the same current density applied to the electrodes. As a cost, the focal of the target regions is not as good as before due to the increased size of target regions while it can be improved by the application of multiple electrodes. Another benefit contributed by the FE spherical models is the introduction of equivalent current, which depicts the injected current amount with varied electrode montages in order to maintain current density or electrical field in a fixed level. However, FE spherical models also have the same problem as the analytical models do, which is their oversimplification of the complex head geometry. The structures of human head tissues are irregular and their shapes extremely vary, thus altering the current flows within the human head. Therefore, the current distributions cannot be that uniform and this conclusion is confirmed by the studies that considered more complex structures afterwards. The anisotropic electrical conductivity property of WM, GM has also been ignored and caused the result being inaccurate compared with later studies.

3.1.3. Low-Resolution Realistic Human Head Models

The remarkable improvements of human body visualization and modelling methods make it possible to construct complex human head models with more anatomical accuracies, benefited from which, subject-specific models are even possible for individual patients. These low resolution models are derived from detailed head geometry descriptions or directly from MRI scans of subject head, which forms their advantages over previous models.

Many studies based on the low resolution models have made surprising findings and some of them are in accordance with previous studies while some are controversial.

The current density in different brain structures varies extremely, with the maximum current density penetrated to the brain is much lower than that found in the scalp layer because of the current shunting. It also confirms that smaller electrodes lead to higher current shunting (Miranda et al., 2009, Wagner et al., 2006, Wagner et al., 2002). However, some result show that the maximum current density was greater when the electrodes were placed along scalp locations with less curvature of the head. This result is contradictory to the early conclusions derived from FE spherical models, which emphasises the importance of realistic human head models (Grandori and Rossini, 1988, Rush and Driscoll, 1968, Saypol et al., 1991, Wagner et al., 2006).

Low resolution anatomically based models have their advantages in the realistic human head modelling, but the application is still confined extensively due to their insufficient anatomical accuracy, especially for the presentation of brain structures. Many brain structures are ignored in the modelling, such as the brain folding, ventricles as well as the anisotropic conductivity for some tissues, such as WM and GM. As a consequence, it is impossible to derive the local inhomogeneous current distributions, which limits the utility of such models.

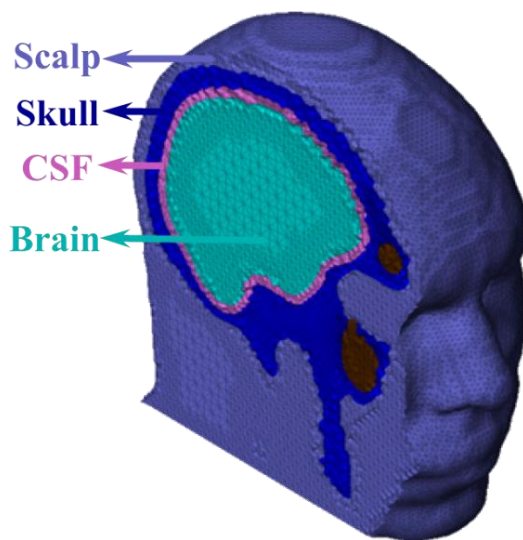


Figure 3.3 Low-resolution realistic model (Bai et al., 2012)

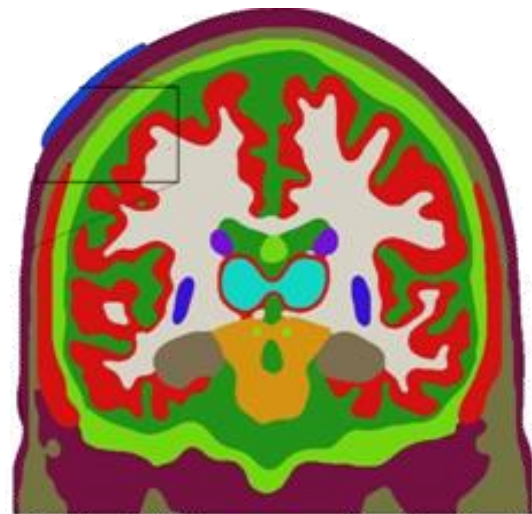


Figure 3.4 High-resolution realistic model (Shahid et al., 2013a)

3.1.4. High-Resolution Realistic Human Head Models

As many studies based on the previous model types have highlighted the importance of complex brain geometries, increasingly more brain stimulation orientated modelling studies are using high-resolution human head models. These models are generally based on the MRI scans of human subjects, which depict the brain structures in details. The anisotropy properties of skull, WM, GM are also considered in these models.

Datta conducted a number of studies based on high resolution models and used these models to investigate the influence of CSF on the current distributions, which has the similar result derived from 2D model studies. Multiple electrodes configuration based on high resolution models also significantly improves the spatial focality of target regions (Datta et al., 2011, Datta et al., 2009, Datta et al., 2008a, Opitz et al., 2015, Song et al., 2016b, Bai et al., 2014). With the help of these models, considerable brain stimulation refinements have been done to improve the clinical performances. Furthermore, customized brain stimulation treatments have been raised for individual patients with the aim to provide individualized therapies because individual anatomical changes within brain may dramatically influence the current distribution.

3.2. Computational Bioelectromagnetism

Bioelectromagnetism is the foundation for transcranial electrical stimulation studies and it combines the theories from electromagnetic fields and biological subjects and deals with electrical, magnetic and electromagnetic phenomenon in living cells, tissues and organs (Malmivuo and Plonsey, 1995).

3.2.1. Quasi-static Approximation

In the frequency range between direct current (DC) and 10 kHz, several approximations can be made to simplify the field solutions (Heller and van Hulsteyn, 1992, Ferdjallah et al., 1996). Because the wavelengths of electromagnetic waves in these ranges are several orders longer than the dimensions of a biological medium, the bioelectric currents and voltages in living tissues can be considered as stationary (Plonsey and Heppner, 1967). A recent study evaluated the difference in neural activation between solving a quasi-static field approximation and the full inhomogeneous Helmholtz equation using square-pulse current stimuli, and found that for the stimulus parameters generally used (such as pulse amplitude and width) , the

exact solution for the potential and capacitive tissue effects could be approximated by the quasi-static approximation. Since the permittivity and magnetic permeability in living tissues are assigned with relatively low values, the quasi-static approximation is applicable in the computational head modelling associated with tES (Wagner et al., 2007b).

3.2.2. Infinitesimal Volume Conductor

Given an infinitesimal homogeneous block volume conductor, its dimensional sides are represented by Δx , Δy and Δz , and its electric conductivity is σ . Figure 3.5 describes the net current out of the block in x direction. Specifically, the dimensions for the infinitesimal volume conductor block are Δx , Δy and Δz , \mathbf{J} is a vector field representing current density and i is the scalar volumetric current source within the block. J_x , J_y , J_z are the scalar components of \mathbf{J} on the Cartesian axes x , y and z , respectively.

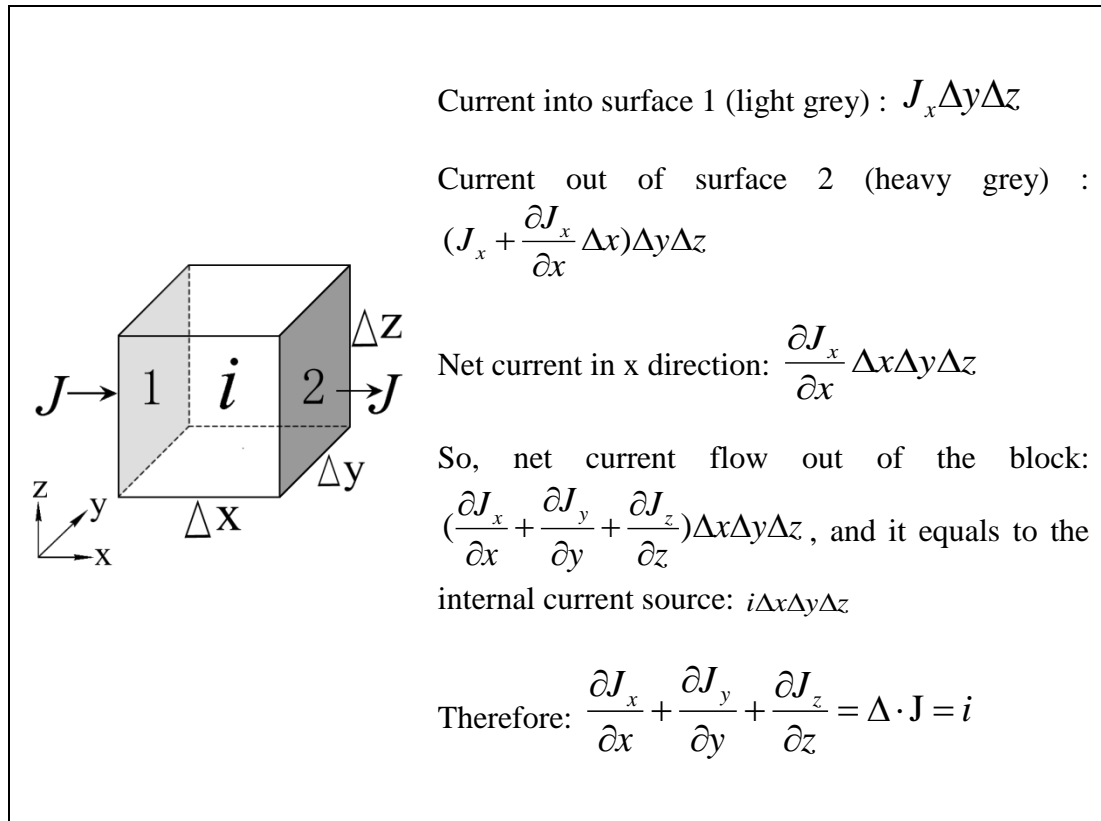


Figure 3.5 The net current out of the block in x direction

From Figure 3.5, an electric field (E-field) strength E throughout the conductor and the net current flow out of the volume must meet the following divergence relationship:

$$\Delta \cdot \mathbf{J} = i \quad \text{Equation 3.1}$$

According to Ohm's law, the relationship between the current density vector \mathbf{J} (amperes per unit area) and E-field:

$$\mathbf{J} = \sigma \mathbf{E} \quad \text{Equation 3.2}$$

Under the quasi-static condition, the E-field \mathbf{E} is defined as the negative gradient of scalar electric potential ϕ :

$$\mathbf{E} = -\nabla \phi \quad \text{Equation 3.3}$$

Therefore, Equation 3.1 can be expressed as:

$$\nabla \cdot (-\sigma \nabla \phi) = i \quad \text{Equation 3.4}$$

Equation 3.4 is also known as Poisson's partial differential equation. Since i is the volume current source within the activated cell, which represents the cell excitability, and it can be approximated to 0 in the typical passive volume conductor model ($i=0$):

$$\begin{aligned} \nabla \cdot (-\sigma \nabla \phi) &= 0 \\ \text{or} \\ \nabla \cdot \begin{bmatrix} \sigma_{xx} & \sigma_{xy} & \sigma_{xz} \\ \sigma_{yx} & \sigma_{yy} & \sigma_{yz} \\ \sigma_{zx} & \sigma_{zy} & \sigma_{zz} \end{bmatrix} \begin{bmatrix} \partial \phi / \partial x \\ \partial \phi / \partial y \\ \partial \phi / \partial z \end{bmatrix} &= 0 \end{aligned} \quad \text{Equation 3.5}$$

Finally, Equation 3.5, also known as Laplace partial differential equation is derived, and it will be used in the realistic human head modelling. For the tissues with isotropic conductivity (such as fat, CSF), σ is simply a scalar while it will be a tensor for those have anisotropic conductors that demonstrate preferential directions of current flows.

3.2.3. Boundary Conditions Assignment

In tDCS modelling, boundary conditions define the relationship between the external stimulation and the estimated potential gradients in a volume conductor model. Equation 3.5 describes the field distribution in the head model domain after applied an external stimulus. The boundary condition in Equation 3.6 defines the continuity of the normal component of the current density between regions of different conductivity.

$$(n \cdot J_1)|_{\Gamma_i} = (n \cdot J_2)|_{\Gamma_i}$$

or

Equation 3.6

$$[n \cdot (\sigma \nabla \varphi_1)]|_{\Gamma_i} = [n \cdot (\sigma \nabla \varphi_2)]|_{\Gamma_i}$$

The boundary condition in Equation 3.6 is only applicable to the inner tissue-tissue boundaries (Γ_1, Γ_2) of volume conductors while the exposed boundaries (Γ_e) are modelled as electrically insulated and represented by Neumann boundary conditions:

$$(n \cdot J)|_{\Gamma_e} = 0$$

or

Equation 3.7

$$[n \cdot (\sigma \nabla \varphi)]|_{\Gamma_e} = 0$$

The exposed surface of cathode is assigned with the Dirichlet boundary condition ($\varphi = 0$ volts) while the exposed surface of anode can be assigned with either the Dirichlet ($\varphi = \varphi_0$ volts) or the Neumann ($n \cdot J = J_n$ A/m²) boundary conditions, where φ_0 is the constant electrode voltage and J_n is the normalized current density on the electrode surface.

3.3. tDCS Orientated Computational High Resolution Realistic Human Head Modelling

One of the highlights in this project is the development of a multimodal high resolution realistic human head model with twenty-nine tissue types and gyri precision for the GM. A typical workflow for constructing high resolution realistic human head models based on MRI scans is shown in Figure 3.6.

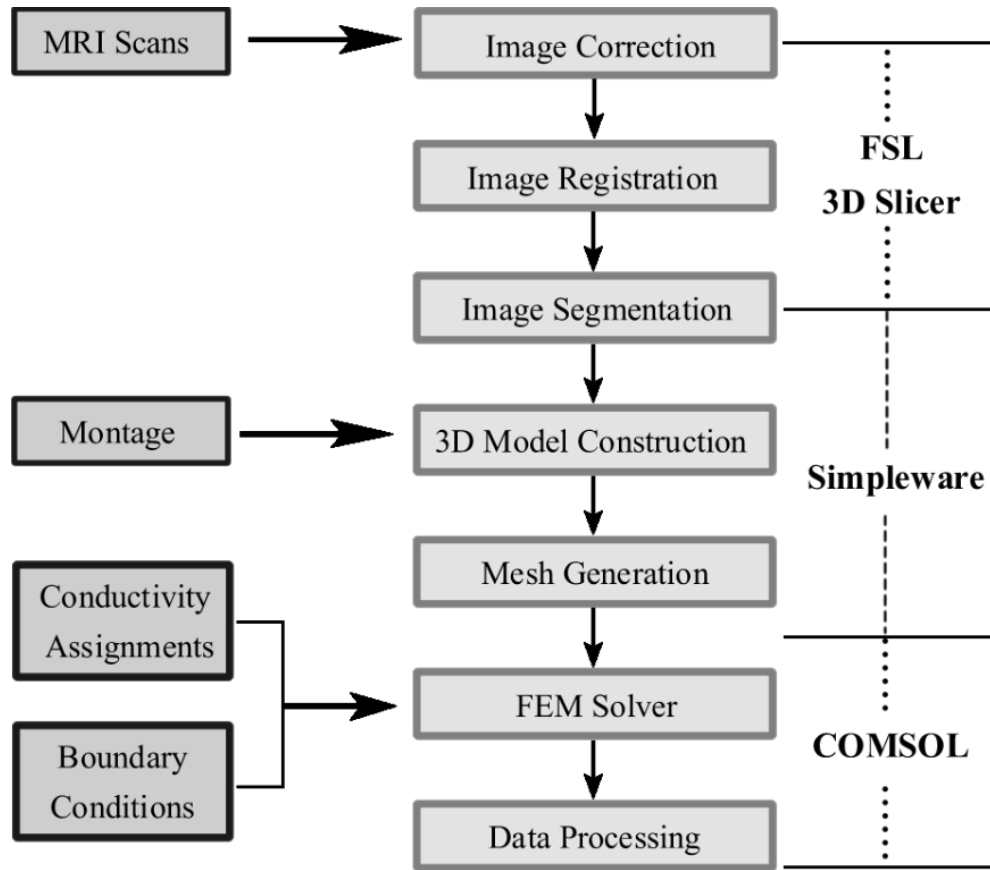


Figure 3.6 A simplified typical workflow in the development of high resolution realistic human head models.

The construction of such high resolution model in this study was achieved by a combination of several open source and commercial software packages, including 3D slicer, BrainSuite, FSL and Simpleware. A particular algorithm on blood vessel segmentation was also applied using Matlab in investigating the role of blood vessel in defining the current distributions during tDCS.

3.3.1. MRI Image Processing

Image Metadata: In this project, the high resolution realistic human head model was constructed from multiple MRI scans of the same subject using different scanning parameters. The data were obtained from the International Consortium for Brain Mapping (ICBM) database and the chosen subject was MNI_0663 from Montreal Neurological Institute of ICBM. The datasets used in the modelling were T1, T2 weighted MRI scans and Magnetic Resonance Angiography (MRA) scans of MNI_0663. The original T1-MRI has the best spatial resolution ($0.54 \text{ mm} \times 0.54 \text{ mm}$

$\times 1.0$ mm), which was later resampled with 1.0 mm^3 voxel resolution by default during image processing in FSL, thus resulting a $256 \text{ mm} \times 256 \text{ mm} \times 176 \text{ mm}$ dimension for the model. MRA is an imaging technique based on MRI to generate images of blood vessels and the original spatial resolution of MRA dataset in this study is $0.625 \text{ mm} \times 0.625 \text{ mm} \times 0.6 \text{ mm}$. The other metadata information of the image scans is listed in Table 3.1.

| | Slice Thickness (mm) | Flip Angle (Degree) | TE (ms) | TR (ms) |
|--------|-------------------------|------------------------|---------|---------|
| T1-MRI | 1 | 30.0 | 9.2 | 22.0 |
| T2-MRI | 2 | 90.0 | 35.0 | 3300.0 |
| MRA | 0.6 | 25.0 | 6.9 | 33.0 |

Table 3.1 Scanning parameters of the MRI and MRA datasets.

Image Registration: By definition, image registration is the mapping operation between two images both spatially and with respect to intensity. The spatial registration operation on multiple scanning datasets of the same subject is a crucial prerequisite for the construction of realistic human head model because it guarantees that the source image with particular coordinates represents the same anatomical features of the reference or target image. The image registration operation in this project was carried out with the assistance of an open source MRI processing platform named 3D Slicer, which provides a number of state-of-the-art algorithms for rigid, affine, deformable registration and manual registration. Those options are selected depending on the anatomical site (e.g., brain vs. prostate), purpose (multimodal vs. longitudinal vs. registering to an atlas), performance (speed vs. accuracy vs. robustness) and level of interaction (e.g., use of fiducials or markers) (Fedorov et al., 2012, Zitova and Flusser, 2003, Brown, 1992). Specifically, both T2-MRI was registered to T1-MRI using rigid registration while MRA dataset was registered to T1-MRI using both rigid and landmark registration approaches. In particular, the transformation matrix was obtained during MRA registration and it was used to manually register the filtered MRA image using Hessian based Frangi vesselness filter (Kroon, 11 June 2009).

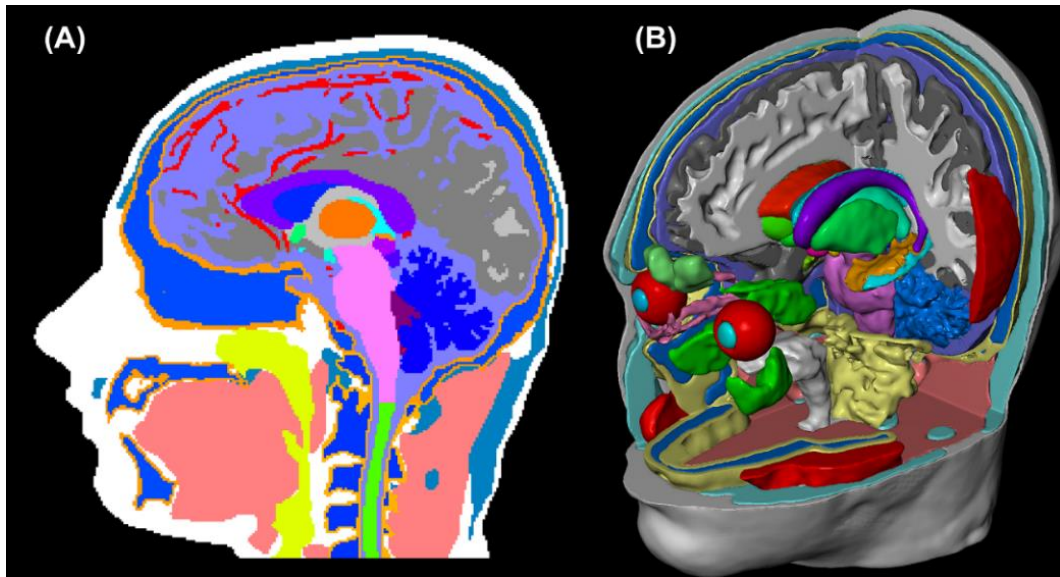


Figure 3.7 Demonstrations of the final segmentation outcomes for the study of blood vessel systems. (A): Sagittal 2D slice view. (B): 3D render view

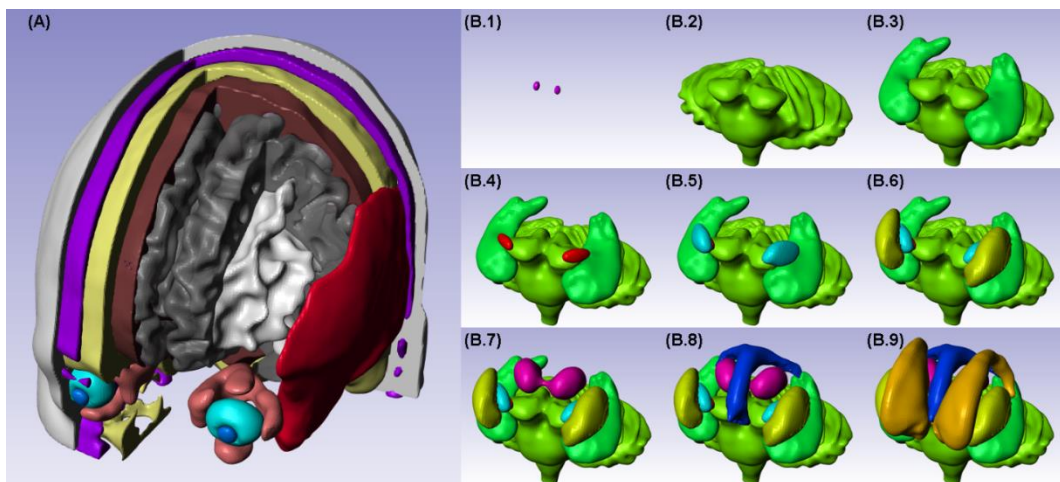


Figure 3.8 Demonstrations of the final segmentation for the study of brain tumors. (A): 3D render view of major human head tissue types. (B.1) - (B.9): 3D render views of inner brain structures.

Image Segmentation: For the study of blood vessels system, after the spatial registrations, both T1 and registered T2 MRI datasets were performed the skull stripping operation and automatic segmentation of scalp, skull, CSF, WM and GM using FSL platform (Jenkinson et al., 2012). Simultaneously, another set of the head tissues masks were also generated using BrainSuite package as reference masks for semiautomatic corrections during the final segmentations (Shattuck and Leahy, 2002). As aforementioned, the mask of blood vessels was obtained from the Frangi vesselness filter processed and manually registered MRA dataset. Then, all the masks were imported into Simpleware for further segmentation and manual corrections against the

human head atlas (Mai et al., 2016). After further tuning the boundary range values of the filtered and registered MRA volume, it became possible to segment the minor branches of blood vessels, which were hard to notice without tuning operation. As a result, the control model for each montage contained 26 masks excluding the gyri while the proposed models had additional four masks for the intracranial blood vessel and extracranial blood vessels. For the study of brain tumors, the methodology utilized was almost the same but only FSL and Simpleware software packages were involved during the segmentations. As shown in Figure 3.8, about 22 masks excluding brain tumors were constructed in this study.

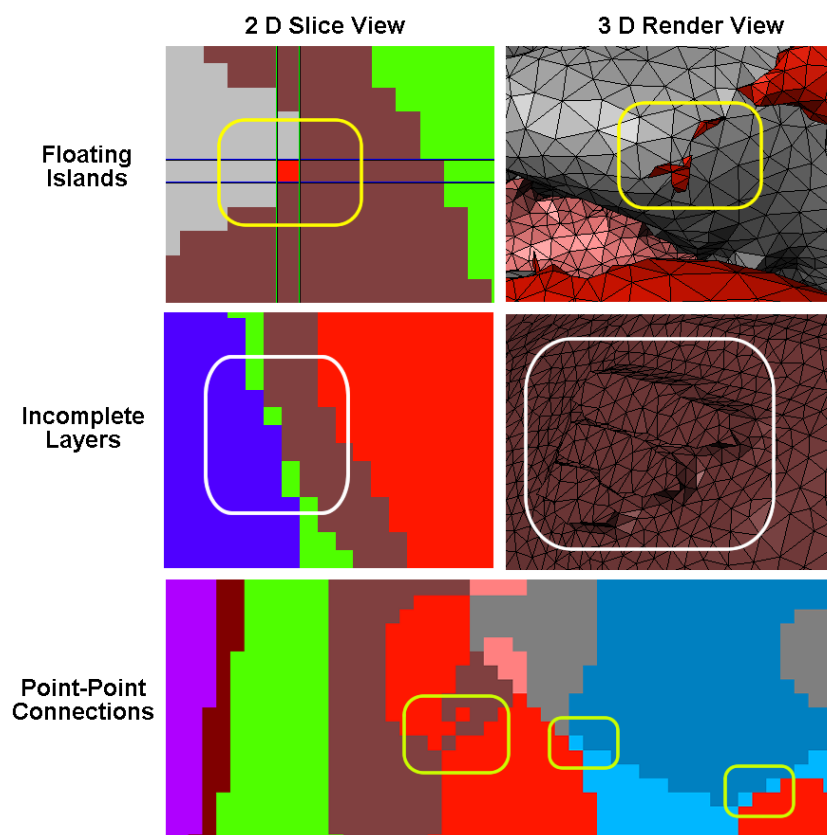


Figure 3.9 Demonstration of the manual correction operations.

Manual Correction: Segmentations using automatic segmentation tools can save extremely a lot of labor work. However, most of current automatic segmentation software packages and algorithms are still not perfect because the problems of floating islands, incomplete layers and point to point connections. As shown in Figure 3.9, manual correction operations were performed to fix the above issues using ScanIP module of Simpleware.

3.3.2. Electrode Montage Configurations

The montage and size of electrodes are two crucial stimulation parameters in defining the target cortex region and outcome of the stimulation (Faria, Leal & Miranda 2009; Miranda, Lomarev & Hallett 2006). In this study, the electrode configurations complied with the International 10-20 EEG recording system and both the cathode and anode were modelled as 5 cm × 5 cm saline soaked sponge pads, which were generally used in conventional tDCS applications. Two sets of electrode configurations were constructed according to the separate studies of brain tumors and blood vessels system. Each montage set contained five common tDCS montages with increasing inter electrode distance and varied target stimulation regions.

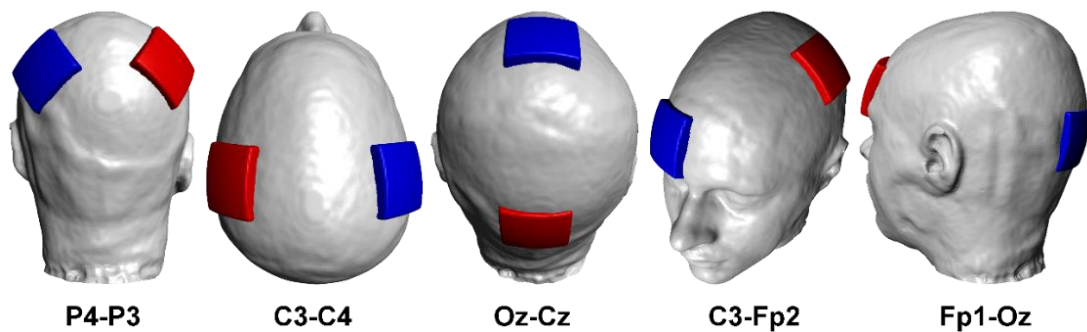


Figure 3.10 Electrode montages constructed in the study of blood vessel systems.

Specifically, the five electrode configurations constructed in the study of blood vessels system are P4-P3, C3-C4, Oz-Cz, C3-Fp2 and Fp1-Oz and their corresponding inter electrode distance are 97 mm, 121 mm, 133 mm, 141 mm and 193 mm, respectively. As shown in Figure 3.10, electrode montage P4 (right parietal lobe) – P3 (left parietal lobe) is used to stimulate the parietal lobe regions in the numerical competence studies (Kadosh et al., 2010). Montage C3 (left M1-motor cortex area) – C4 (right M1-motor cortex area) is applied to stimulate the contralateral orbital motor cortex in the treatment of stroke (Hesse et al., 2007). Montage Oz (occipital cortex) – Cz (vertex) is applied to stimulate the primary visual cortex in the visual processing tasks (Antal et al., 2004a). Montage C3 (left M1-motor cortex area) - Fp2 (right contralateral supra-orbital region) is used to stimulate the primary motor cortex and contralateral supraorbital regions in the studies of cancer pain control (Silva et al., 2007). Montage Fp1 (left supraorbital region) – Oz (inion) is referred to stimulate the left supraorbital in the treatment of depression (Bai et al., 2014).

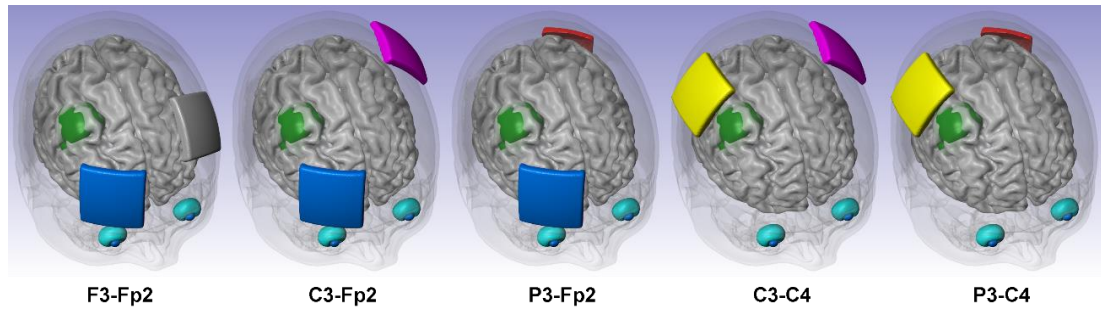


Figure 3.11 Electrode montages constructed in the study of brain tumors.

As for the study of brain tumors, the chosen five electrode montages are F3-Fp2, C3-C4, C3-Fp2, P3-C4 and P3-Fp2 and their inter-electrode distances are 91 mm, 126 mm, 143 mm, 156 mm and 199 mm, respectively. Figure 3.11 gives a 3D demonstration for those proposed electrode configurations.

3.3.3. Electrical Conductivity Assignment

In this project, the influence of anisotropic electrical conductivity was not the focus and the isotropic electrical conductivities of all proposed tissue types in the control models were listed in Table 3.2. As for the electrical conductivity of other proposed tissue types, like blood vessels system and brain tumors in different grades were given in their corresponding chapters with detailed assignment reasoning.

3.3.4. Mesh Generation and Computation

After the manual corrections and montage assignments, the models were meshed using +FE Free meshing algorithm provided in Simpleware. For the study of blood vessels system, the compound coarseness was set to -30. Therefore, the final volumetric finite element models in the control group contain about 10 million finite elements while the number is approximately 13 million for the proposed models.

After assigning the boundary conditions and electrical properties, the computation was carried out in a commercial software package named COMSOL Multiphysics and each simulation took about half an hour for a computing workstation with dual Intel Xeon E5-2697 V3 CPUs. For the study of brain tumors, the compound coarseness was set to -15 whereas the region of tumor was further refined by setting the mesh size to 0.8 mm. The derived volumetric finite element models contain 8 million tetrahedral

elements and each simulation consumed approximately one hour for an 8-core workstation.

| Material | Conductivity (S/m) | Reference |
|---|-------------------------------|----------------------------|
| Saline soaked electrodes | 1.4 | (Datta et al., 2009) |
| Scalp | 0.43 | (Shahid et al., 2014a) |
| Fat | 0.025 | (Gabriel et al., 1996a) |
| Muscles (head, neck and eyes) | 0.16 | |
| Eyes | 0.5 | |
| Eye lens | 0.31 | (Gabriel et al., 1996b) |
| Skull | 0.015 | (Oostendorp et al., 2000a) |
| CSF (including four ventricles) | 1.79 | (Baumann et al., 1997b) |
| GM | 0.32 | (Gonçalves et al., 2003) |
| WM | 0.15 | (Nicholson, 1965) |
| Hindbrain (cerebellum, colliculus, medulla, mammillary body and cerebral aqueduct) | 0.25 | (Geddes and Baker, 1967) |
| Spinal Cord | | |
| Fornix Crura | | |
| Globus pallidus pars interna | 0.32 | (Gonçalves et al., 2003) |
| Globus pallidus pars externa | | |
| Nucleus Accumbens | | |
| Amygdala | | |
| Fornix Crura | | |
| Hippocampus | | |
| Thalamus | | |
| Putamen | | |

Table 3.2 Electrical conductivity of the normal tissue types included in the control models of this project.

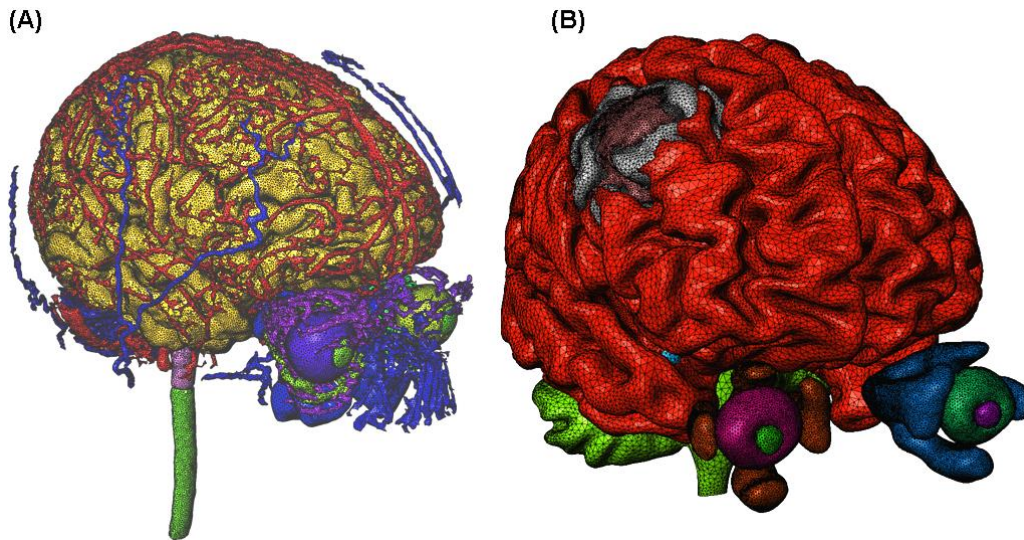


Figure 3.12 Mesh generations for the studies of blood vessels system (A) and brain tumors (B).

3.3.5. Workflow Summary

In this project, there are four major procedures during the development of high resolution realistic human head model. Firstly, MRI image was processed in three key steps, image registration using FSL and 3D Slicer, image segmentation using FSL, BrainSuite and Frangi vesselness filter, semiautomatic image correction using ScanIP module of Simpleware. Secondly, sponge electrode montages were configured against the 10-20 EEG recording system using +CAD module of Simpleware. Thirdly, MRI based model was meshed using the +FE Free meshing algorithm provided in ScanIP and the mesh size was further tuned in specific regions of interest. Finally, the meshed model was applied with electrical properties and boundary conditions in Multiphysics COMSOL before the final computations.

In this chapter, the advancement of human head modelling are systematically presented, which highlights the demand of high resolution realistic human head models to assist the precise tDCS application. In addition, the construction of high realistic human head models for this project is also described in detail and such methodology is repeatable for the following computational studies of tDCS and other stimulation techniques.

4. IMPACT OF BRAIN SHIFT ON CURRENT DISTRIBUTIONS

4.1. Introduction

In the early stage of human head modelling, concentric spherical models were used broadly. A typical three layer model has scalp, skull and brain. With the emerging of MRI, DTI and Diffusion Spectrum Imaging (DSI), increasingly more researches focus on the realistic human head models. Many studies found that CSF distribution had significant impacts on tDCS and many other neurophysiological modulation techniques (Sadleir et al., 2010, Miranda et al., 2006). However, there is little research on the impact of head orientations on the current distributions during tDCS. Since CSF is a kind of bodily fluid that acts as a buffer or cushion for the brain (as shown in Figure 4.1), the brain may compress the CSF closer to the ground direction due to the downward shift caused by gravity (Shahid et al., 2011, Bijsterbosch et al., 2013). That is, the distribution of CSF is subject to change according to different head orientations as the CSF facing the ground side always tends to be thinner than that of the other sides. This fact should be considered during tDCS.

This chapter numerically investigates the influences of brain displacements in two head orientations (left lateral and right lateral) with two different electrode montages (C3-C4, C3-Fp2) during tDCS. In the methodology part, 26 real shape human head models were developed and divided into four groups (as demonstrated in Table 4.1). The brain downward displacements pulled by the gravity were reported varying from 0.5 mm to 7.5 mm, averaging at 3.0 mm (Letteboer et al., 2005).

Since the thickness of CSF layer was modelled only 4 mm based on previous research study (Shahid et al., 2011), the brain shift in gravity direction was incrementally set from 0 mm (control model) to 3.0 mm (75% of possible displacement). After the assignment of boundary conditions and stimulation parameters for all tissue properties, the result was calculated and analysed for each group in the result analysis part.

| Group | Electrode Montage | Lateral Head Orientation | Models with Brain Displacement (mm) | | | | | | |
|-------|-------------------|--------------------------|-------------------------------------|---------------------------|---------------------------|---------------------------|---------------------------|---------------------------|---------------------------|
| | | | M[0] | M[0.5] | M[1.0] | M[1.5] | M[2.0] | M[2.5] | M[3.0] |
| G1 | C3-C4 | Right | M _{C3-C4} [0] | M _{C3-C4} [0.5] | M _{C3-C4} [1.0] | M _{C3-C4} [1.5] | M _{C3-C4} [2.0] | M _{C3-C4} [2.5] | M _{C3-C4} [3.0] |
| G2 | C3-C4 | Left | M _{C3-C4} [0] | M _{C3-C4} [0.5] | M _{C3-C4} [1.0] | M _{C3-C4} [1.5] | M _{C3-C4} [2.0] | M _{C3-C4} [2.5] | M _{C3-C4} [3.0] |
| G3 | C3-Fp2 | Right | M _{C3-Fp2} [0] | M _{C3-Fp2} [0.5] | M _{C3-Fp2} [1.0] | M _{C3-Fp2} [1.5] | M _{C3-Fp2} [2.0] | M _{C3-Fp2} [2.5] | M _{C3-Fp2} [3.0] |
| G4 | C3-Fp2 | Left | M _{C3-Fp2} [0] | M _{C3-Fp2} [0.5] | M _{C3-Fp2} [1.0] | M _{C3-Fp2} [1.5] | M _{C3-Fp2} [2.0] | M _{C3-Fp2} [2.5] | M _{C3-Fp2} [3.0] |

Table 4.1 Twenty-six models applied with different montages, head orientations and brain displacements. Notation M_{C3-C4}[0.5] represents a model applied with C3-C4 electric montage and right lateral head orientation while the brain displacement is 0.5 mm towards the ground

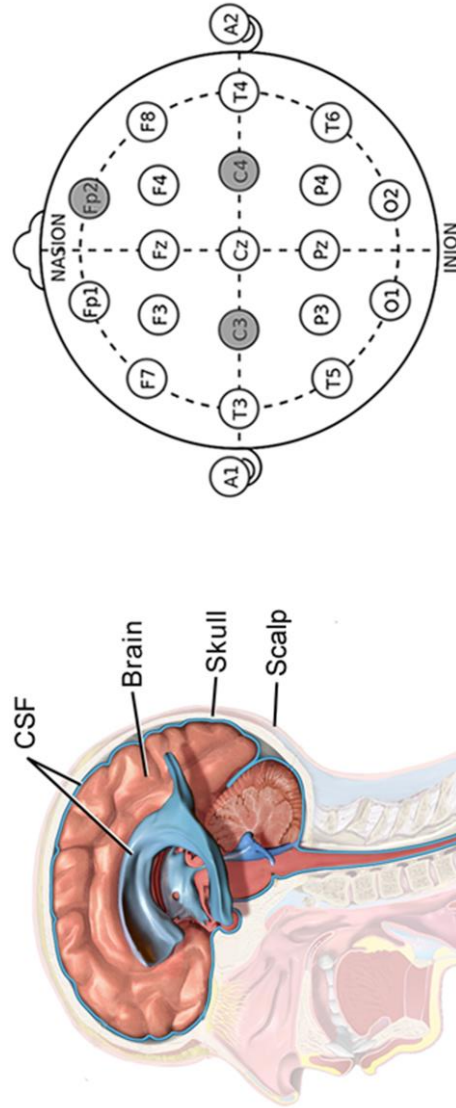


Figure 4.1 Four layers included in this study (Image modified from (Blaus, 2014))
 Figure 4.2 Electrode locations of International 10-20 system for EEG recording (Modified from (トマト 124, 2010))

| Structure | Semi axis (mm) | | | Conductivity (S/m) |
|-----------|----------------|----|----|--------------------|
| | a | b | c | |
| Skull | 70 | 90 | 90 | 0.015 |
| CSF | 66 | 86 | 86 | 1.79 |
| Brain | 62 | 82 | 82 | 0.2 |
| Scalp | | | | 0.43 |
| Electrode | 40×40 | | | 0.14 |

Table 4.2 Parameters assigned to all layers (Scalp dimension is derived from real subject)

4.2. Methods

The models used were developed based on the most characteristic concentric spherical human head model, Rush and Driscoll human head model (R.D Model) (Rush and Driscoll, 1968). However, several major changes were applied to make it a realistic shaped human head model. Specifically, besides the original three layers (scalp, skull and brain) in R.D Model, we implemented another layer representing CSF between skull and brain. All the layers were modelled as concentric ellipsoids, rather than concentric spheres in R.D Model. Based on this model, we set the displacement of brain ellipsoid towards the ground with incremental magnitude (0.5 mm) to simulate the downward movement of brain due to gravity. The regions of interest (ROI) chosen was the whole surface of brain layer and the distribution of current density in this surface was analysed with different electrode montages, head orientations and brain displacements.

4.2.1. Quasi-static Approximation and Boundary Conditions

The electromagnetic properties of a biological medium can be defined by Maxwell's equations. In the frequency range of DC~10 kHz, it is possible to ignore the capacitive, inductive, propagation and time varying effects of the medium because the wavelengths of electromagnetic waves at these frequencies are much longer than the scale of body structures (Baumann et al., 1997b, Nunez and Srinivasan, 2006). Since tDCS utilises direct current, the Quasi-static approximation could be employed in the modelling process. Therefore, all head layers in this study were modelled as passive volume conductors and their intracellular volume-averaged current source was ignored, which complied with quasi-static Laplace equation (Bai et al., 2013b):

$$\nabla \cdot (-\sigma \nabla \phi) = 0 \quad \text{Equation 4.1}$$

where ϕ is the electric potential and σ is the electrical conductivity of a conductive medium. However, ϕ is generally a tensor for anisotropic volume conductors that has inhomogeneous electrical conductivities along different directions. For isotropic volume conductors assumed in this study, ϕ is merely a scalar.

With the quasi-static approximation, the relationships between electric field (\mathbf{E}) and current density (\mathbf{J}) of a point within the conductive medium can be defined in Equation 4.2 and Equation 4.3 (Parazzini et al., 2011):

$$\mathbf{E} = -\nabla\phi \quad \text{Equation 4.2}$$

$$\mathbf{J} = \sigma \mathbf{E}. \quad \text{Equation 4.3}$$

There are two types of boundary conditions (Neumann, Dirichlet) available for the electrodes. Neumann boundary condition sets inward current density \mathbf{J}_n for anode and $-\mathbf{J}_n$ for cathode while Dirichlet boundary condition sets constant voltage V for anode and $-V$ for cathode. And the E-field distributions are almost the same no matter which boundary condition type is chosen though absolute E-field values are slightly different (Bai et al., 2014). For this study, inward current density was applied to anode and cathode.

As air-scalp boundary is generally considered as electric insulating, no current density or ground boundary condition ($\phi = 0$) was applied to the air-scalp boundary while continual current was maintained in all interior tissue-tissue boundaries.

4.2.2. Conductivity Assignment and Geometric Dimensions

In all the models constructed, we assumed that the electrical conductivities of all four layers were homogenous. The electrical conductivity values of Skull and CSF were obtained from literature review (Baumann et al., 1997b, Oostendorp et al., 2000a). Specifically, scalp conductivity was derived from the conductivity values of skin, fat and muscles (Holdefer et al., 2006); Grey matter and white matter contributed to the brain layer conductivity (He, 2004, Datta et al., 2009). The size of all sponge electrodes was modelled as 4.0 cm \times 4.0 cm. The sponge electrodes are typically soaked in saline solution in clinical trials. Therefore, all electrodes were assigned with the conductivity of saline solution (Datta et al., 2009).

The outermost layer, scalp, was modelled from SAM Phantom provided by IEEE, IEC and CENELEC while the geometric dimensions of skull, CSF and brain were scaled with the same ratio in R.D Model to fit in the real shape model (Rush and Driscoll, 1968, Shahid et al., 2011). The geometric dimensions of all layers along with their electrical conductivities are listed in Table 4.2.

4.2.3. Electrode Montages and Stimulation Parameters

The electrode locations assigned in this study complied with the International 10-20 system for Electroencephalography (EEG) recording and as shown in Figure 4.2, Montages C3 (Left M1-motor cortex area) - C4 (Right M1-motor cortex area) and C3 (Left M1-motor cortex area) - Fp2 (Contralateral supra-orbital region) were chosen to simulate the primary motor cortex (Alexandre F et al., 2011, Shahid et al., 2014a). The exposed scalp surface was assigned with ground potential and flux continuity was set to all inner tissue-tissue boundaries. As for the electrodes, the anode remained at C3 position applying with a 1.25 A/m^2 normal inward current density while cathode was separately placed at C4 and Fp2 locations with a -1.25 A/m^2 normal inward current density. Both electrode montages were implemented in all four groups coupled with lateral head orientations and incremental brain displacements (M[0], M[0.5], M[1.0], M[1.5], M[2.0], M[2.5], M[3.0]). Specifically, M[0] was the control model with no displacement of brain ellipsoid while in M[0.5]~M[3.0] models, the displacement were 0.5 mm, 1.0 mm, 1.5 mm, 2 mm, 2.5 mm and 3 mm to the direction of gravity respectively.

4.2.4. Finite Element Model Mesh and Data Computation

Using COMSOL Multiphysics software package, all the models with designed geometry properties (montage, brain displacement etc.) were constructed and assigned with proposed boundary conditions as well as other stimulation parameters. After that, physics controlled mesh was conducted to generate tetrahedral finite elements and the element size was set to extremely fine, which resulted in about 1.3 million elements in each model.

Considering that the surface of brain layer has more neurons in charge, the surface of brain layer was chosen as the only ROI and the distribution of current density on that surface was computed. For each model, four characteristic values were computed from its current density dataset. Namely, they were 99th percentile value, median value, mean value and threshold area (TA). To be specific, 99th percentile, rather than the maximum value, was used to take into account possible computational instabilities. TA was defined as the percentage of surface area where the amplitude of current density was greater than 70% of its 99th percentile. The threshold of 70% was chosen

because it corresponds to the 3dB cut off frequency (J amplitude reduction with respect to the maximum value) (Parazzini et al., 2011).

4.3. Results and Analysis

In this study, 2 mA current was applied to the electrodes and resulted up to 0.413 mA/cm² current density on the scalp beneath the electrodes (about 0.196 mA/cm² in average). However, for most other tDCS studies using saline-socked electrodes, the value they obtained was up to 0.08 mA/cm². That huge difference was because the size of their electrodes (25~35 cm²) were much bigger than the one we modelled (16 cm²). Though the value was 3 times larger, it was still relatively weak and no apparent side effects were reported in similar researches.

Simulation results were obtained and analysed in three parts. Firstly, the current distributions in two control models ($M_{C3-C4}^{Control}[0]$, $M_{C3-Fp2}^{Control}[0]$) were compared, which were applied with C3-C4 and C3-Fp2 electrode configurations respectively (as shown in Figure 4.3). But neither of them was applied with the brain shift (brain displacement was 0 mm). Then, for each electrode montage, both right lateral head orientation and left head orientation were investigated in respect to the increasing brain displacements (0.5~3.0 mm). As demonstrated in Table 4.1, group 1 and group 2 were analysed in the second part while the rest two groups were addressed in the last part.

4.3.1. Analysis of Control Models for C3-C4 and C3-Fp2 Montages

To illustrate the simulation result of the control models for C3-C4 and C3-Fp2 electrode montages, electric potential (V) within all four layers was calculated and their distributions were plotted in Figure 4.3. Though it provided a global view of the current distributions, not too much detailed difference could be observed. In order to well demonstrate the differences, four feature values of current density (J) distributed on the brain layer surface were chosen in the investigation.

Table 4.3 shows the 99th percentile, median and mean values of current density (J , A/m²). Based on the 99th percentile value, the threshold area (TA, %) was also calculated. Those characteristic values revealed huge difference in the distributions of current density in the models with different electrode configurations. Apparently

control model with C3-C4 montage had relatively higher current density (6.406×10^{-2} A/m²) than the control model with C3-Fp2 montage (4.950×10^{-2} A/m²). Because under the C3-C4 montage, the electrodes were placed close together, thus increasing the focality significantly. This result also supported the finding of previous work by Faria et al. in 2011 (Faria et al., 2011) and even earlier analytical studies (Rush and Driscoll, 1968, Weaver et al., 1976). However, the mean and median values of C3-Fp2 control model were higher than those of the C3-C4 control model and the threshold area also showed the same trend, which was even 3 times larger. This result complied with the previous studies that the amount of current penetrating through the scalp is reduced with the increasing distance of stimulation electrodes (Miranda et al., 2006, Datta et al., 2008b).

| | 99th Percentile (E-2) | Median (E-3) | Mean (E-3) | Threshold Area (%) |
|-----------------------------------|-----------------------|--------------|------------|--------------------|
| $M_{C3-C4}^{\text{Control}} [0]$ | 6.4068 | 1.9270 | 7.089 | 2.6160 |
| $M_{C3-Fp2}^{\text{Control}} [0]$ | 4.9509 | 4.055 | 10.185 | 9.1446 |

Table 4.3 Four feature values of the current density distribution (A/m²) in the brain surface of control models with C3-C4 and C3-Fp2 electrode configurations

4.3.2. Analysis of Models with C3-C4 Montage

Under C3-C4 montage, both right and left head orientations were numerically investigated by analysing the current distributions on the brain surface. As declared in Table 4.1, models in group 1 (G1) and group 2 (G2) were applied with right lateral head orientation and left lateral head orientation respectively. Both G1 and G2 were investigated by implementing 6 models ($M_{C3-C4} [0.5] \sim M_{C3-C4} [3.0]$) applied with incremental brain shift (0.5 mm) in compare of the control model for C3-C4 montage ($M_{C3-C4}^{\text{Control}} [0]$). Therefore, both groups contained 7 models with different brain shifts and their differences in the current density distributions were discussed by analysing three characteristic values (99th percentile, median and TA) of current density described before.

Figure 4.4 (a) describes the trend of three key feature values of 7 models from G1. Specifically, M[0] represents the control model while M[0.5] is simplified for $M_{C3-C4}^{\text{Right}} [0.5]$ (model applied with C3-C4 montage and right lateral head orientation while the brain shift was 0.5mm), and so on and so forth for the rest notations. As can

be clearly observed, with the gradual increase of brain displacement, the values of 99th percentile and TA respectively increased about 6.5% and 21% while the median value almost remained the same ($1.8 \times 10^{-3} \sim 1.9 \times 10^{-3} \text{ A/m}^2$). Since only a small proportion of current applied on the electrodes penetrates through the skull and other layers to stimulate the cortex, the current density on the brain surface was scaled by Log_{10} and the normalised values were classified into eight bins (Bin1~Bin8). Figure 4.4 (b) revealed that with the increase of brain shift, the fraction volume of normalised current density in peak range (Bin8) also raised 24% and that in the off peak ranges of Bin7 and Bin4 declined about 12% and 5%, respectively. As for the normalised current density in other bins, they slightly fluctuated but could be still considered remaining at the same level as that of the control model.

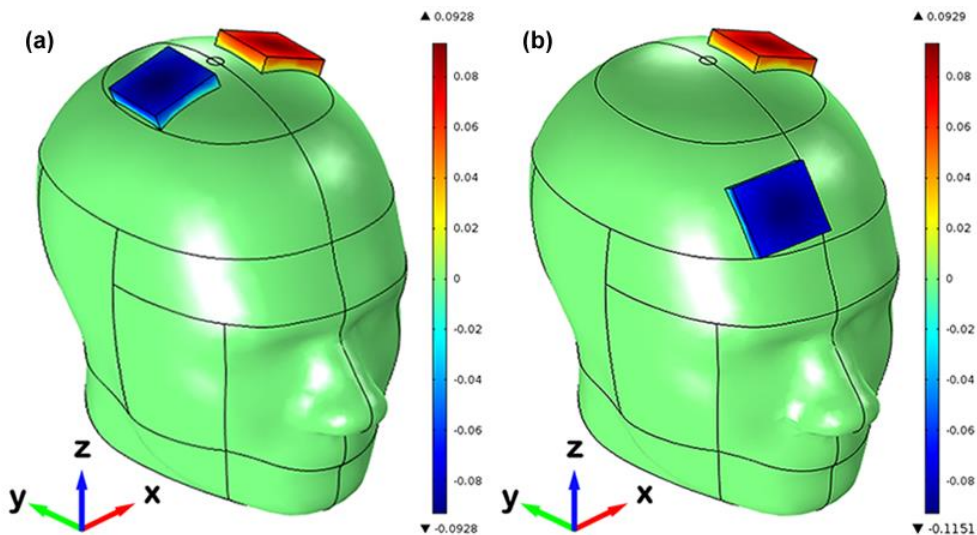


Figure 4.3 Electric potential distributions in the control models of C3-C4 (a) and C3-Fp2 (b) montages

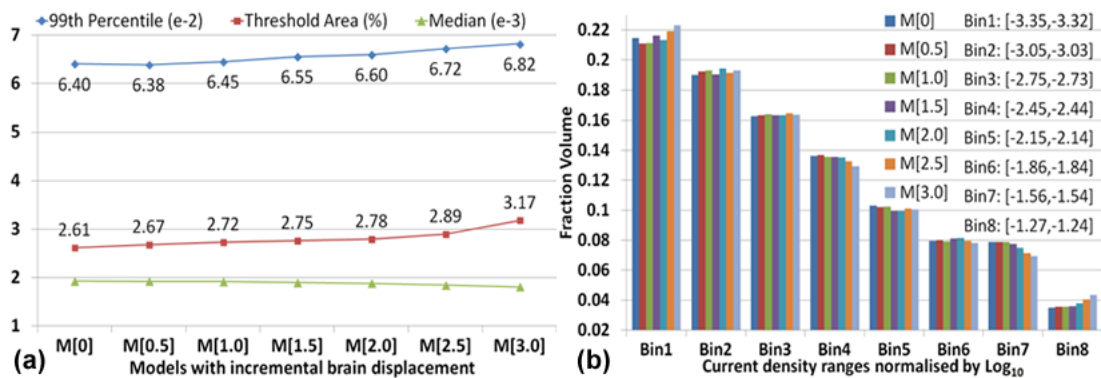


Figure 4.4 Current density distributions on the brain surface of models with incremental brain displacements under C3-C4 electrode montage and right lateral head orientation (a: The distributions of three key features of current density; b: The fraction volume distributions of Log_{10} normalised current density)

As shown in Figure 4.5(a), the same trend could also be observed under the configuration of C3-C4 montage and the left lateral head orientation. To be specific, with the gradual increase of brain displacement, the values of 99th percentile and TA respectively increased about 5.9% and 23.8% while the median value nearly still stayed at the same level ($1.8 \times 10^{-3} \sim 1.9 \times 10^{-3} \text{ A/m}^2$). A similar normalised current density distribution could be seen from Figure 4.5(b). The fraction volume of normalised current density in peak range (Bin8) increased about 24% and the scaled value of Bin7 and Bin4 declined about 13% and 4.9%. And the normalised current density in other bins almost remained at the same level. The tiny difference between the results of right lateral head orientation and left head orientation models was because that the geometry of this model, especially for the scalp layer, was not exactly symmetric.

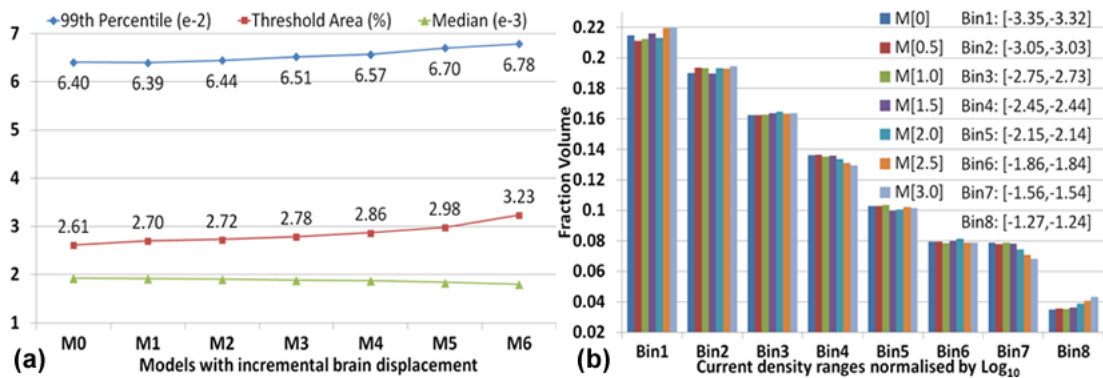


Figure 4.5 Current density distributions on the brain surface of models with incremental brain displacements under C3-C4 electrode montage and left lateral head orientation (a: The distributions of three key features of current density; b: The fraction volume distributions of Log₁₀ normalised current density)

These findings implied that under the configuration of C3-C4 montage, no matter which lateral head orientation was applied, the increase of brain shift could bring more current through the scalp and reached the target region of brain surface. As a result, it gradually enhanced the stimulation effect on the primary motor cortex. However, as can be seen from the top two groups (G1 and G2) in Figure 4.6, with the increase of brain displacement, the center of target region was shifting. G1 was configured with right lateral head orientation and the target region center was shifting from the brain cortex to the middle of C4 spot and brain cortex. On the contrary, the stimulation center was moving to the middle of C3 spot and brain cortex when left lateral head orientation was applied (G2).

4.3.3. Analysis of Models with C3-Fp2 Montage

Exactly the same methods were applied to look into the result derived from Group 3 and Group 4 models in Table 4.1 (G3, G4), which were applied with C3-Fp2 electrode configuration, right lateral head orientation and left lateral head orientation, respectively. The ROI under this montage was also the brain layer only.

Figure 4.7(a) demonstrates the variation of 99th percentile, median and TA of 7 models from G3. It is apparent to conclude that, with the moderate growth of brain displacement, the values of 99th percentile increased about 10% while TA declined approximately 12% and the median value declined a small portion (3%). Figure 4.7(b) disclosed that with the increase of brain shift, the fraction volume of normalised current density in peak range (Bin8) declined about 27% while that in the off peak ranges of Bin7 and Bin1 increased about 15% and 6%. As for the normalised current density in other bins, they slightly fluctuated but could be still regarded at the same level because the changing gap was less than 1.9 %, which could be considered as stable on the same level of the control model.

However, when the left head orientation was applied, with the increase of brain shift, a different trend could be observed from Figure 4.8(a) because there was no linear relationship between the growths of brain shift and the two key feature values (99th percentile and TA) whilst the median value of current density was nearly stabilized at $4 \times 10^{-3} \text{ A/m}^2$. To be specific, when the brain displacement was modelled as a small quantity (0.5 mm), both the 99th percentile and TA declined slightly (0.7% and 0.6%) and they returned to the same level of control model when the brain displacement was applied as 1.0 mm. Then, with the growth of brain displacement, the values of 99th percentile and TA were linearly increased approximately 9% and 7%, respectively. In terms of the median value, it declined an extremely small percentage (0.7%) and it could be considered as negligible when compared with the value of G3, which suggested that, with the increase of brain shift, the amount of current penetrating the outer layers and reaching the brain surface remained almost the same level. From Figure 4.8(b), it is easy to discover that $M_{C3-Fp2}^{\text{Left}}[0.5]$ had a slightly higher normalized current density than the control model in the peak range (Bin8) and then with the increase of brain shift, the normalized current density in Bin8 declined about 16%. The

normalized current density in off peak ranges Bin7 and Bin1 increased 4% and 6% respectively while less than 2% variation gap could be observed for all the rest bins.

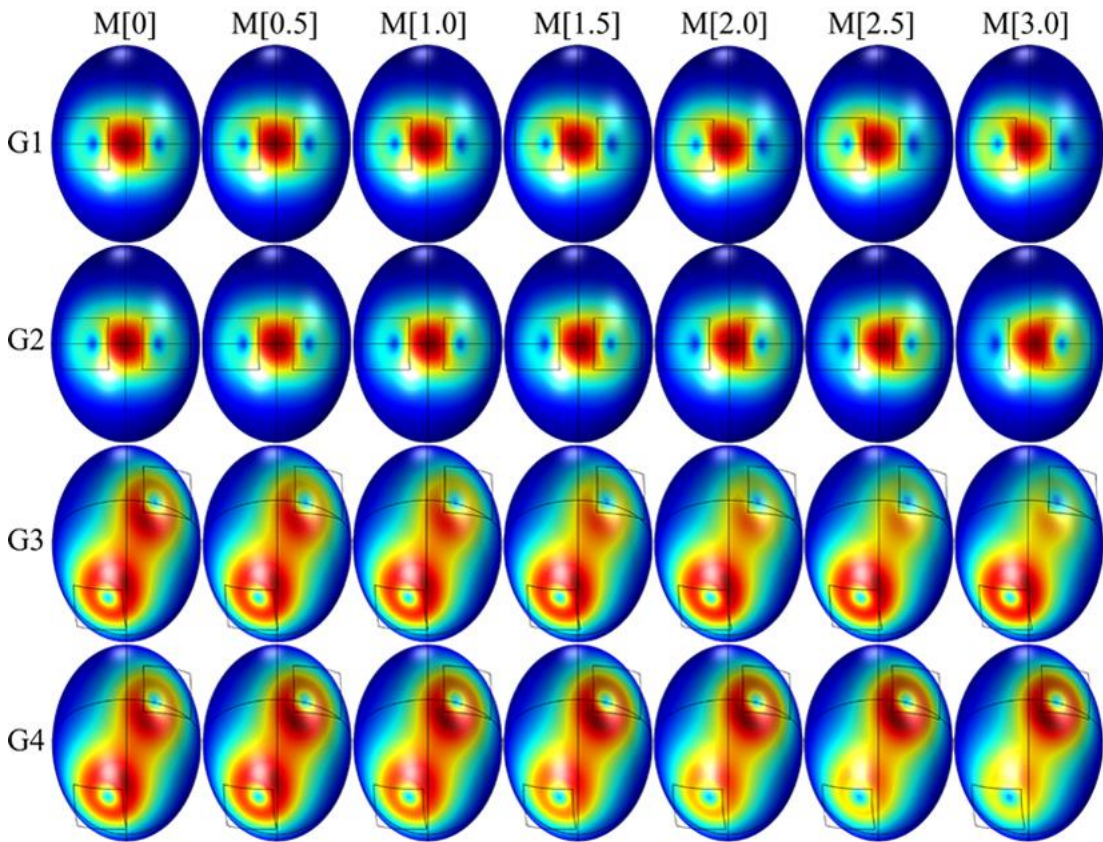


Figure 4.6 Plot of current density distributions on the brain surface of all the models listed in Table 4.1 and the right square pads in all four groups are the anode electrode placed at C3 location while the left ones are cathode electrode configured at C4 (G1, G2) and Fp2 (G3, G4) locations respectively

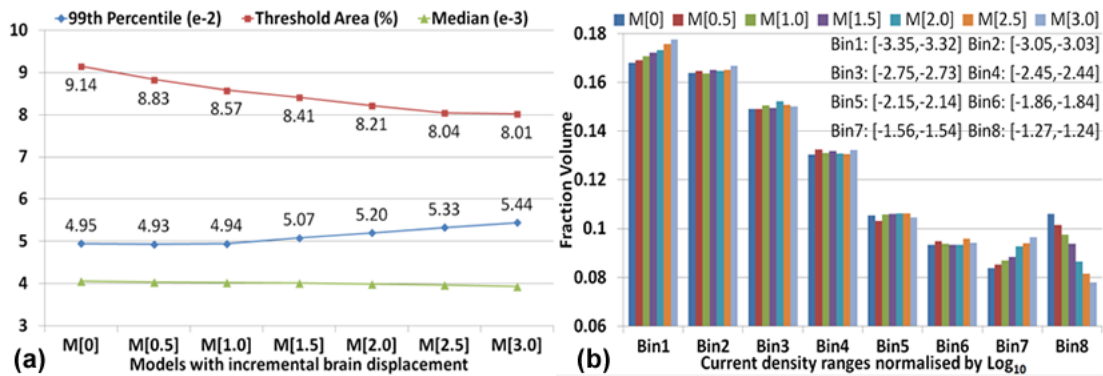


Figure 4.7 Current density distributions on the brain surface of models with incremental brain displacements under C3-Fp2 electrode montage and right lateral head orientation (a: The distributions of three key features of current density; b: The fraction volume distributions of Log_{10} normalised current density)

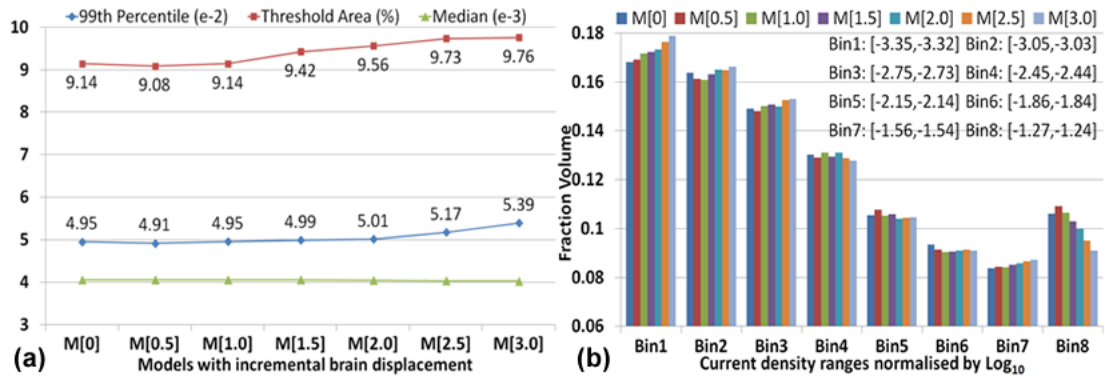


Figure 4.8 Current density distributions on the brain surface of models with incremental brain displacements under C3-Fp2 electrode montage and left lateral head orientation (a: The distributions of three key features of current density; b: The fraction volume distributions of Log_{10} normalised current density)

These findings implied that under the configuration of C3-Fp2 montage, with the increase of brain shift, huge differences could be observed in the current distributions when different lateral head orientations were applied. As demonstrated in Group 3 (G3) and Group 4 (G4) of Figure 4.6, when the brain shift was increased under different lateral head orientations, the center of target region was also moving to different directions. Specifically, when no lateral head orientation was applied ($M_{C3-Fp2}^{\text{Control}}[0]$), two focuses could be identified in the target regions and they were the left primary motor cortex near the anode at C3 and right supra-orbital near the cathode at Fp2. However, when the right lateral head orientation was applied (G3), with the growth of brain shift, the focus at left primary motor cortex was compromised and at the same time, the other focus at right supra-orbital was strengthened and this local stimulation enhancement was achieved at a cost of the deterioration of the global TA. On the contrary, when the left lateral head orientation was applied (G4), the focus at the right supra-orbital was weakened and the focus at the left primary motor cortex was boosted. As a result, the local stimulation of left primary motor cortex was promoted though this promotion was not as strong as it in G3. With the increase of brain shift, the global TA in G4 was not undermined, except when the brain shift was set to 0.5mm. But it was soon recovered and finally surpassed the original level in the control model ($M_{C3-Fp2}^{\text{Control}}[0]$), which was significantly higher than the TA in G3.

4.4. Discussions

This study has investigated the distribution of current density on the brain surface under the different configurations of electrode montages (C3-C4 and C3-Fp2), lateral head orientations (left and right) and brain displacements (0 mm ~ 3.0 mm) by constructing a four-layer real shaped human head model. The experiment results and interpretations were focused on revealing the influence of brain shift on the distribution of current density on the brain surface, which were carried out by analysing three feature values (99th percentile, median and TA) and the distribution of log10 normalised current density in four groups (G1~G4).

4.4.1. Model Formulation

The real shaped human head model was constructed to host four layers to represent the tissues of scalp, skull, CSF and brain. Compared with the early spherical models, two major improvements have been made by modelling the outermost layer (scalp) as the real shape of an adult and the rest layers (skull, CSF and brain) as concentric ellipsoids according to their geometry radius ratio in R.D model. Though this model made an advancement to derive more realistic stimulation result than spherical human head models, it did not include enough tissue types and real geometry features. No anisotropic electrical conductivity was considered for the brain tissue. However, with limited tissue types and geometry features, this model is still able to reveal that the brain shift had sensitive effects on the current distributions during tDCS. And considering that the anisotropic electrical conductivity properties are generally considered to obtain more accurate result in the experiments investigating the current distributions within GM and WM, the lack of anisotropic electrical conductivity should not have too much influence on the result derived as the ROI chosen in this study was merely the brain surface, rather than the whole brain regions (Suh et al., 2009, Wolters et al., 2006, Suh et al., 2012). Therefore, the four-layer real shaped human head model was robust enough to validate the hypothesis proposed in this study.

4.4.2. Comparison of Two Electrode Montages

Two electrode montages (C3-C4 and C3-Fp2) are frequently used for the enhancement of motor performance of the non-dominant hand (C3-C4) and primary motor cortex of emotional and psychomotor functions (C3-Fp2) (Boggio et al., 2006a, Boggio et al.,

2007, Utz et al., 2010, Koenigs et al., 2009). The simulation results derived from the control models of both montages suggested that the peak current density discovered on the brain surface was depended on the placement of electrodes. For symmetric electrode placement of C3-C4, the maximum current density was found right between the electrodes (M[0] of G1 and G2) while, in terms of asymmetric electrode montage of C3-Fp2, two peaks of current density could be identified beneath the adjacent corners of both electrodes (M[0] of G3 and G4). This finding corresponded to previous studies (Peterchev et al., 2010, Datta et al., 2008b, Wagner et al., 2007a). Besides, by comparing the mean, median and TA values of Table 4.3, more current could penetrate the out tissue layers (scalp, skull and CSF) and reach the brain layer under the C3-Fp2 montage due to that the inter-electrode distance in such montage was much bigger than it in C3-C4 montage, which decreased the shunting phenomenon of the current through the out layers (Faria et al., 2011). However, the close inter-electrode distance in C3-C4 montage brought more focal current in the target region as its 99th percentile value was 1.3 times of it in C3-Fp2.

4.4.3. Variations of Brain Displacement

To demonstrate the downwards displacement of brain caused by gravity under different electrode montages and lateral head orientations, incremental increase of the brain shift was applied as previous intraoperative studies reported a varied range of brain displacement (Hu et al., 2007, Letteboer et al., 2005). From the result of G1 and G2 with the electrode configuration of C3-C4, longer brain displacement could bring stronger stimulation effect on the primary motor cortex and the focus of target region also slightly shifted downwards to the ground direction. However, in terms of C3-Fp2 electrode configuration, the asymmetric electrode location determined different influences brought by the brain displacement under different lateral head orientations. In G3, higher brain shift caused a shrink of stimulation region while the area was fluctuating in G4 and determined by the extent of brain shift, which makes its application tricky for the future clinical trials as customized treatment is needed to cope this situation. Still, in both lateral head orientation under C3-Fp2, higher brain shift brought local enhancement of current density and this could be an important factor to consider during tDCS treatments.

4.5. Conclusions

The head geometry is modified in a small scale as the gravity pulls the brain slightly downward and changes the distribution of CSF. This chapter investigated four groups of models with different electrode montages and lateral head orientations. For each group, the slight geometry change was numerically generated by assigning incremental brain downward displacement. This study allowed us to investigate how sensitive the current density distribution on the brain surface due to this alteration and how significant the influence was. The results demonstrated two major outcomes. Firstly, the downward movement of brain made itself closer to one electrode (anode or cathode) and enhanced the stimulation of the brain region beneath that electrode at a cost of undermining the stimulation the other electrode. Secondly, the overall current penetrated and current distributions on the majority of other brain regions remained almost unchanged at the same time. Therefore, the impact of lateral head orientations discovered in this study is helpful in the predication of stimulation results for the clinical practice in electrical neurophysiological modulation and mental health.

5. INFLUENCE OF BRAIN TUMOR ON THE INDUCED CURRENT DISTRIBUTION PATTERN

According to the latest annual cancer surveillance report jointly released by the American Cancer Society (ACS), the Centers for Disease Control and Prevention (CDC), the National Cancer Institute (NCI), and the North American Association of Central Cancer Registries (NAACCR), brain and other nervous system cancer caused 7.8 and 5.7 deaths per 100,000 persons for men and women specifically in America (Edwards et al., 2014). Another report released by ACS estimated 23,380 new cases and 14,320 deaths claimed by brain and other nervous system cancer in America in 2014 (Siegel et al., 2014). Brain tumor frequently associates with neoplasm that is caused by uncontrolled cell proliferation and World Health Organization (WHO) ratified the most widely used I–IV grading system to classify tumors with increasing aggressive degree (Bauer et al., 2013, Kleihues et al., 1993). Both in vivo and in vitro studies have confirmed that tumors exhibit much higher electrical conductivity (up to 7.5-fold) and electrical permittivity (up to 5-fold) than the normal surrounding tissue because of the increased cellular water and salt content, altered membrane permeability, changed packing density, and orientation of cells. In addition, higher grade tumors are also reported to have higher electrical conductivity (Gabriel et al., 1996a, Fricke and Morse, 1926, Halter et al., 2011, Scholz and Anderson, 2000, Zou and Guo, 2003, Van Lier et al., 2011, Smith et al., 1986).

Four sections are included in this chapter. Following the background information of brain tumor is the Introduction which presents the electrical treatment. The method and model design are described in the second section. After that, the computation and result are reported and analysed in the third section. Discussion of the brain tumor influence on the current distributions during tDCS is made in the final section.

5.1. Introduction

Early researches have enabled neuroscientists to draw conclusions that direct electrical stimulation of the human cortex induces behavioural changes and neuroplastic alterations of cortical excitability (Zago et al., 2008, Bindman et al., 1964a). However, almost all of current studies only focused on the mental disorders that can hardly result in anatomical or morphological distortions in the cortex. Particularly, few of them attempted to explore the current distributions of tDCS in a human head model that has structural abnormalities caused by brain tumors. Figure 5.1 illustrates the MRI scans of a brain tumor in the left frontal lobe (Kaus et al., 2001).

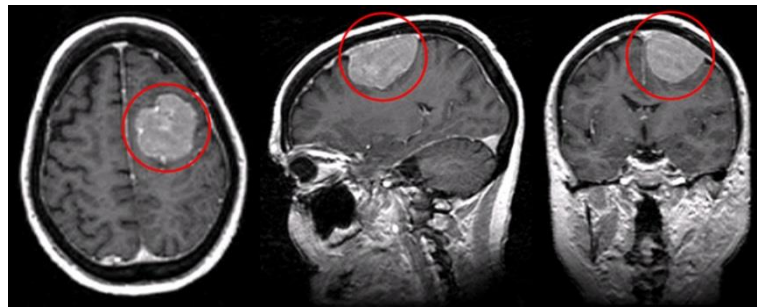


Figure 5.1 Illustration of a brain tumor (Highlighted with red circle) harbored in the left frontal lobe in transverse, sagittal and coronal planes.

This chapter composed to numerically investigate the influence of tumor grade on the current distribution patterns of brain cancer patients during the application of tDCS. The simulation experiments were developed to accommodate a series of high resolution human head models with different brain tumors locations and varied electrode montages. The anatomically accurate human head model and brain tumors were constructed from MRI datasets (T1, T2 and PD-MRI). About five electrode configurations (F3-Fp2, C3-C4, C3-Fp2, P3-C4 and P3-Fp2) were applied to the models individually and the sponge electrodes were all squared ones with $5 \times 5 \text{ cm}^2$ dimension.

For each electrode configuration, there was a control model without brain tumor. The healthy control models contained eighteen head tissues and when it comes to the proposed model with brain tumors, the brain tumor was derived from another MRI dataset of a patient with brain tumor, which was then manually merged into the

controls and configured with different locations within the brain. With the developing of brain tumors, their electrical conductivity demonstrates an increasing trend due to the accumulation of conductive media and deterioration of membrane. Therefore, brain tumors in different grade were simulated by assigning their corresponding electrical conductivities.

5.2. Method and Model Design

Firstly, a set of high resolution realistic human head models integrated with a brain tumor were constructed. Then these models configured with different electrode montages and tumor locations were meshed into finite element models. Finally the simulations were carried out after the boundary conditions and tissue properties were assigned properly.

5.2.1. Image Segmentation and Mesh Generation

In this study, the baseline head model was derived from the previous studies in our research group (Shahid et al., 2012, Shahid et al., 2013b). The utilized human head MRI datasets were obtained from the Simulated Brain Database of BrainWeb, which provided an MRI simulator to generate a set of MRI data volumes by varying imaging parameters and artifacts (Cocosco et al., 1997, McConnell Brain Imaging Centre, 2014). For the brain tumor dataset, it was obtained from the Surgical Planning Laboratory (SPL) and the Department of Neurosurgery (NSG) Brain Tumor Database (Kaus et al., 2001, Warfield et al., 2000). Each human head dataset volume has 1mm^3 isotropic voxel resolution and contains $181 \times 181 \times 217$ slices in the transverse, sagittal and coronal axes. T1-weighted MRI volume was applied for the tissue identification and segmentation of GM, WM, fat, muscles (temporalis and extraocular muscles), eyes (vitreous body and lens) and scalp. In addition, T2-weighted and Proton Density (PD) MRI volumes were used for the segmentation of cerebrospinal fluid (CSF) and inner skull boundaries. FMRIB's Software Library (FSL) platform (Smith et al., 2004) was deployed to derive tissue masks of scalp, skull, CSF, WM, GM and nine subcortical structures (hindbrain, hippocampus etc.) whereas module ScanIP from commercial

software package Simpleware 4.3 was applied for the semiautomatic generation of fat, muscles and eyes.

The brain tumor mask was obtained from a patient (case6) in SPL and NSG Brain tumor Database who was diagnosed with low grade glioma in the right frontal brain. This patient-specific case was selected for two reasons. Specifically, the natural of the brain tumor in case6 was consistent with the interest of this study by its original tumor location and tumor grade, which was further explored as well in Chapter 6. Moreover, MRI scans of the brain tumor in case6 had relatively high quality and it was also apparent to distinguish the boundaries between the tumor and normal brain tissues, which made it easier to verify the obtained brain tumor mask. The volume of this tumor is $3.28 \times 10^4 \text{ mm}^3$ and its surface area covers $1.49 \times 10^4 \text{ mm}^2$. After the healthy control model was constructed in Simpleware, the mask of a brain tumor derived from the MRI dataset was imported in different regions of interest (ROI). Specifically, these locations are superficial right frontal lobe (RFL) and buried left occipital lobe (LOL) regions.

After manual correction, the models were meshed using +FE Free meshing algorithm in Simpleware and the compound coarseness was set to -15 whereas the region of tumor was further refined by setting the mesh size to 0.8mm. The derived volumetric finite element models contain 8 million tetrahedral elements and each simulation took approximately one hour for an 8-core workstation.

5.2.2. Electrode Montages and Tumor Locations

The electrode configurations applied in this study were consistent with the International 10-20 system for EEG recording. Electrode montage of C3 (Left M1-motor cortex area) - Fp2 (Contralateral supra-orbital region) was selected and modelled to stimulate the primary motor cortex and contralateral supraorbital regions, which was also commonly used in many other studies, including cancer pain control (Shahid et al., 2014a, Shahid et al., 2013b, Silva et al., 2007). Another four electrode configurations (F3-Fp2, C3-C4, P3-C4 and P3-Fp2) are supplemented to explore the influence of electrodes inter distance on current distributions in the brain with tumors. Specifically, the inter electrode distances in the utilized montages (F3-Fp2, C3-C4,

C3-Fp2, P3-C4 and P3-Fp2) are 91 mm, 126 mm, 143 mm, 156 mm and 199 mm, respectively.

Tumor location is considered to be the lobe or region of the brain that the bulk of the oligodendroglioma resides (Zlatescu et al., 2001) and the lesion location generally determines the side effects with its growth, which interferes the normal brain functionalities that the specific region previously dominates. In this study, the original glioma location was harbored in the right frontal lobe (RFL) that plays a role in non-literal language, personality and emotions, and self-awareness (Shammi and Stuss, 1999). As a contrast, the same brain tumor was also placed in the left occipital lobe (LOL) that dominates visual processing (Grill-Spector et al., 1998).

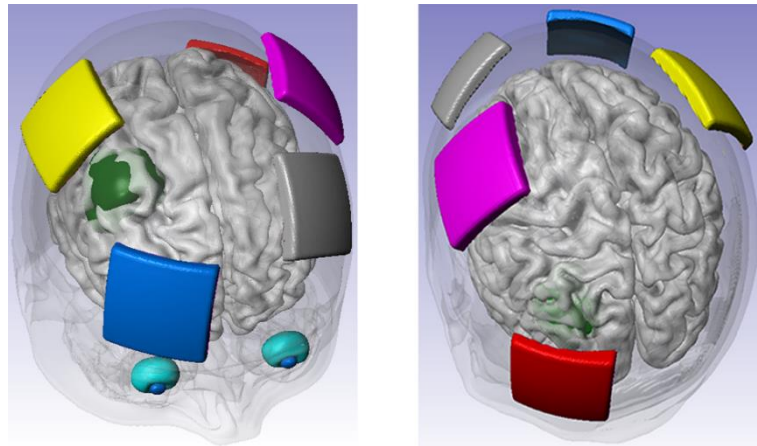


Figure 5.2 Demonstration of tumor locations (Black green bulk: Tumor in RFL; Light green bulk: Tumor in LOL) and electrodes for five montages (Cathode electrode: blue pad in Fp2 and yellow pad in C4; Anode electrode: grey pad in F3, magenta pad in C3 and red pad in P3).

In this study, five primary groups of human head models were configured with different electrode montages (F3-Fp2, C3-C4, C3-Fp2, P3-C4 and P3-Fp2) and tumor locations (RFL, LOL). As an illustration example, we chose one group to present in detail, which was configured with the most commonly used anti-pain montage (C3-Fp2) for both proposed tumor locations. Figure 5.2 indicates the locations of all proposed electrodes and tumors.

5.2.3. Electrical Properties and Tissue Conductivity

Quasi-static approximation could be applied in this study because it also falls in the low frequency range under 10 kHz. The boundary conditions utilized in chapter 4 were assigned in this chapter as well. For each simulation, 0.8 A/m^2 inward current density (equivalent to 2 mA) was applied to the exposed anode surface using Numann boundary condition while Dirichlet boundary was configured to define electrical potential V (ground potential) on the cathode surface.

| Material | Conductivity (S/m) | Reference |
|-------------------------------------|---------------------------|----------------------------|
| Saline soaked electrodes | 1.4 | (Datta et al., 2009) |
| Scalp | 0.43 | (Shahid et al., 2014a) |
| Fat | 0.025 | (Gabriel et al., 1996a) |
| Temporalis and eye muscles | 0.16 | |
| Eyes | 0.5 | |
| Eye lens | 0.31 | (Gabriel et al., 1996b) |
| Skull | 0.015 | (Oostendorp et al., 2000a) |
| CSF | 1.79 | (Baumann et al., 1997b) |
| GM | 0.32 | (Gonçalves et al., 2003) |
| WM | 0.15 | (Nicholson, 1965) |
| Hindbrain | 0.25 | (Geddes and Baker, 1967) |
| Red Nucleus | | |
| Globus pallidus pars interna | 0.32 | (Gonçalves et al., 2003) |
| Globus pallidus par externa | | |
| Caudate nucleus | | |
| Fornix Crura | | |
| Hippocampus | | |
| Thalamus | | |
| Putamen | | |

Table 5.1 Conductivity of Electrodes and Tissues

In this study, nineteen normal tissue regions (excluding brain tumors and electrodes) were identified and accommodated in all primary models. Electrodes were modelled as $5 \text{ cm} \times 5 \text{ cm}$ sponge pads and in conventional tDCS applications, they are generally soaked in saline solution to conduct electrical current smoothly. Therefore, sponge electrodes were assigned with the conductivity of saline solution (Datta et al., 2009). Table 5.1 lists the conductivity values of all normal tissues and electrodes with literature references.

For the conductivity of brain tumors, inconsistent values were reported in several studies due to the variations of brain tumor locations and grades. However, the majority of them agreed on the enhancement of brain tumor's electrical conductivity, which is relatively higher than the value of the normal surrounding grey matter and white matter (Voigt et al., 2011, Garcia et al., 2011, Zhang et al., 2013, Katscher et al., 2013, Van Lier et al., 2011, Meng et al., 2013, Lier et al., 2014). The conductivity boost is attributed to the membrane degeneration of tumor cells and the permeable increase of water-soluble substances. As a consequence, charge carriers of biological organisms, like positively charged sodium, potassium, magnesium, calcium and negatively charged electrons, are increasingly accumulated within the tumor (Seeger and Wolz, 1992, Ho, 1996, Scholz and Anderson, 2000). Furthermore, the conductivity difference between tumor-like white matter and tumor-like grey matter was reported and strong correlations between tissue malignancies and dielectric properties was found (Chen et al., 2008, Meng et al., 2013). In this study, the brain tumor was further segmented into cancerized white matter (CWM) and cancerized grey matter (CGM). Their conductivities in different grades were adjusted according to their cancerization degree in reported conductivity range. Specifically, the conductivity of the CWM and CGM in grade I brain tumors was set to 10% typically higher than that of the surrounding healthy WM and GM. When it comes to grade IV, their conductivity was set equivalent to the level of CSF (Katscher et al., 2009, Lier et al., 2014, Van Lier et al., 2011). Accordingly to the cancerized development, the range between them were scaled to derive the conductivity of the CWM and CGM in grades II and III, correspondingly (Chen et al., 2008).

| Tumor Grade | Conductivity (S/m) | |
|-------------|--------------------|------|
| | CWM | CGM |
| Control | 0.15 | 0.32 |
| I | 0.56 | 0.68 |
| II | 0.96 | 1.05 |
| III | 1.37 | 1.41 |
| IV | 1.77 | 1.77 |

Table 5.2 Conductivity of the Brain Tumor Conductivity assigned to the tumor confined regions in the control models and tumors components of different grades in other proposed models.

5.2.4. Simulation Parameters and Models Notation

For each simulation, 0.8 A/m^2 inward current density (equivalent to 2 mA) was applied to the exposed anode surface using Numann boundary condition. Input parameters including electrode montages (F3-Fp2, C3-C4, C3-Fp2, P3-C4 and P3-Fp2), tumor locations (RFL, LOL) and tumor grades (I-IV) were separately investigated in groups to explore their influences on the current distributions within the cortex and brain tumors during tDCS. All primary models are divided into five groups (G1-G5) and their notations are shown in Table 5.3.

| Group | Model Alias | Electrode Montage | Tumor Location | Tumor Grade |
|-----------|---|-------------------|----------------|-------------|
| G1 | $M_{RFL \text{ Control}}^{F3-Fp2}, M_{RFL \text{ I-IV}}^{F3-Fp2}$ | F3-Fp2 | RFL | N/A, I - IV |
| | $M_{LOL \text{ Control}}^{F3-Fp2}, M_{LOL \text{ I-IV}}^{F3-Fp2}$ | | LOL | |
| G2 | $M_{RFL \text{ Control}}^{C3-C4}, M_{RFL \text{ I-IV}}^{C3-C4}$ | C3-C4 | RFL | N/A, I - IV |
| | $M_{LOL \text{ Control}}^{C3-C4}, M_{LOL \text{ I-IV}}^{C3-C4}$ | | LOL | |
| G3 | $M_{RFL \text{ Control}}^{C3-Fp2}, M_{RFL \text{ I-IV}}^{C3-Fp2}$ | C3-Fp2 | RFL | N/A, I - IV |
| | $M_{LOL \text{ Control}}^{C3-Fp2}, M_{LOL \text{ I-IV}}^{C3-Fp2}$ | | LOL | |
| G4 | $M_{RFL \text{ Control}}^{P3-C4}, M_{RFL \text{ I-IV}}^{P3-C4}$ | P3-C4 | RFL | N/A, I - IV |
| | $M_{LOL \text{ Control}}^{P3-C4}, M_{LOL \text{ I-IV}}^{P3-C4}$ | | LOL | |
| G5 | $M_{RFL \text{ Control}}^{P3-Fp2}, M_{RFL \text{ I-IV}}^{P3-Fp2}$ | P3-Fp2 | RFL | N/A, I - IV |
| | $M_{LOL \text{ Control}}^{P3-Fp2}, M_{LOL \text{ I-IV}}^{P3-Fp2}$ | | LOL | |

Table 5.3 Notations for All Models

Note: Notation $M_{RFL \text{ I}}^{C3-Fp2}$ represents the model applied with C3-Fp2 montage and harbored a grade I brain tumor in the right front lobe. Other notations have similar representing meaning; 2. The group is ordered according to their inter electrode distances as stated before.

5.3. Computations and Results

The simulations and results of all models are organized into three parts. In the first part, the results from the models with the RFL brain tumor were obtained and analyzed to investigate the influence of the FRL brain tumor in growing grade under different electrode configurations. After that, the results from the models with the LOL brain tumor were addressed to explore the influence of different grade LOL brain tumor

under all the proposed montages. However, only the results from the third group (G3) with the typical anti-pain electrode montage (C3-Fp2) were demonstrated in graphs with progressing details and the results from other groups were summarized in line charts. To explain the results clearly, the concept of threshold area (TA) is introduced in this study. The TA is defined as the volume fraction of a tissue (or region) that has 70% or higher current density than the 99th percentile of the maximum current density (referred as peak current density to avoid calculation errors) within the tissue or region, which is deemed as an indicator to reflect the stimulation outcome (Parazzini et al., 2011).

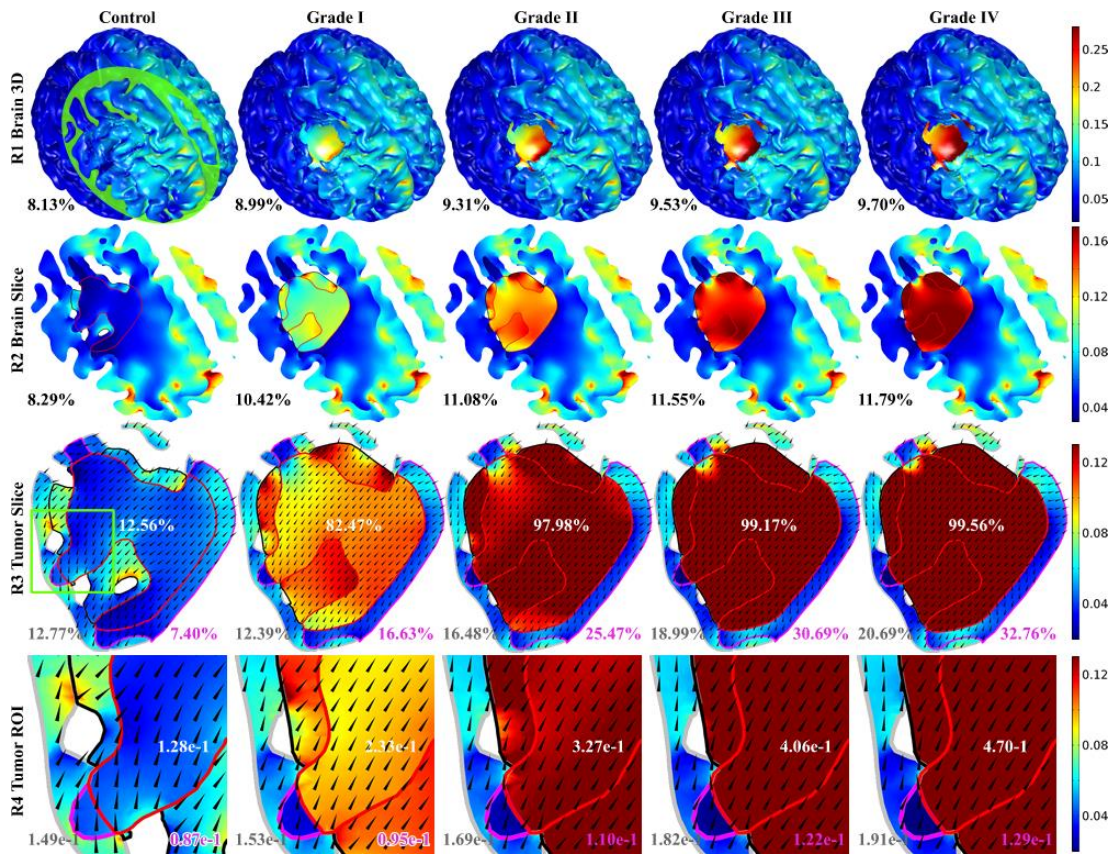


Figure 5.3 The current density J (A/m^2) distributions for simulations of the RFL brain tumor in different grades under C3-Fp2 montage. The first row (R1) shows the 3D brain plots and the 55-degree slice of right frontal brain (green plane) is shown in R2. R3 demonstrates the sliced tumor (black and red contours), normal surrounding GM (grey contour) and WM (magenta contour) whereas R4 zooms in the ROI (green squared region in R3). Black cones in R3 and R4 depict the current directions; the percentage statistics in R1 and R2 are the TA of GM and WM whereas the values in R3 and R4 represent TA and peak current density of tumor, normal adjacent GM and WM in their corresponding contour color.

5.3.1. Influence of the RFL Brain Tumor

In this section, the RFL tumor in growing grade under C3-Fp2 electrode montage was simulated and its influence on the current distributions is demonstrated in Figure 5.3 with progressive structural details from the first row (R1) to the fourth row (R4). The results from other models with the RFL brain tumor were summarized into line charts afterwards.

Under C3-Fp2 montage (Figure 5.3), TA values of the normal GM (R1) and WM (R2), RFL brain tumor and adjacent WM of it (R3) showed a linear relationship between their TA values and the tumor grade. Specifically, compared with the control model ($M_{RFL\ Control}^{C3-Fp2}$), the TA value of normal GM increased with the growing of tumor grade, peaking at 9.7% in $M_{RFL\ IV}^{C3-Fp2}$ (19% enhancement above the baseline). The second row (R2) images of Figure 5.3 further demonstrate the inner brain current distribution by a parallel diagonal cut plane as the 55° green slicing shown in the control model and the TA of normal WM gradually increased to 11.79%, reaching the maximum boost rate of 42% ($M_{RFL\ IV}^{C3-Fp2}$). At the same time, the TA of Grade I RFL brain tumor boosted 6.5 times to 82.47% and then with the growing of the tumor grade, it gradually increased to 99.56%. As a consequence, the TA values of the adjacent GM and WM to the RFL brain tumor also enhanced significantly. But the maximum boost rate of adjacent WM (343%) was much greater than that of adjacent GM (62%) because the diminished GM shunting effect contributed by the surge of the brain tumor conductivity brought comparatively more current to the inner WM tissues. Images and statistics in R4 also corroborate this assumption as the peaking current density (99th percentile) of the RFL brain tumor, adjacent GM and WM increased dramatically (peaking 266%, 28% and 48% in $M_{RFL\ IV}^{C3-Fp2}$). With the growing of tumor grade, considerable changes of the current density directions within the cortex and brain tumor could be observed apparently, especially for the regions where the RFL brain tumor meets GM, WM and CSF. The current density direction roughly went from the negatively polarized cathode to the positively polarized anode as expected.

Overall, the present of the RFL brain tumor enhanced the stimulation strength of C3-Fp2 electrode montage considerably and the developing of tumor grade also magnified such enhancement up to 19%. Though the RFL brain tumor and adjacent tissues around it received much stronger stimulation, the induced peaking current density ($0.47\ A/m^2$)

among them was still considered as safe because it was two orders below the harmful strength (142.9 A/m^2) that could cause brain lesions and far below the intensity in the cortex generated by the TTFs (Liebetanz et al., 2009, Kirson et al., 2007). Therefore, it is safe to stimulate the M1 region of patients with the RFL brain tumor under the application of C3-Fp2 electrode montage to relieve their pain caused by brain tumor. However, considering the enhanced stimulation strength, it is expected to correspondingly reduce the normal stimulation duration according to the tumor grade in the early clinical trials.

Figure 5.4 demonstrates the changing trend of median and peak current density values of the normal GM and WM in the models configured with the RFL brain tumor and proposed electrode montages. According to the median current density values of the control models with all proposed montages in Figure 5.4 (a), increasing the inter electrode distance reduced the shunting effect and allowed more current penetrating into the brain, thus resulting in a higher median current density. The presence of the RFL brain tumor did not break this rule, no matter which grade the RFL brain tumor was in. From Figure 5.4 (b), it can be concluded that the presence of the RFL brain tumor influenced the peaking stimulation strength in two different ways. Specifically for the GM, with the growing of the tumor grade, the peak stimulation strength kept declining (up to 3% loss in $M_{RFL\ IV}^{P3-C4}$) in the montages (C3-C4, P3-C4) that applied the cathode closely over the RFL brain tumor (C4). Whereas for the rest montages, the growing grade RFL brain tumor gradually increased the peak stimulation strength up to 4%. When it comes to the WM stimulation, a general slight increase of the peak stimulation current (up to 4% in $M_{RFL\ IV}^{C3-Fp2}$) could be observed with the development of the RFL brain tumor except for the montages with a larger inter electrode distance (P3-C4, P3-Fp2). This finding can be observed in the adjacent GM and WM as well in Figure 5.5. Therefore, the stimulation with cathode placed over the RFL brain tumor is expected to have compromised outcomes than expected whereas the stimulation is boosted when the RFL brain tumor is relatively far away from the cathode.

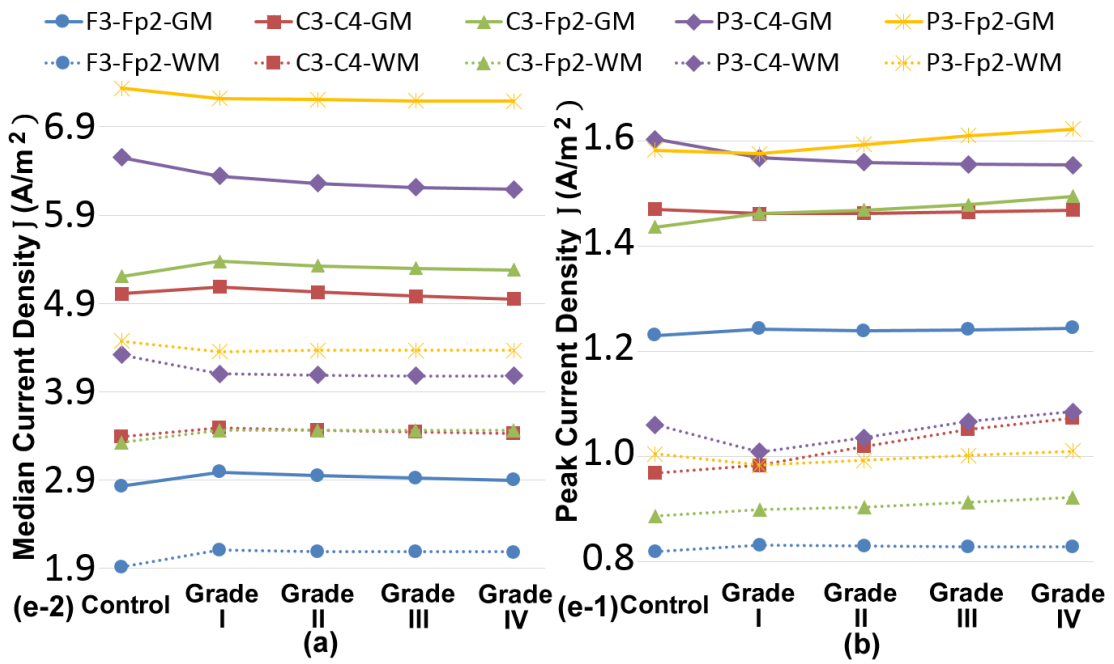


Figure 5.4 Demonstration of the median current density (a), peak current density (b) of the normal GM and WM in the models with the RFL brain tumor under all proposed electrode configurations in unit e-2 A/m² and e-1 A/m².

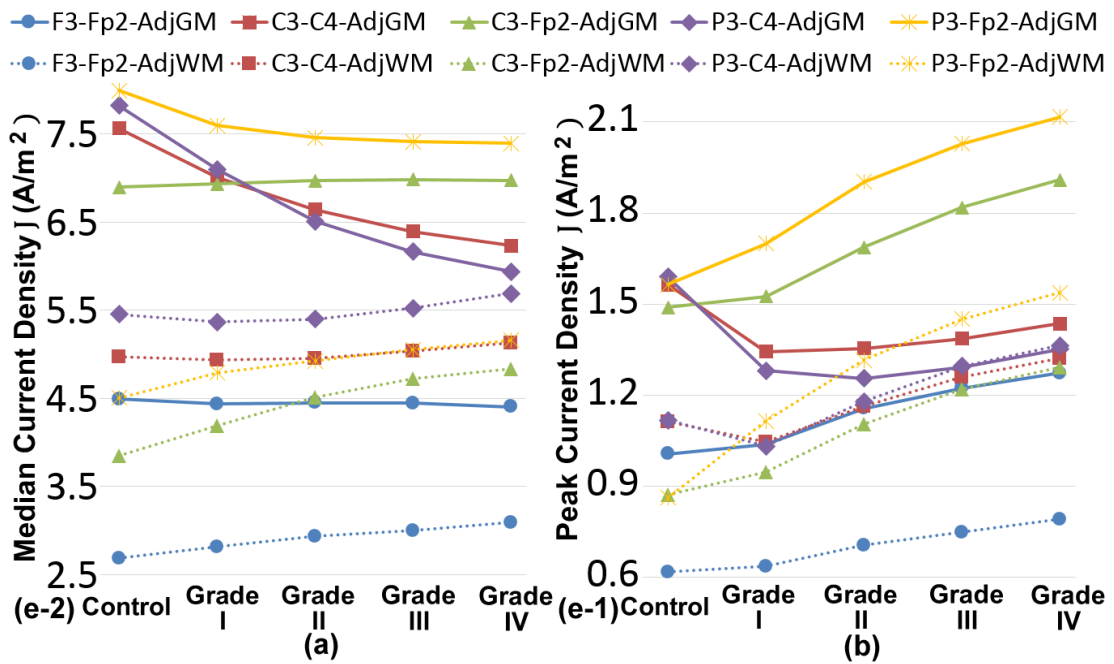


Figure 5.5 Demonstration of the median current density (a), peak current density (b) of the adjacent GM (AdjGM) and adjacent WM (AdjWM) to the RFL brain tumor in the models configured with all proposed electrode montages in unit e-2 A/m² and e-1 A/m².

Figure 5.6 depicts the peak and median current density of the RFL brain tumor in the model configured with all proposed electrode montages and tumor grades. From Figure 5.4 to Figure 5.6, it is apparent to discover that the peaking current density in

all cases was about 0.51 A/m^2 in M_{RFLIV}^{P3-Fp2} and the induced peaking current in the healthy GM and WM was 0.21 A/m^2 in the same model. As analyzed before, both values were far from the harmful current density and it should be safe to apply the proposed tDCS montages on the patients with the RFL brain tumor to relieve their neuropsychiatric conditions and acute or chronic pain caused by brain tumors.

Besides, the induced peaking current density in the high grade RFL brain tumor fitted into the effective current density strength window for intro tumor suppression (calculated as $0.35\sim 0.7 \text{ A/m}^2$) and reached up to 26% of the effective current density (1.8 A/m^2) generated by the noninvasive electrotherapy for vivo tumor suppression (Clock Jr and Lyte, 1993, Miklavčič et al., 1997). This finding provides an encouraging support to the clinical explorations on the RFL brain tumor inhibition using tDCS. However, the current density strength is still considerably lower than the working current density ($13\sim 56 \text{ A/m}^2$) calculated from other minimally invasive DCT studies using needle electrodes (Griffin et al., 1994, Sersa and Miklavcic, 1993, Oji and Ani, 2010) and the actual effects of tDCS on suppressing the RFL brain tumor still remains to be verified by clinical trials.

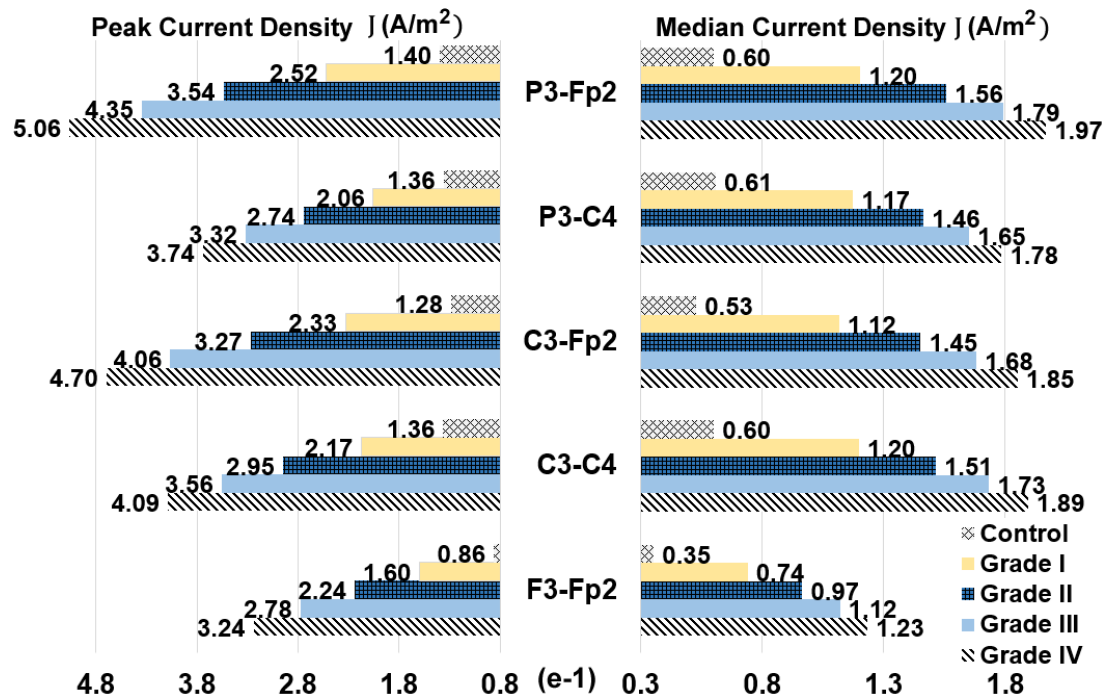


Figure 5.6 Demonstration of the peak and median current density within the RFL brain tumor in the model configured with different tumor grades and electrode montages. (Unit: $e-1 \text{ A/m}^2$)

5.3.2. Influence of the RFL Brain Tumor

As a contrast study for the RFL brain tumor, the LOL brain tumors with increasing tumor grade under the stimulation of C3-Fp2 electrode montage were constructed and their influences on the current distributions are exhibited in Figure 5.7.

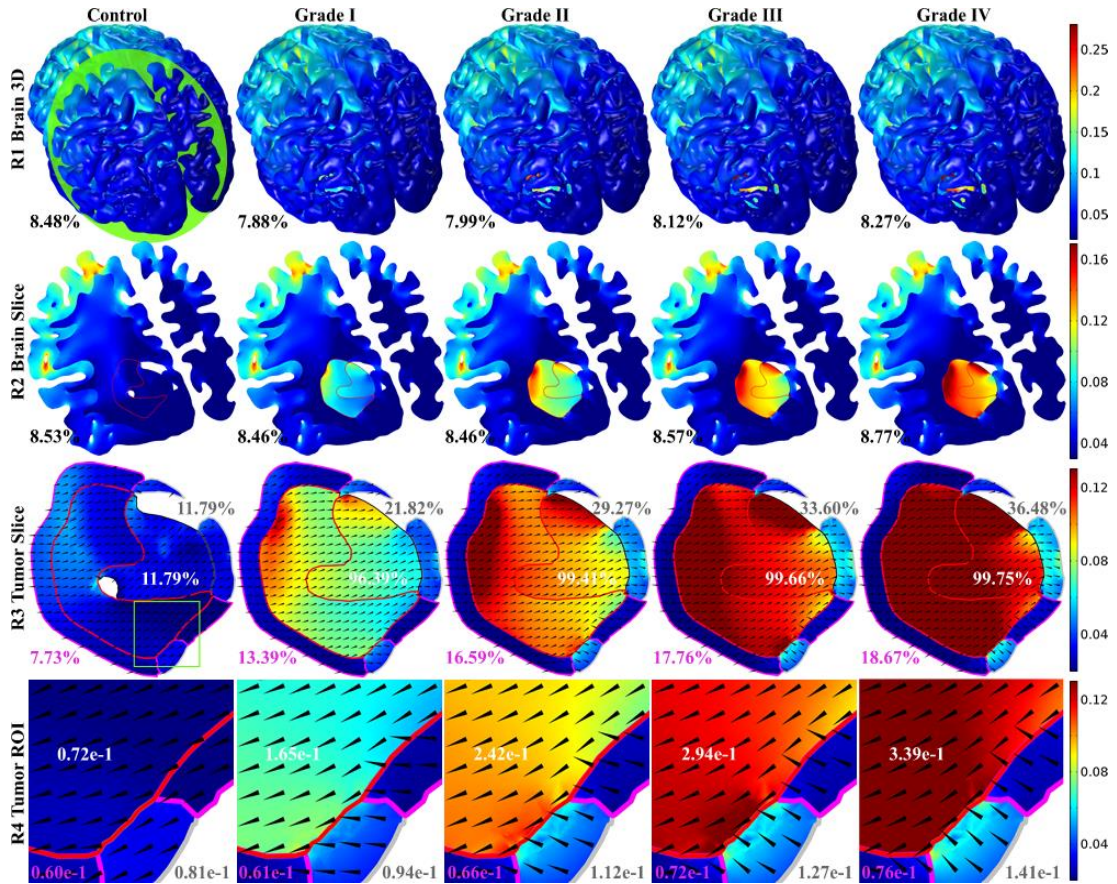


Figure 5.7 The current density J (A/m²) distribution for simulations of the LOL brain tumor in different grades under C3-Fp2 montage. (The notation follows the one used in Figure 5.3).

Under C3-Fp2 electrode montage (Figure 5.7), the TA of the normal GM demonstrated 7% decrease in the grade I tumor model ($M_{LOL I}^{C3-Fp2}$) and then gradually increased with the growing of the tumor grade. But the value was still slightly lower (2%) than the control model ($M_{LOL Control}^{C3-Fp2}$). TA values of the normal WM also showed the same trend as it slightly decreased in the low grade brain tumor models and then slowly increased in the high grade brain tumor models, peaking 3% enhancement in $M_{LOL IV}^{C3-Fp2}$. For the LOL brain tumor, adjacent GM and WM, their TA values kept increasing and reached the maximum boost rate of 746%, 209% and 142% respectively in the model with the

grade IV brain tumor ($M_{LOL IV}^{C3-Fp2}$). At the same time, their peak current density values increased up to 372%, 75% and 27%, which implied significant enhancement of the stimulation outcomes in those regions.

According to the R3 and R4 images in Figure 5.7, the current density direction still went roughly from the cathode to anode. In the LOL brain tumor, the current density directions remained almost the same with the development of the tumor grade and only some parts near CSF slightly changed. As a contrast, the current density directions within the adjacent GM and WM were substantially changed with the growing of the tumor grade, especially for the regions relatively far away from the normal inner WM. Similar to the FRL brain tumor, the most significant current density direction variation was also in the boundary tissues of the LOL brain tumor and adjacent tissues.

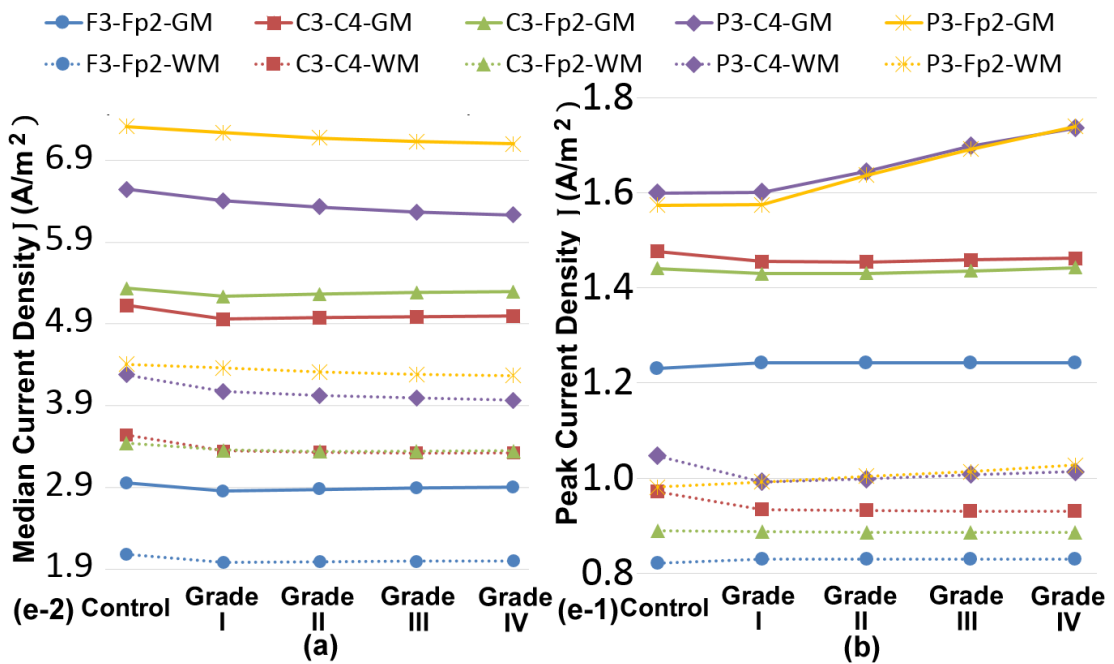


Figure 5.8 Demonstration of the median current density (a), peak current density (b) of the normal GM and WM in the models with the LOL brain tumor under all proposed electrode configurations in unit e-2 A/m² and e-1 A/m².

Overall, the present of the LOL brain tumor decreased the stimulation strength of C3-Fp2 electrode montage up to 7% and the developing of the tumor grade gradually compensated this loss and made up with this loss to 2%. The LOL brain tumor and adjacent tissues around it also received much stronger stimulation with the growing of the tumor grade, and the induced peaking current density was 0.34 A/m². Therefore, it

is also safe to apply C3-Fp2 electrode montage on the patients with the LOL brain tumor to relieve their cancer pain. However, considering the reduced stimulation strength, it is expected to correspondingly increase the normal stimulation duration according to the tumor grade in early clinical trials.

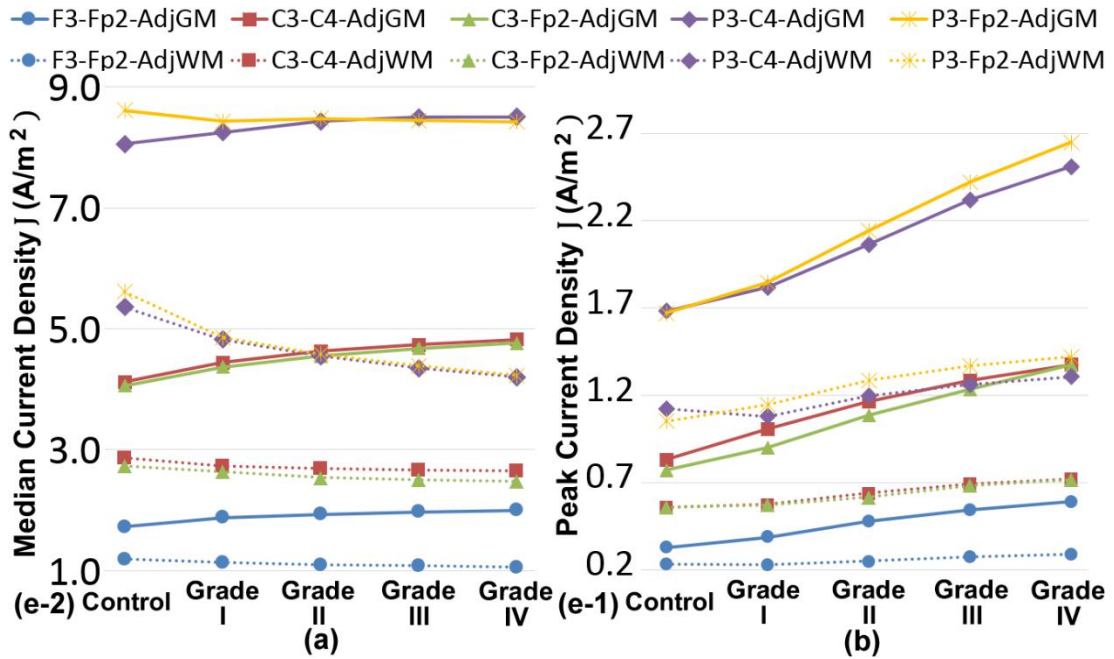


Figure 5.9 Demonstration of the median current density (a), peak current density (b) of the adjacent GM (AdjGM) and adjacent WM (AdjWM) to the LOL brain tumor in the models configured with all proposed electrode montages in unit e-2 A/m² and e-1 A/m².

According to Figure 5.4 and Figure 5.8, the influences of the LOL brain tumor on the median and peak current density distributions in the cortex were similar to the influences of RFL brain tumor. The most apparent difference between them happened in the peak current distributions of GM with P3-C4 montage. Specifically, the peak current density in the model with the LOL brain tumor gradually increased up to 9% above the control model with the development of the tumor grade whereas it kept a moderate declining speed, reaching at most 3% loss for the peak stimulation strength in the model with RFL brain tumor. Besides, the maximum boost rate for the peak current density of GM in the LOL brain tumor model with P3-Fp2 configuration was 11% whereas it was 3% in the RFL brain tumor model with the same montage. Therefore, the present of the LOL brain tumor enhanced the stimulation outcomes when the anode is placed over the tumor. Even considering such enhancement, the

induced maximum peak current density (0.17 A/m^2) in all models with the LOL brain tumor is still in the normal region and no safety concerns could be involved.

Figure 5.9 reveals the influence of the LOL brain tumor on the local current distributions. The peak current density values of the adjacent GM and WM under all proposed montages increased with the growing of the LOL brain tumor grade, which implied stronger local peak stimulation strength (up to 75%). But for the montages that applied anode over the LOL brain tumor, the overall stimulation strength in the adjacent WM declined up to 25% with the growing of the tumor grade.

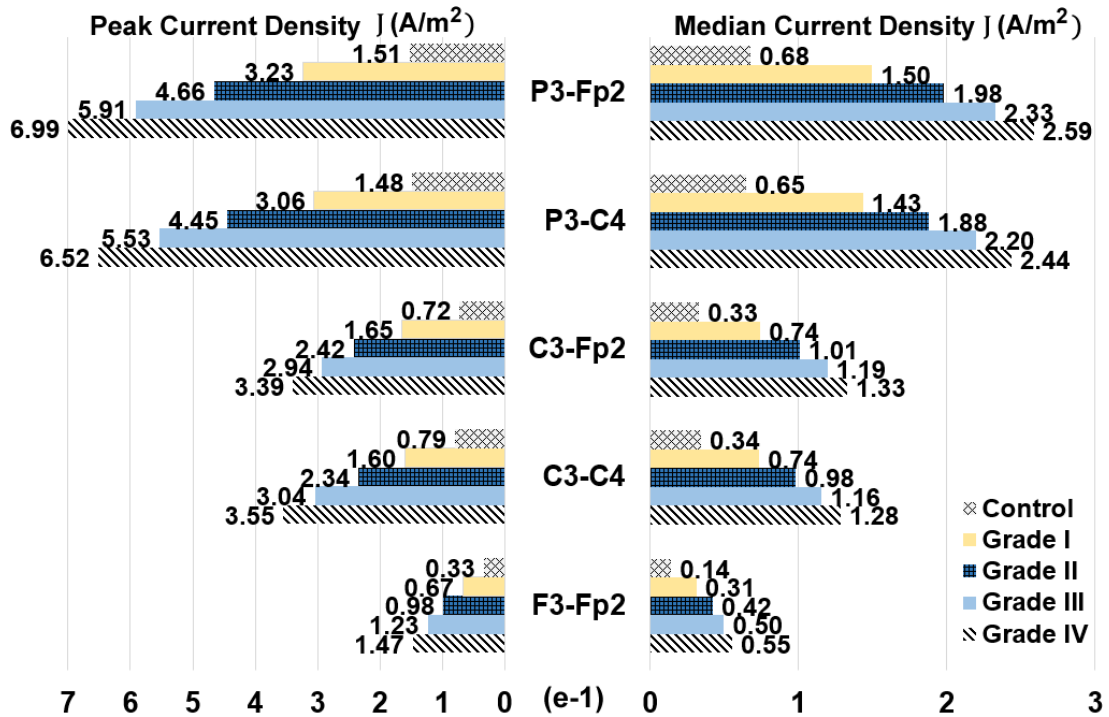


Figure 5.10 Demonstration of the peak and median current density values within the LOL brain tumor in the model configured with different tumor grades and electrode montages. (Unit: e-1 A/m²)

Figure 5.10 depicts the peak and median current density values of the LOL brain tumor in the model configured with all proposed electrode montages and tumor grades. It is obvious that the peaking current density in all cases was about 0.70 A/m^2 in $M_{LOL,IV}^{P3-Fp2}$ and the induced peaking current in the healthy GM and WM was 0.27 A/m^2 in $M_{LOL,IV}^{P3-Fp2}$ as well. Both values should be safe to apply the proposed tDCS montages on the patients with the LOL brain tumor to relieve their neuropsychiatric conditions and acute or chronic pain caused by brain tumors. Moreover, for the LOL brain tumor targeted montages (P3-C4, P3-Fp2), increasing the inter electrode distance can result stronger

stimulation within the tumor, which meets the strength for *in vitro* tumor suppression and reaches up to 39% of the effective current density induced by the noninvasive electrotherapy for *in vivo* tumor suppression.

5.4. Discussion

5.4.1. Variations of the Electrode Montage and Tumor Location

Electrode location is one of the most significant stimulation parameters during tDCS because varied electrode montages generate diverse current distribution patterns within the brain globally. Tumor location generally determines the induced complications depending on the affected region of the brain. In this study, five tDCS montages (F3-Fp2, C3-C4, C3-Fp2, P3-C4 and P3-Fp2) for the conventional tDCS are applied. The experiment results showed that their influences on the current distributions within the brain tumors and adjacent tissues are dramatically different. As reported by previous studies on the electrode montages, increasing the inter electrode distance generally results in more current penetrating through the scalp and skull at a cost of compromising the peak current strength of focality (Faria et al., 2011, Bai et al., 2012, Bai et al., 2014, Datta et al., 2008b). But the present of a brain tumor makes the influences of electrode montages more complex as the present of a brain tumor stimulates the local shunting effect and causes more current passing into the inner brain, thus resulting global influences on the current distributions.

The current density direction induced by tDCS roughly goes from the negatively polarized cathode to the positively polarized anode. No apparent influence on the global stimulation can be induced when the brain tumor is harbored off the main current path within the brain. But when it is close to or right in the path, obvious influence on the global stimulation within the brain can be expected. Specifically, when the cathode electrode is placed above the superficial RFL brain tumor, the global stimulation strength on the GM is likely to decrease (Figure 5.4) whereas it increases significantly when the anode electrode is applied above the buried LOL brain tumor (Figure 5.8). This observation is in line with the differences reported between anode stimulation and cathode stimulation.

For the local influence caused by the variations of the montages and tumor locations, the above trend can be observed more apparently, especially for the montages that applies their electrodes above the brain tumors (C3-C4, P3-C4 in Figure 5.5 and P3-C4, P3-Fp2 in Figure 5.9). But, their stimulation outcomes on the WM shows opposite effects.

5.4.2. Tumors in Different Grades

In this study, the electrical conductivity of brain tumors is scaled according to their grade. It is found that, the electrical property changes of the brain tumors also result in global current distribution variations in the models with different grade tumors, especially for the montages that applied the electrodes near the brain tumors. Specifically, when the cathode is applied above the superficial RFL brain tumor (C3-C4, P3-C4), the increase of the tumor grade magnifies the global diminished stimulation effects. For the montages that applied anode to the buried LOL brain tumor (P3-C4, P3-Fp2), the increase of the tumor grade advances the strengthen stimulation outcomes.

In addition, based on the observations from Figure 5.6 and Figure 5.10, the current distributions within the brain tumor in different grades are dramatically different and with the increase of tumor grade, the peak and median current density values also boost accordingly. Still, the boost influence of tumor grade on the induced current density is strengthened when the tumor exists in or is close to the primary current stream between the cathode and anode.

5.4.3. Current Limitations and Future Improvements

In this study, only a brain tumor mask (case6) from SPL and NSG Brain Tumor Database was selected because of its instinctive consistency with the interest of this study and comparatively higher image quality. Based on this patient-specific tumor mask, the brain tumor locations and grades were investigated to obtain their influences in shaping the current distributions during tDCS.

Due to the scope definition of this study, only two tumor locations were chosen without fully accommodating the variations of tumor location or the tumor size among all the 10 cases from the brain tumor database. Therefore, the findings in this study may not be exactly the same as it derived from other cases, especially when the brain tumor mask from other cases were modelled with different locations and sizes. Such limitation points out that further explorations are required in order to extend current work by including more brain tumor cases from the database and carry out continued investigation of the influence of the brain tumor size on the current distribution patterns during tDCS.

5.5. Conclusion

This study is the first initial to investigate the influence of brain tumors on current density distributions with a numerical method, and to explore the potential treatment using a series of high resolution realistic human head models with build-in brain tumors. A systematic analysis was conducted to investigate the influence of brain tumor's grades (I-IV) and locations (RFL and LOL) on the current distributions under five conventional electrode montages (F3-Fp2, C3-C4, C3-Fp2, P3-C4 and P3-Fp2) during tDCS.

The results showed that significant changes of the global current distributions are resulted when a brain tumor is close to the electrodes whereas such influence is inconspicuous when the brain tumor is harbored away from the primary current stream between the cathode and anode. In addition, the tumor grade also considerably influenced the current density distributions. Overall, it is safe to apply tDCS on the patients with brain tumors to modulate their neuropsychiatric conditions or control the acute and chronic pain caused by brain tumors.

6. CURRENT DISTRIBUTIONS IN LOW GRADE BRAIN TUMOR

This chapter is a further research of brain tumor influence on current distribution and focuses on the current distributions within the low grade brain tumor and adjacent edematous brain tissues, and aim to investigate the role of peritumoral edematous brain tissues during tDCS.

6.1. Introduction

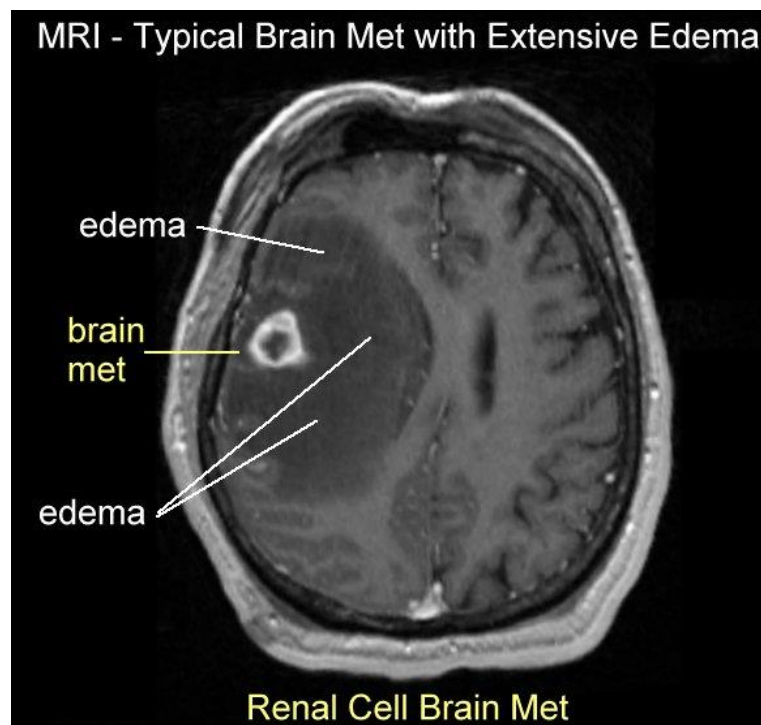


Figure 6.1 Demonstration of brain tumor (renal cell brain metastasis) and extensive surrounding edema from post-contrast T1 weighted MRI scan (www.aboutcancer.com, 2016)

As introduced previously, WHO endorsed the most widely used I–IV grading system based on the tumor cell location and type to classify tumors with increasing aggressive degree (Bauer et al., 2013, Kleihues et al., 1993). Grade I and grade II tumors are relatively slow in growing and they are not that aggressive compared with the Grade III and grade IV tumor. Therefore, grade I and grade II tumors are normally classified as low grade tumors. Low grade brain tumors (grade I and grade II) have relatively

slow growing cells and have no or only slightly abnormal morphology features under a microscopic view (Society, 2016).

Symptoms of patients with brain tumor are normally determined by the tumor size and functional regions that was intruded by the brain tumor. According to an audit servery of patients with cerebral glioma type brain tumors, the most common symptom caused by brain tumor was headache (46.5%), which was followed by seizure (26.5%). In addition, diverse mental disorders (confusion, personality problem and etc.) were also declared at hospital presentation (Grant, 2004). Those symptoms were also reported by many other researches (RUSHTON and ROOKE, 1962, Schaller and Rüegg, 2003, Meyers et al., 1998, Malamud, 1967, Forsyth and Posner, 1993, Kaal and Vecht, 2004).

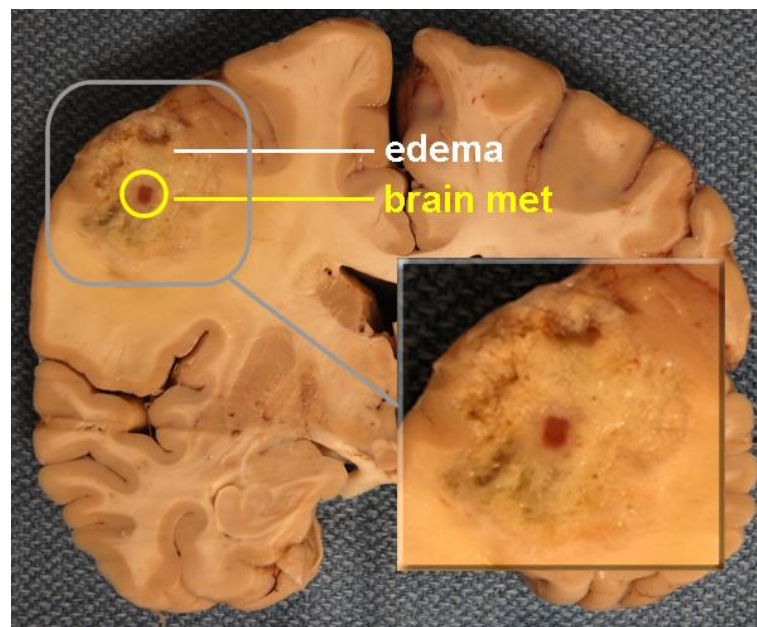


Figure 6.2 Demonstration of brain tumor (metastatic lung carcinoma) and extensive peritumoral brain edema from human brain coronal slice with enlarge view of the region of interest. This image is modified from (Agamanolis, 2016).

Despite the differing histological features and categories of brain tumors, peritumoral brain edema (swelling around the brain tumor) is one of the most common complications of brain tumor. It is reported that Peritumoral brain edema contributes to the neurologic dysfunctions and debilitated life quality (Kaal and Vecht, 2004, Papadopoulos et al., 2004). With the advent of CT and MRI, brain edema can be identified from brain scans. As shown in Figure 6.1 and Figure 6.2, extensive peritumoral brain edema can be observed around the brain tumor. The foundational

reason behind is that both headache and other clinical mental disorders associate with brain tumor are caused by the elevated intracranial pressure (ICP), which could be significantly increased by the presence of peritumoral brain edema (Reithmeier et al., 2005, IKEDA and MATSUMOTO, 1999, Fishman, 1975, Tosoni et al., 2004). Peritumoral brain edema is the result of plasma leakage into the parenchyma through dysfunctional cerebral capillaries (Kaal and Vecht, 2004, Jha, 2003).

Both in vivo and in vitro studies have confirmed that tumors exhibit much higher electrical conductivity (up to 7.5-fold) and electrical permittivity (up to 5-fold) than the normal surrounding tissue because of the increased cellular water and salt content, altered membrane permeability, changed packing density, and orientation of cells. In addition, higher grade tumors are also reported to have higher electrical conductivity (Gabriel et al., 1996a, Fricke and Morse, 1926, Halter et al., 2011, Scholz and Anderson, 2000, Zou and Guo, 2003, Van Lier et al., 2011, Smith et al., 1986).

The computational experiments in this chapter consisted of a series of high resolution human head models with the same brain tumors locations and electrode montages as that in chapter 4. Specifically, the anatomically accurate human head model and brain tumor were constructed from MRI datasets (T1, T2 and PD-MRI). Five electrode configurations (F3-Fp2, C3-C4, P3-C4 and P3-Fp2) were applied to the models individually and the sponge electrodes were all squared ones with $5\text{ cm} \times 5\text{ cm}$ dimension as well.

For each montage, there was a control model constructed with low grade brain tumor. The control models contained eighteen different human head tissues derived from MRI scans and the low grade brain tumor was derived from another separated MRI dataset of a real patient with brain tumor, which was then manually merged into the control models and configured with different locations within the brain. When it comes to the proposed model with peritumoral brain edema, the edematous tissue surrounding the brain tumor further segmentation was conducted into edematous white matter (EWM) and edematous grey matter (EGM).

6.2. Model Design and Implementation

Firstly, a series of high resolution realistic human head models integrated with an MRI-based brain tumor were constructed as the control models for each montage and tumor location. After that, proposed models were constructed based on the control models by supplementing peritumoral edematous tissues segmentation. Then these paired models were meshed into finite element models and the simulation was carried out after the boundary conditions and tissue properties were assigned accordingly.

6.2.1. Image Processing and Model Construction

In this study, the control model was derived from the previous studies in our research group (Shahid et al., 2012, Shahid et al., 2013b). The utilized MRI human head datasets were obtained from the Simulated Brain Database of BrainWeb, which provided an MRI simulator to generate a set of MRI data volumes by varying imaging parameters and artifacts (Cocosco et al., 1997, McConnell Brain Imaging Centre, 2014). For the brain tumor dataset, it was obtained from the Surgical Planning Laboratory (SPL) and the Department of Neurosurgery (NSG) Brain Tumor Database (Kaus et al., 2001, Warfield et al., 2000). Each human head dataset volume has 1 mm^3 isotropic voxel resolution and contains $181 \times 181 \times 217$ slices in the transverse, sagittal and coronal axes. T1-weighted MRI volume was applied for the tissue identification and segmentation of GM, WM, fat, muscles (temporalis and extraocular muscles), eyes (vitreous body and lens) and scalp. In addition, T2-weighted and Proton Density (PD) MRI volumes were also used for the segmentation of cerebrospinal fluid (CSF) and inner skull boundaries. FMRIB's Software Library (FSL) platform (Smith et al., 2004) was deployed to derive tissue masks of scalp, skull, CSF, WM, GM and nine subcortical structures (hindbrain, hippocampus etc.) whereas module ScanIP from commercial software package Simpleware 4.3 was applied for the semiautomatic generation of fat, muscles and eyes. The brain tumor mask was obtained from a patient (case 6) in SPL and NSG Brain tumor Database that was diagnosed with low grade glioma in the right frontal brain. The volume of this tumor is $3.28 \times 10^4 \text{ mm}^3$ and its surface area covers $1.49 \times 10^4 \text{ mm}^2$. After the healthy model was constructed in Simpleware, the mask of a brain tumor derived from the MRI dataset was imported in different regions of interest (ROI) to construct the control models of this study. Specifically, these locations are also superficial RFL and buried LOL regions.

After the models were constructed and parameters were configured, semiautomatic operations were performed in the +CAD and ScanIP modules within Simpleware to get the adjacent grey matter and adjacent white matter around the tumor. After manual correction operations in ScanIP, for the superficial RFL brain tumor, the peritumoral EWM occupies $10.7 \times 10^3 \text{ mm}^3$ volume and covers $9.37 \times 10^3 \text{ mm}^2$ surface area while the peritumoral EGM occupies $9.05 \times 10^3 \text{ mm}^3$ volume and covers $11.5 \times 10^3 \text{ mm}^2$ surface area. When it comes to buried LOL brain tumor, the peritumoral EWM occupies $11.0 \times 10^3 \text{ mm}^3$ volume and covers $10.9 \times 10^3 \text{ mm}^2$ surface area while the peritumoral EGM occupies $12.9 \times 10^3 \text{ mm}^3$ volume and covers $14.9 \times 10^3 \text{ mm}^2$ surface area. Then, the models were meshed using +FE Free meshing algorithm in Simpleware and the compound coarseness was set to -15 whereas the region of tumor was further refined by setting the mesh size to 0.8 mm. The derived volumetric finite element models contain 8 million tetrahedral elements and each simulation consumed approximately one hour for an 8-core workstation.

The electrode configurations and tumor locations applied in this chapter were consistent with the previous study, this study constructed five primary groups of human head models configured with different electrode montages (F3-Fp2, C3-C4, C3-Fp2, P3-C4 and P3-Fp2) and tumor locations (RFL, LOL).

6.2.2. Boundary Conditions and Electrical Properties

Considering that this study still falls in the low frequency range under 10 kHz, Quasi-static approximation could be made as well and the boundary conditions were assigned the same with chapter 4. For each simulation, 0.8 A/m^2 inward current density (equivalent to 2 mA) was applied to the exposed anode surface using Numann boundary condition.

In this study, nineteen normal tissue and sponge electrodes were assigned with the same conductivity values in chapter 5 and their conductivities can be referred in Table 5.1. The electrical conductivity of the cancerized low grade brain tumor components and around edematous tissues coupled with their calculation reasoning are shown in Table 6.1 (Meng et al., 2013).

Input parameters including electrode montages (F3-Fp2, C3-C4, C3-Fp2, P3-C4 and P3-Fp2), tumor locations (RFL, LOL) and tumor grades (I-IV) were separately investigated in groups to explore their influences on the current distributions within the cortex and brain tumors during tDCS.

| Tissue | Conductivity (S/m) | Comment |
|---------------|---------------------------|------------------------|
| CWM | 0.3 | 2 times of WM and GM |
| CGM | 0.64 | |
| EWM | 0.225 | 1.5 times of WM and GM |
| EGM | 0.48 | |

Table 6.1 Conductivity of the Cancerized Brain Tumor Components and Adjacent Edematous Tissues.

6.3. Computational Results

The simulations and results of low grade brain tumor and peritumoral edematous brain tissues (EGM, EWM) are interpreted using the concept of threshold area (TA), which was also previously introduced in chapter 5. The TA is defined as the volume fraction of a tissue (or region) that has 70% or higher current density than the 99th percentile of the maximum current density (referred as peak current density to avoid calculation errors) within the tissue or region, which is deemed as an indicator to reflect the stimulation outcome (Parazzini et al., 2011).

| | F3-Fp2 | | C3-C4 | | C3-Fp2 | | P3-C4 | | P3-Fp2 | |
|------------|---------------|------------|--------------|------------|---------------|------------|--------------|------------|---------------|------------|
| | RFL | LOL | RFL | LOL | RFL | LOL | RFL | LOL | RFL | LOL |
| CGM | -12% | -16% | -5% | -25% | -10% | -20% | -3% | -35% | -15% | -45% |
| CWM | 8% | -7% | 2% | -3% | 9% | -11% | 0% | -10% | 8% | -10% |
| EGM | 184% | 213% | 239% | 235% | 228% | 254% | 309% | 181% | 222% | 244% |
| EWM | 191% | 247% | 113% | 160% | 179% | 371% | 138% | 195% | 218% | 225% |

Table 6.2 Boost rates of TA in the proposed models compared to their control model without edema.

In this section, the influence of possible edema on the local current distributions was investigated in another series of models. Specifically, the control models were configured with the low grade RFL brain tumor and LOL brain tumor under five electrode montages used in the above studies. For the proposed models, the edema around the brain tumor was further modelled to include more details. To better demonstrate the current density variations within the cancerized brain tumors (CGM, CWM) and adjacent edematous tissues (EGM, EWM) of the proposed models, their

TA changing rates are used in Table 6.2 and the current distributions within the brain are demonstrated in Figure 6.3 by the same slicing planes demonstrated in chapter 5.

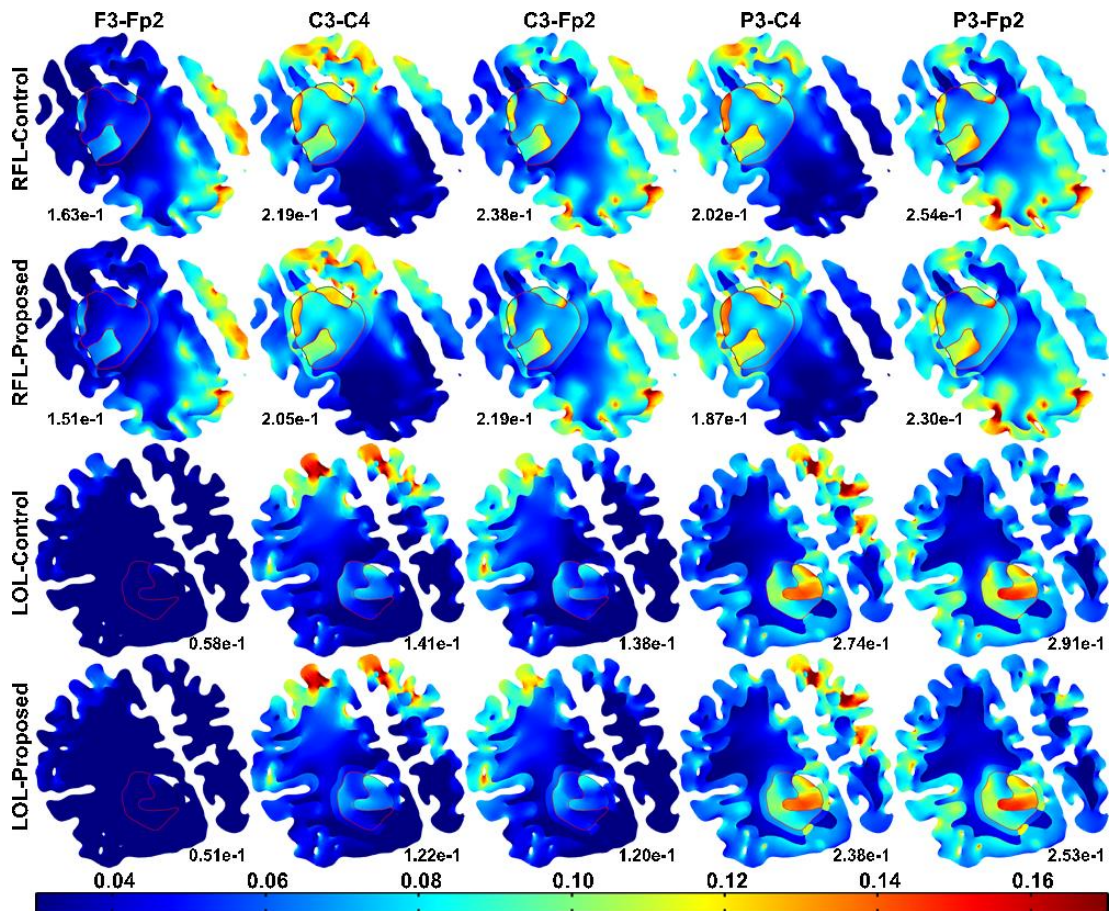


Figure 6.3 Demonstration of current density J (A/m^2) within the brain tumor tissues and surrounding edematous tissues under all the proposed electrode configurations in the control and proposed models. The number below each slice is the maximum peak current density among the tumor and adjacent tissues (they are unanimously from CGM due to its high conductivity).

In Figure 6.3, compared with the control models, the present of edema did not bring conspicuous changes to the global current distributions, but the local current density distributions were affected considerably. Edema induced more shunting effect and caused the stimulation of CGM declining (up to -45%) for all montages, which could also be reflected by the peak current density shrink as shown in Figure 6.3. At the same time, the stimulation of CWM in RFL was slightly enhanced (8% in maximum) whereas the stimulation of CWM in LOL kept declining (up to 11%). Due to the conductivity increase of edema tissues, TA values of both EGM and EWM in the proposed models were enhanced significantly though their boost rates were very diverse (1~3 times).

6.4. Discussion

The outcomes of chapter 5 and 6 cleared the safety concerns for applying tDCS on the patients with brain tumors because the induced current strength within the brain and tumor is far below the level which could cause lesions and mortality (Griffin et al., 1994, Liebetanz et al., 2009). Compared with other electric therapies (TTFs and DCT), the induced current density strength is also much smaller than theirs. Therefore, even with the consideration of edema, it is still safe to manipulate tDCS on the patients with brain tumors to modulate their neuropsychiatric conditions or control the acute and chronic pain caused by brain tumors. But the stimulation duration is suggested to be adjusted accordingly in the early clinical trials. When it comes to suppressing a brain tumor, the actual effects of tDCS need to be verified by clinical trials because the tDCS induced current density in the brain tumors is considerably weak, compared with the majority of the effective electric treatments.

Switching on and off the tDCS stimulation was reported to bring a few cases of visual sensation due to the retinal and visual cortex stimulation. For the montages applied cathode on Fp2, the peak current density within the right eye shows up to 1% increase compared with the control model. Considerable increase of the peak current density in the visual cortex is also resulted due to the present of LOL brain tumor, especially when P3 location is used in the montages. These enhancements may increase the possibility of suffering visual sensation. Still this possible side effect can be reduced by the prolonged fade in and fade out manipulations of the current (Poreisz et al., 2007).

In this study, we assigned a low grade brain tumor to two different locations in the brain (superficial RFL and buried LOL) without taking the tumor size parameter into modelling. Considering the tumor size and growing, the stimulation for the brain with a higher grade brain tumor is expected to result in more shunting effect, stronger stimulations and suppression on neuropsychiatric conditions and brain tumors, respectively. Individualized stimulations coupled with varied electrode configurations are the next targets to be explored in the further studies.

6.5. Conclusion

In this study, a systematic analysis was conducted to investigate the influence of peritumoral edematous tissues coupled with tumor locations (RFL and LOL) on the current distributions under five conventional electrode montages (F3-Fp2, C3-C4, C3-Fp2, P3-C4 and P3-Fp2) during tDCS.

The results showed that under the same montage, the present of edema brought comparatively bigger influence on the buried LOL brain tumor than the superficial RFL brain tumor by weakening its stimulation strength considerably. However, the stimulation on the edematous tissues were significantly boosted for all the proposed montages. These discoveries should be noticed when the tDCS clinical trials are designed for the patients with brain tumors. Overall, even with the consideration of peritumoral brain tissues, it is still safe to apply tDCS on the patients with brain tumors to modulate their neuropsychiatric conditions or control the acute and chronic pain caused by brain tumors.

7. BRAIN BLOOD VESSEL MODELLING AND INFLUENCE ON CURRENT DISTRIBUTIONS

This chapter focuses on including brain blood vessels in the model and further investigate their influence on current distribution during tDCS. In this chapter, a high resolution realistic human head model with 26 tissues types were firstly constructed as the control model. As a contrast, both the extracranial and intracranial blood vessels were carefully segmented and supplemented in constructing the proposed model. After that, about five common electrode montages with varied inter-electrode distance were individually configured to composite five major study groups, each group containing a control and a corresponding proposed model. Then, the tDCS simulations were carried out based on finite element methods and the data was collected for analysis.

7.1. Introduction

The development of advanced brain models were advanced by accommodating increasingly more anatomical features and accuracy electrical properties derived from multimodal medical imaging approaches. Specifically, the computational model used MRI datasets were obtained from the prior 1.5T scanners to the recent widely used 3T scanners till the most current 7T scanners, providing dramatically improved contrast and spatial resolution as well as the elevated possibility to extract more accurate anatomical details. In addition, the application of DTI and Magnetic resonance electrical impedance tomography (MREIT) scans from the same subject also sheds light on the progressive conductivity estimation and measurement (Shahid et al., 2013b, Kwon et al., 2016, Sadleir et al., 2010, Kim et al., 2014b).

Currently, MRI-derived high resolution realistic computational models utilising finite element methods are normally applied as a standard solution to better understand and predict the injected current distribution patterns within the cortex and targeted brain regions of interest. It also makes the customized tDCS therapy possible by optimizing the stimulation parameters to avoid unexpected outcomes, especially for the patients with particular physical conditions, like brain lesions, skull defect and etc. (Parazzini

et al., 2016, Datta et al., 2011, Song et al., 2016a, Datta et al., 2010, Truong et al., 2013, Hesse et al., 2007)

7.2. Brain Blood Vessels and Modelling

During the development of computational human head modelling, increasingly detailed computational models were proposed with enhanced model complexity and accuracy in pursuance of more accurate simulation outcomes of their studies (Wagner et al., 2006, Wagner et al., 2013, Bai et al., 2014, de Oliveira et al., 2016, Shahid et al., 2013b, Fiederer et al., 2016, Datta et al., 2011). Among those studies, the work from Fiederer and his collaborators concluded the importance of blood vessels in the high resolution human head modelling for EEG source analyses and envisioned the possible benefits for brain stimulation modellings (Fiederer et al., 2016). However, with the advancement of medical imaging techniques, the blood or blood vessels system within the human head was rarely considered, nor included in the most recent high resolution realistic human head modellings for various reasons (Wagner et al., 2013, Bai et al., 2014, Song et al., 2016a, Laakso et al., 2016, Shahid et al., 2015, de Oliveira et al., 2016, Parazzini et al., 2016).

Apart from the research interest reasons, the overlooking of extracranial and intracranial blood vessels in human head modelling might be explained by resource limitations, like unsatisfying scanner resolution, shortage of blood imaging equipment and reconstruction approach. By all means, omitting the compartment like blood vessels is still considered as a noticeable deficiency in constructing the high resolution realistic human head models for tDCS simulations, especially when blood vessels system spans almost all the regions of human head and blood vessels were reported to have a considerably higher electrical conductivity than the majority of other body tissues (Sadleir et al., 2010, Datta et al., 2011, Tang et al., 2016, Fiederer et al., 2016). Therefore, it could be fatal for the precision requested research and clinical studies to neglect the blood vessels system in their simulation models, especially when the importance of blood vessels on the current distribution patterns of tDCS is still unclear. In other words, the exact influence of accommodating blood vessels on the realistic human head modelling for tDCS is still open for explorations.

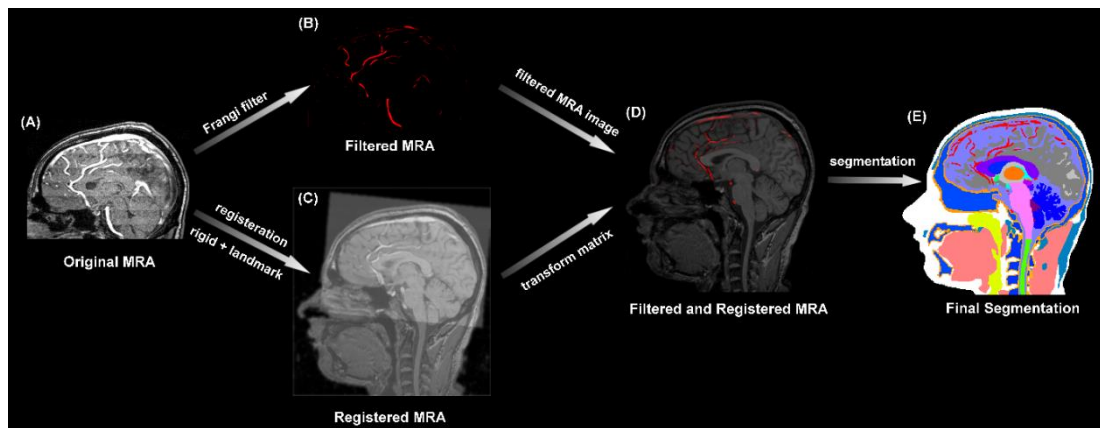


Figure 7.1 The image processing work flow for blood vessels segmentation. (A): The original MRA image. (B): The filtered MRA image generated by Frangi filter (present with default boundary range values). (C): The original MRA was registered to T1-MRI using both rigid and landmark registration approaches. (D): The filtered MRA image was registered to T1-MRI using the transform matrix obtained from operations in (C). (E): The final segmentation result of blood vessels (further tuning was applied to the filtered and registered MRA image).

Addressing this question is expected to have meaningful value in setting the baseline of high resolution realistic human head modellings for both research studies and clinical trials. Specifically, if blood vessels system is proven to demonstrate considerable influence in defining the current distributions within the brain during tDCS, corresponding concerns and efforts should be made to accommodate the blood vessels mask in the simulation models for the precision requested studies, particularly for the case needs optimized stimulation solutions. Otherwise, if no meaningful clinical benefits could be obtained from it, considerable equipment resources and post processing workloads will be saved in the future tDCS modellings.

7.2.1. Image Registration and Segmentation

The high resolution realistic human head models in this study were constructed from multimodal MRI scans of the same subject. The data were obtained from the International Consortium for Brain Mapping (ICBM) database and the chosen subject was named as MNI_0663 from Montreal Neurological Institute of ICBM (Mazziotta et al., 2001). The datasets used in the modelling were T1, T2 weighted MRI scans and Magnetic Resonance Angiography (MRA) scans of MNI_0663 while the original T1-MRI had the best spatial resolution ($0.54 \text{ mm} \times 0.54 \text{ mm} \times 1.0 \text{ mm}$), which was later resampled with 1.0 mm^3 voxel resolution by default during image processing, thus

resulting a $256 \text{ mm} \times 256 \text{ mm} \times 176 \text{ mm}$ dimension for the model. MRA is an imaging technique based on MRI to generate images of blood vessels and the original spatial resolution of MRA dataset in this study is $0.625 \text{ mm} \times 0.625 \text{ mm} \times 0.6 \text{ mm}$.

The image registration and segmentation operations were carried out in semiautomatic manners with the help of a couple of software packages and algorithms. Firstly, T2-MRI was registered to T1-MRI using the rigid registration option in an open source software named 3D Slicer and then both T1 and registered T2 MRI datasets were performed the skull stripping operation and automatic segmentation of scalp, skull, CSF, WM and GM using FSL platform (Fedorov et al., 2012, Jenkinson et al., 2012).

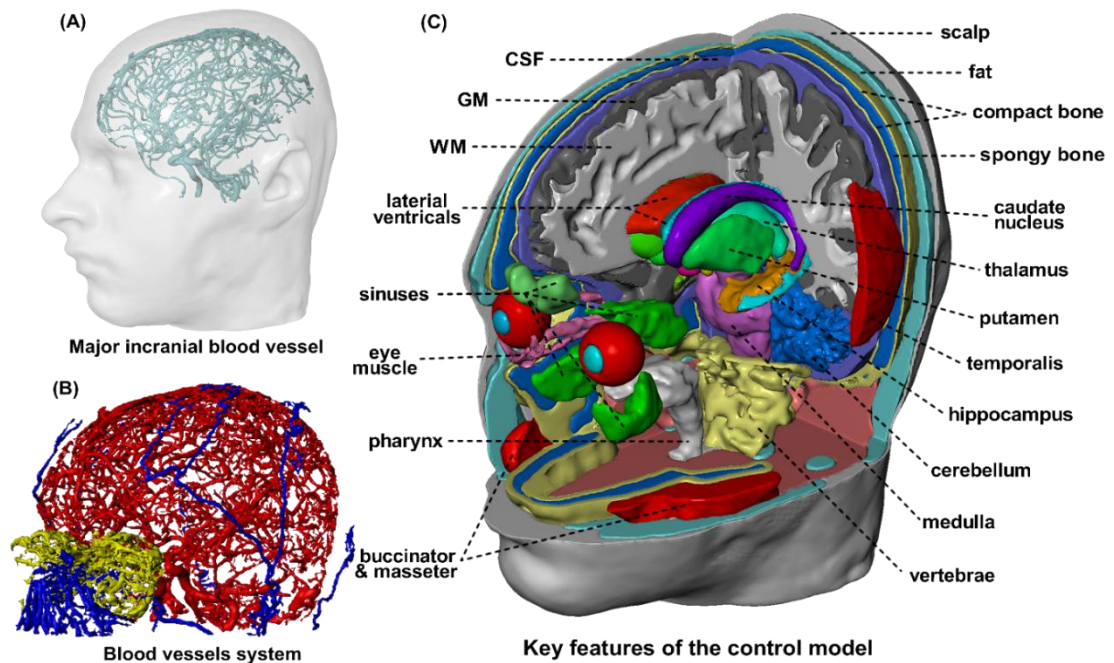


Figure 7.2 The demonstration of key features from the constructed models in this study. (A): The preliminary segmentation result of major intracranial blood vessel obtained without tuning operations. (B): The final segmentation outcome of blood vessels system within the proposed human head models (red mask: intracranial blood vessel obtained after tuning, yellow mask: blood vessels in the eye organ; blue mask: other extracranial blood vessel in the scalp).

Another set of head tissues masks were also generated using BrainSuite package, which were used as auxiliary masks to perform semiautomatic corrections during the final segmentations (Shattuck and Leahy, 2002). In the meanwhile, a full list of gyri labels of MNI_0663 were obtained against the BCI-DNI brain atlas using BrainSuite and some labels were then used in 3D Slicer to generate the mask of target gyri in this

study (Pantazis et al., 2010). The gyri of interest in this study were selected according to the target stimulation regions of corresponding montages.

The working flow for blood vessel segmentation is shown in Figure 7.1. Specifically, to extract a better quality mask of blood vessels from MRA, Hessian based Frangi vesselness filter was firstly applied to outstand blood vessels from the original MRA image background. At the same time, the original MRA image was registered to T1-MRI using both rigid and landmark registration approaches in 3D slicer to achieve impeccable registration outcome, which consequently generated a transformation matrix in this step. Then the filtered MRA images were manually registered to T1-MRI in 3D Slicer using exactly the same transformation matrix obtained precedently (Kroon, 11 June 2009). After that, all the masks and background images were imported into ScanIP module of Simpleware to perform further segmentation and manual corrections against the human head atlas before the configurations of proposed electrode montages (Mai et al., 2016). During this procedure, the processed image of blood vessels (filtered and registered MRA) was sufficient to generate the major blood vessel branches within the human head (as shown in Figure 7.2 (A)). After further tuning the boundary range values of the filtered and registered MRA volume, the minor branches of blood vessels were segmented as well (as shown in Figure 7.2 (B)) and those minor branches were initially hard to notice in Figure 7.1 (B) and Figure 7.1 (C). As a result, the control model for each montage contained 26 masks excluding the gyri while the proposed models had additional four masks for the intracranial blood vessel and extracranial blood vessels.

After the manual corrections and montage assignments, five control models with different electrode configurations and their corresponding models with blood vessels were meshed using +FE Free meshing algorithm in Simpleware and the compound coarseness was set to -30. The final volumetric finite element models in the control group contain about 10 million finite elements while the number is approximately 13 million for the proposed models. The computation was carried out in a commercial software package named COMSOL Multiphysics and each simulation took about half an hour for a computing workstation with dual Intel Xeon E5-2697 V3 CPUs.

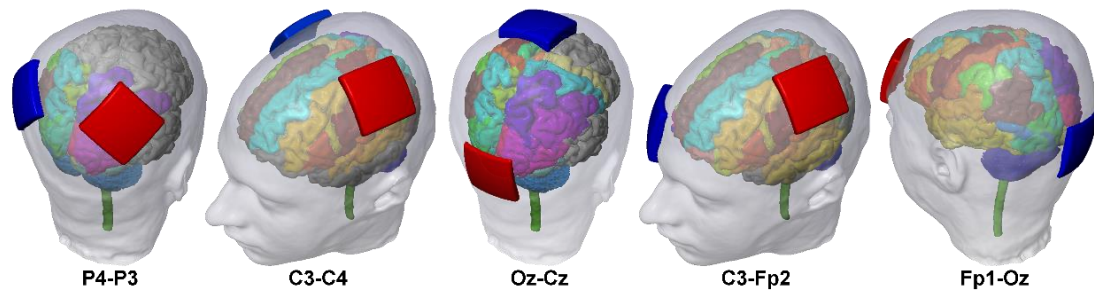


Figure 7.3 The demonstration of tDCS montages selected in this study.

7.2.2. Montage Modelling and Electrical Property Assignment

In this study, the electrode configurations complied with the International 10-20 EEG recording system and both the cathode and anode were modelled as 5 cm × 5 cm sponge pads, which were traditionally soaked in saline solution in conventional tDCS applications to smoothly conduct electrical current. As shown in Figure 7.3, five common tDCS montages were selected into modelling and they were chosen based on the increasing inter electrode distance and varied target stimulation regions. Specifically, the five electrode configurations are P4-P3, C3-C4, Oz-Cz, C3-Fp2 and Fp1-Oz while their corresponding inter electrode distance are 97 mm, 121 mm, 133 mm, 141 mm and 193 mm, respectively. As shown in P4 (right parietal lobe) – P3 (left parietal lobe) is used to stimulate the parietal lobe regions in the numerical competence studies (Kadosh et al., 2010). C3 (left M1-motor cortex area) – C4 (right M1-motor cortex area) is applied to stimulate the contralateral orbital motor cortex in the treatment of stroke (Hesse et al., 2007). Oz (occipital cortex) – Cz (vertex) is applied to stimulate the primary visual cortex in the visual processing tasks (Antal et al., 2004a). C3 (left M1-motor cortex area) - Fp2 (right contralateral supra-orbital region) is used to stimulate the primary motor cortex and contralateral supraorbital regions in the studies of cancer pain control (Silva et al., 2007). Fp1 (left supraorbital region) – Oz (inion) is referred to stimulate the left supraorbital in the treatment of depression (Bai et al., 2014).

The selected tissue masks from Figure 7.2 were shown in Table 7.1, and total twenty-nine tissue types were included in this work. Their conductivities were derived from a series of recognized reports and those values were widely used by a wide range studies

with solid referencing records (Baumann et al., 1997a, Datta et al., 2009, Gabriel et al., 1996a, Gabriel et al., 1996b, Geddes and Baker, 1967, Gonçalves et al., 2003, Nicholson, 1965, Oostendorp et al., 2000b, Shahid et al., 2014a).

| Material | Conductivity (S/m) | Reference |
|--|-------------------------------|----------------------------|
| Saline soaked electrodes | 1.4 | (Datta et al., 2009) |
| Scalp | 0.43 | (Shahid et al., 2014a) |
| Fat | 0.025 | |
| Muscles (head, neck and eyes) | 0.16 | (Gabriel et al., 1996a) |
| Eyes | 0.5 | |
| Eye lens | 0.31 | (Gabriel et al., 1996b) |
| Skull | 0.015 | (Oostendorp et al., 2000a) |
| CSF (including four ventricles) | 1.79 | (Baumann et al., 1997b) |
| GM | 0.32 | (Gonçalves et al., 2003) |
| WM | 0.15 | (Nicholson, 1965) |
| Hindbrain (cerebellum, colliculus, medulla, spinal cord, mammillary body and cerebral aqueduct) | 0.25 | (Geddes and Baker, 1967) |
| Globus pallidus | | |
| Nucleus Accumbens | | |
| Amygdala | | |
| Fornix Crura | 0.32 | (Gonçalves et al., 2003) |
| Hippocampus | | |
| Thalamus | | |
| Putamen | | |

Table 7.1 Conductivity values for the electrodes and tissues.

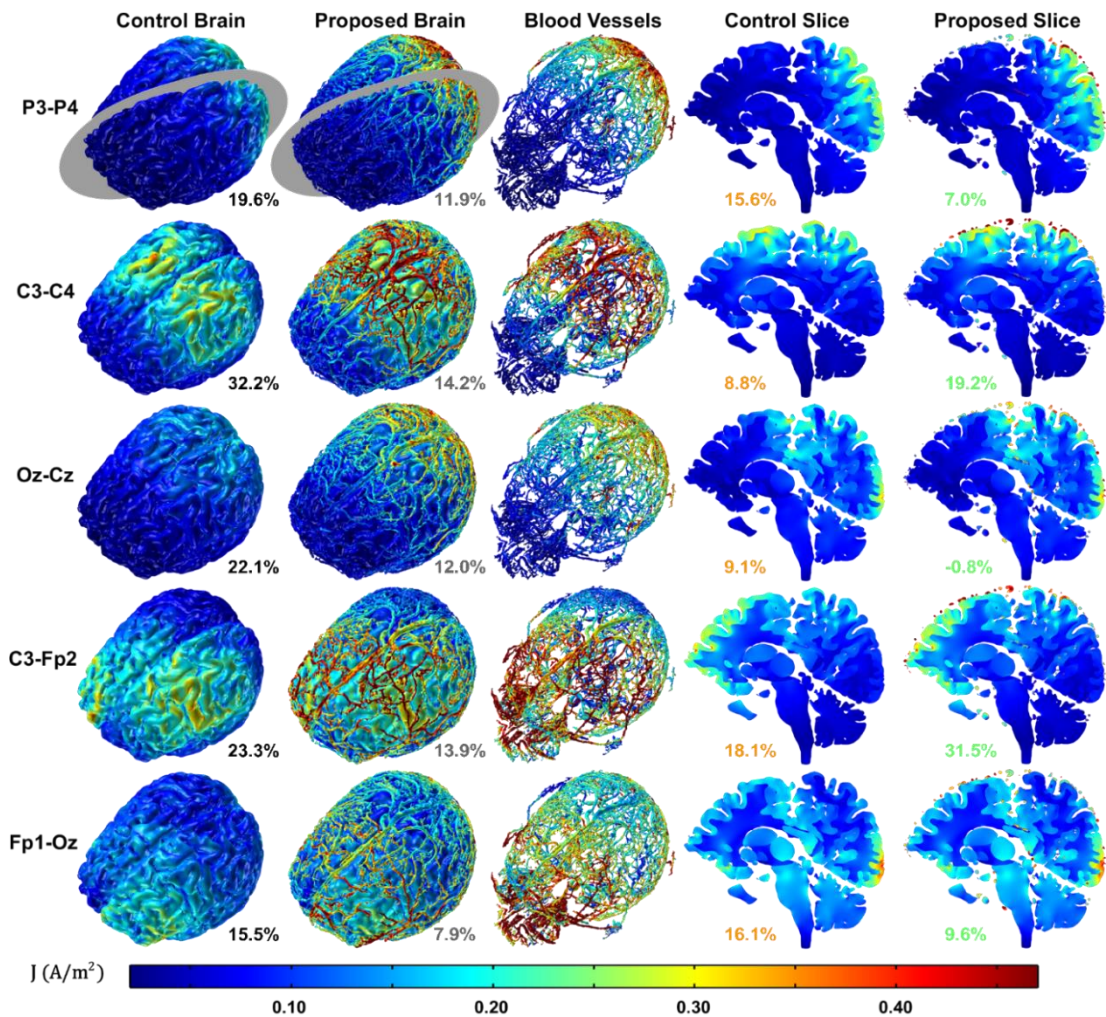


Figure 7.4 The illustration of current density distributions under all the proposed electrode montages. The first two columns are the demonstrations for the current density distribution patterns within the brain of the control and proposed models while the third column particularly presents the blood vessels system from the proposed model. The fourth and fifth columns are the sliced brain of the control and posed models, which are shown as grey plants in the first two columns. The numbers in the first two columns are the TA changing rates of GM (black color) and WM (grey color) while the numbers in the last two columns are the TA changing rates of the inner brain (yellow color) and hindbrain (green color) structures, respectively.

The current used in tDCS studies was normally set between 0.5 mA ~ 2 mA and the ceiling value (2 mA) was applied for all simulations in this study. To define the boundary conditions of anode and cathode, both Neumann and Dirichlet boundary conditions are generally used in such definition. In this study, Neumann boundary condition was selected to apply the inward current density J_n (0.8 A/m², equivalent to 2 mA) to the exposed anode surface while Dirichlet boundary was referred to define electrical potential V (ground potential) on the cathode surface. Considering that scalp is generally treated as electric insulating from air, ground potential was applied to the

air-scalp boundary whereas continual current density was configured to all tissue-tissue boundaries within the human head.

7.3. Global Influence of Blood Vessels System on the Cerebral Current Distributions

The computational experiments were designed and carried out based on four major regions of interest, namely, GM, WM, inner brain and hindbrain. The results were also analysed according each of the four regions.

The normalised current density (A/m^2) within the specific region of interest was chosen to demonstrate the result difference between the control model and the proposed model. Three key features of the current density distribution, median current density, peak current density and threshold area (TA) were utilized in this study. The peak current density was slightly different from the absolute maximum current density as it was defined as the 99th percentile of the maximum current density to avoid calculation errors. The TA was the volume fraction of a tissue (or region of interest) that has 70% or higher current density than the peak current density of that tissue or region, which was referred as an efficient reflection of the stimulation outcomes (Parazzini et al., 2011). To better demonstrate the influence brought by the blood vessels in the proposed model, the changing rate of TA, peak and median current density within each paired group (control model and proposed model with the same montage) were also obtained by dividing the value of proposed model with that of the control model.

Different electrode montages are expected to induce varied current distribution patterns within the cortex and there is no exception for this study. As shown in the control models of Figure 7.4 (first column), the generated current distributions of the brain had close relationship with the designed electrode montage and the regions having the most notable current density also roughly complied with the target regions of corresponding montage. In 3D view (second column), no apparent visual difference of the current distribution patterns could be recognized by observing the brain plots of the paired models for each montage, though the intracranial blood vessels were

introduced. Similarly, it is also difficult to visually confirm the influence of blood vessels in defining the current distribution within the cortex by comparing the sliced brain plants (last two columns of Figure 7.4). However, from the outcome plots of the proposed brain and blood vessels system (second and third columns of Figure 7.4), it is relatively easy to notice that the present of blood vessels system enables the current to reach comparatively further regions through the blood vessel highway, thus resulting the current spreading more areas of the brain surface than the control models.

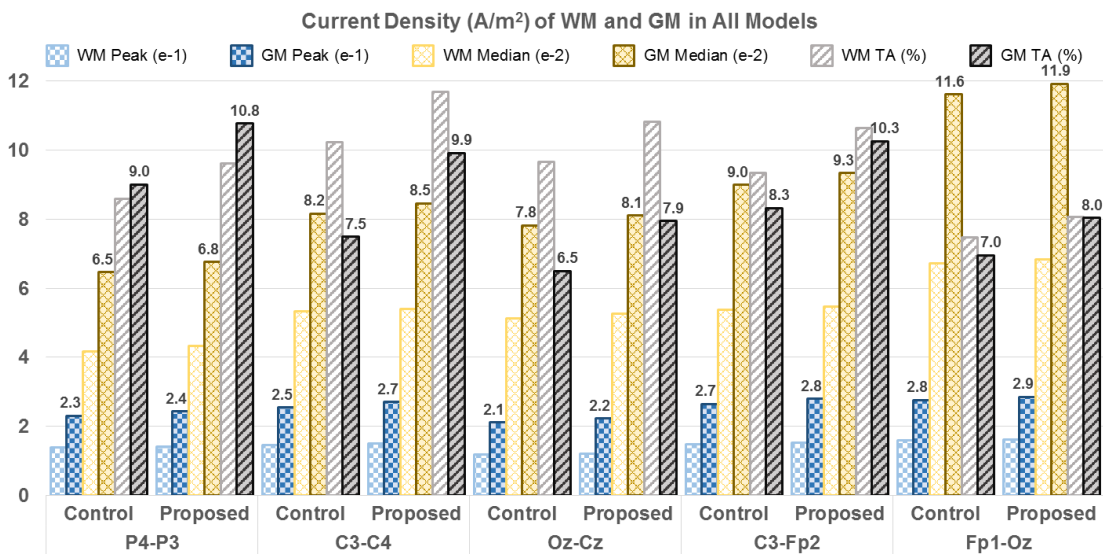


Figure 7.5 The peak, median and TA values of the current density within WM and GM in all models.

Additionally, the percentages in the first two and the last two columns of Figure 7.4 are representing the TA changing rate of GM, WM, inner brain and hindbrain structures, respectively. From those TA boosting rates, it is obvious to conclude that blood vessels system plays a significant role in defining the current distributions within the cortex. Specifically, the simulation results showed that after introducing the blood vessels system to the control models, the TA of GM and WM were enhanced up to 32.2% and 14.2%, both of which were achieved in the model with C3-C4 montage. Furthermore, the stimulation outcome of GM is expected to show the doubled influence than that of WM with the present of the brain blood vessels system.

As a contrast, the TA value for the inner brain and hindbrain were improved up to 16.1% and 31.5% in the model configured with C3-Fp2 montage. Particularly, there was an exception for the TA changing rate of hindbrain with Oz-Cz electrode

configuration as the proposed blood vessels system almost showed no influence (-0.8%). This special situation could be explained by the lack of intracranial blood vessels in the target cerebral regions (hindbrain) of the anode electrode. As a result, no highway was available for the current to efficiently transfer the current from the focal area beneath the anode electrode to the hindbrain regions, thus the induced current in the proposed model spreading to the hindbrain almost in the same way as it did in the control model. The slight decrease could be caused by the minor blood vessel present in the hindbrain, which occupied a tiny portion of hindbrain and caused the statistical issue.

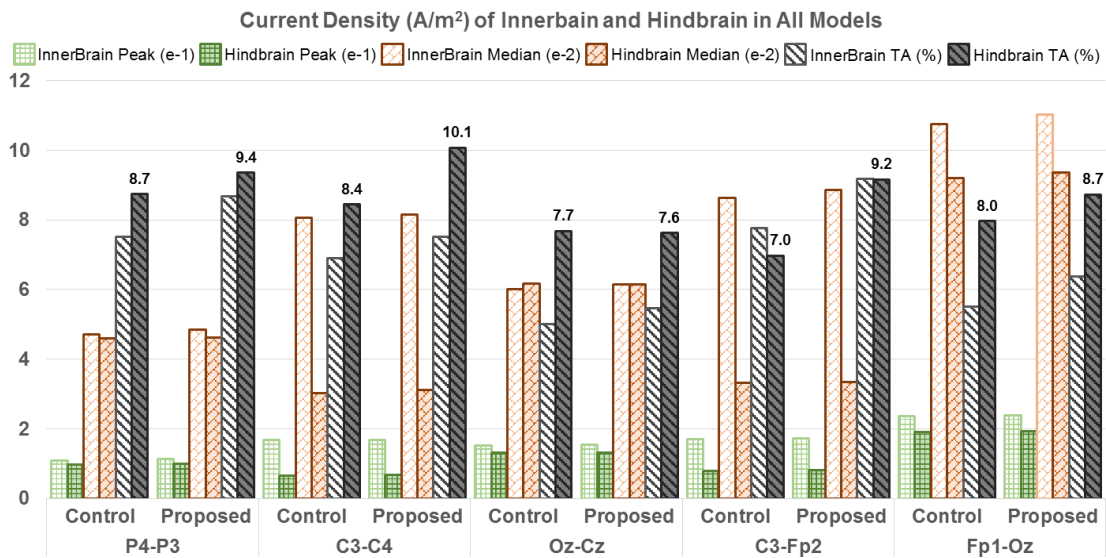


Figure 7.6 The peak, median and TA values of the current density within the inner brain and hindbrain in all models.

More detailed information on the peak, median and TA values of the current density within the four major brain structures are given in Figure 7.5 (GM and WM) and Figure 7.6 (inner brain and hindbrain). According to Figure 7.5, the present of blood vessels system enhanced the peak, median and TA of current density for both GM and WM under all montages. Specifically, the key feature values (peak, TA and median) of GM increased up to 6.1%, 32.2% (under C3-C4) and 4.4% (under P4-P3), correspondingly while the values of WM increased up to 3.3%, 14.2% (under C3-C4) and 3.3% (under P4-P3) respectively. As demonstrated in Figure 7.6, the peak, median current density and TA of the inner brain compartment escalated up to 2.6%, 2.9% (under P4-P3) and

18.1% (under C3-Fp2) while the peak, TA and median feature values of Hindbrain increased up to 3.8%, 31.5% (under C3-Fp2) and 2.8% (under C3-C4).

The result showed that, with the present of blood vessels system, global influence of the current distributions in the brain could be caused by enhancing the stimulation outcomes up to 32.2% for GM, 13.9% for WM, 18.1% for inner brain organizations and 31.5% for hindbrain. In other words, the actual global stimulation outcomes are relatively stronger than the simulation based expectations in our current applications of conventional tDCS.

7.4. Gyri Specific Influence of Blood Vessels System on the Current Distributions during tDCS

The cerebral current distribution with gyri precision was also obtained and investigated in accordance with the target regions of the proposed five electrode montages. In this section, the TA (%) of eight major cerebral lobe regions was analysed in the first place and then the target regions of each electrode configuration with gyri details were presented individually.

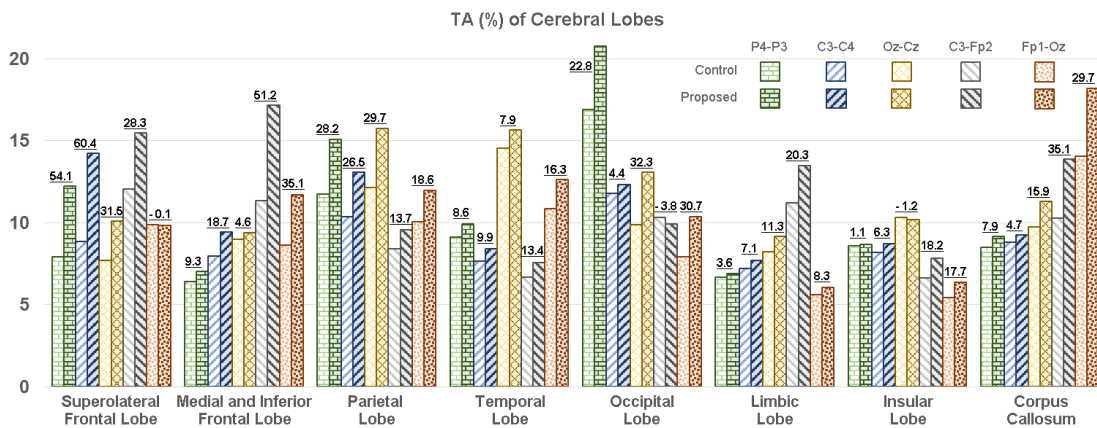


Figure 7.7. The TA (%) of cerebral lobes for all montages with contrast of the control and proposed groups. The underlined numbers over the paired columns are the boosting rate of TA for each lobe region under the proposed electrode configuration when the blood vessels system was considered.

As shown in Figure 7.7, with the modelling of blood vessels system, apparent enhancement could be observed for the TA of the majority of lobe regions, especially for the target lobes of all proposed electrode montages, which indicated that enhanced

stimulations of the corresponding regions could be expected than the original assumptions. To be specific, the TA values of parietal and occipital lobes under P4-P3 montage increased 28.2% and 22.8% compared with their control group while the TA values of superolateral frontal and parietal lobes under C3-C4 montage boosted 60.4% and 26.5% respectively in their proposed group. Under Oz-Cz electrode configuration, the TA values of occipital and parietal lobes escalated 32.3% and 29.7% respectively after the accommodation of blood vessels system. With the modelling of blood vessels system, the TA values of superolateral frontal lobe, medial and inferior frontal lobe and corpus callosum under the C3-Fp2 electrode configuration increased 28.3%, 51.2% and 35.1% respectively while the TA values of occipital lobe, medial and inferior frontal lobe and corpus callosum boosted 30.7%, 35.1% and 29.7% correspondingly under the Fp1-Oz electrode montage. In particular, the limbic and insular lobes were found with relatively higher induced current density under the electrode montages with greater inter-electrode distance (C3-Fp2 and Fp1-Oz) and their TA values under both electrode montages escalated 20.3%, 18.2%, and 8.3%, 17.7% respectively.

| Electrode Montage | Selected Target Gyrus | Peak Current Density (e-1 A/m ²) | | TA (%) | | |
|-------------------|-------------------------------|---|----------|---------|----------|---------------|
| | | Control | Proposed | Control | Proposed | Increase Rate |
| P4-P3 | Superior Parietal Gyrus | 2.9 | 3.1 | 14.3 | 20.1 | 40.1 |
| | Angular Gyrus | 2.8 | 3.1 | 15.8 | 23.3 | 47.2 |
| | Middle Occipital Gyrus | 2.7 | 2.9 | 18.3 | 24.7 | 34.9 |
| | Cuneus | 2.4 | 2.7 | 16.3 | 20.7 | 26.8 |
| C3-C4 | Superior Frontal Gyrus | 2.9 | 3.1 | 9.6 | 16.3 | 70.4 |
| | Middle Frontal Gyrus | 2.9 | 3.3 | 10.2 | 16.4 | 60.6 |
| | Post Central Gyrus | 3.0 | 3.1 | 11.1 | 15.1 | 35.2 |
| | Superior Parietal Gyrus | 2.4 | 2.4 | 13.5 | 18.3 | 35.8 |
| Oz-Cz | Superior Occipital Gyrus | 3.2 | 3.4 | 16.6 | 22.9 | 37.7 |
| | Cuneus | 2.6 | 2.7 | 11.4 | 15.4 | 35.2 |
| | Superior Parietal Gyrus | 2.2 | 2.4 | 14.0 | 19.7 | 40.8 |
| | Supramarginal Gyrus | 1.6 | 1.7 | 16.8 | 22.0 | 31.3 |
| C3-Fp2 | Superior Frontal Gyrus | 3.1 | 3.2 | 12.2 | 16.4 | 34.5 |
| | Inferior Frontal Gyrus | 2.9 | 3.2 | 12.4 | 16.0 | 28.8 |
| | Subcallosal Gyrus | 2.2 | 2.4 | 13.6 | 26.2 | 92.2 |
| | Middle Orbitofrontal Gyrus | 2.3 | 2.7 | 17.0 | 30.3 | 77.8 |
| Fp1-Oz | Superior Occipital Gyrus | 3.9 | 4.0 | 11.7 | 16.6 | 41.5 |
| | Cuneus | 3.0 | 3.1 | 10.0 | 13.7 | 37.6 |
| | Gyrus Rectus | 2.5 | 2.9 | 11.4 | 22.1 | 94.5 |
| | Posterior Orbitofrontal Gyrus | 3.0 | 3.3 | 10.2 | 16.7 | 64.7 |

Table 7.2 The peak and TA values of the most influenced target brain gyri under all proposed tDCS montages after the modelling of blood vessels system.

Table 7.2 gives the current distribution summary of the target gyri that were influenced the most by the accommodation of blood vessels system under all proposed tDCS montages. Compared with the tDCS stimulation outcomes of the control models, a general increase trend could be observed for almost all brain gyri in the proposed models with blood vessels system except for a few small inner brain regions due to the segment classification and statistical reasons. In particular, owing to the presence of blood vessels system, the stimulation for the target gyri of all proposed montage were enhanced significantly by increasing the peak current density and TA up to 18.9% (in middle orbitofrontal gyrus under C3-Fp2) and 92.2% (in subcallosal gyrus under C3-Fp2), respectively. For the gyri off the target regions, no apparent alteration of the current distribution was found.

7.5. Discussion

7.5.1. The Value and Cost of Brain Model Complexity

This study followed the recent trend of improving the model complexity during the forward human head modelling in order to pursue the relatively higher simulation accuracy by introducing the masks of blood vessels system. But, another crucial problem about increasing model complexity needs to be considered and discussed before assigning the non-negotiable value of blood vessels in tDCS orientated simulations. As pointed out by Bikson and his colleagues, increasing the model complexity does not necessarily guarantee the model accuracy or bring meaningfully guide for clinical utility unless the model details (complexity) and accuracy (mask segmentation and tissue properties assignment) are rationally balanced (Bikson et al., 2012a, Bikson et al., 2012b, Bikson et al., 2015). However, according to some of the early and recent studies, blood vessels was confirmed to have considerably higher electrical conductivity than the majority of other human tissues and show great impact on the EEG signal sourcing. Considering that body liquid, like CSF, was believed as a super highway for electricity distributions during tDCS, blood vessels system is expected to have similar role in defining the current distributions. Therefore, such findings and hypothesis imply the necessity of increasing the model complexity by accommodating blood vessels system if solid work and reliable reference can be

included in the mask generations and electrical properties assignment during the modelling. Most importantly, this hypothesis is proved to be positive according to the simulation results of this study.

In this study, blood vessels system is reported to have significant influence in defining the current distribution patterns during tDCS, which should confirm its value in the tDCS modellings. Still, to avoid the possible misleading result as warned by Bikson and his colleagues, 20% extra workload is expected to obtain the accurate masks of the blood vessel systems, which is considered as a challenging and time consuming part (Shahid et al., 2014b, Bikson et al., 2012b). For simulation models that are constructed based on the existing phantoms, it could be much easier to include blood vessels in their studies. But for those models constructed from image stacks, considerable resources and extra workload are expected.

7.5.2. Limitations and Future Directions

It has been well reported that anatomical features are expected to shape a complex spatial current distribution in the brain during tDCS, especially for the localizations of stimulations. As a result of anatomical variations between the subjects caused by the gender and age, the induced current distribution patterns of the same electrode montage between different patients could be different though the induced current strength in the brain were generally found in the same order (Datta et al., 2012, Kim et al., 2014a, Bai et al., 2014). As a pioneer study focusing on the role of blood vessels system in the precise tDCS studies, this work did not inspect the influence of inter-subject differences on the role of blood vessels system. From the perspective of the electrical conductivity, the blood vessels system was believed to act as an express way to conduct the current more efficiently during tDCS. Therefore, the modelling of blood vessels system in other realistic human head models is still believed to enhance the stimulation strength of tDCS though subject variations may slightly affect the stimulation enhancement rates reported in this study. Nonetheless, further studies are also expected to extend this study with more electrode montages and finite element models in order to quantitatively analyze the role of blood vessels system in conventional tDCS modelling.

7.6. Conclusion

Human brain blood vessels reconstruction is a challenging but rewarding research area and it is also believed to be significant in the forward human head modelling though considerable extra workload is required to accommodate this anatomy feature. This chapter, to the best of our knowledge, is supposed to be a pioneer work to systematically include the brain blood vessels to investigate the role of blood vessels system in the realistic human head modelling for tDCS. We constructed a series of MRI-based high resolution human head model with 26 tissue types and the tDCS stimulation was conducted under five electrode montages with varied targeting regions. The observation was analyzed based on the calculation of induced median current density, peak current density and effective threshold area. The results showed that up to 32% and 92% enhancement of tDCS stimulation outcomes could be detected in the global GM and target gyri after the accommodation of human head blood vessels system, which confirmed the important role of blood vessels system in the realistic human head modelling for tDCS though 20% extra workload was introduced during the model construction. Therefore, this study will set a new baseline of the model complexity for the future precision requested tDCS modelling studies.

8. CONCLUSIONS AND FUTURE DIRECTIONS

This project was developed to address the precise applications of tDCS in conditional scenarios utilizing high resolution realistic human head models using FEM. In particular, the influence of head orientations was pre-validated using real shaped human head model. Moreover, the application of tDCS on the patients with brain tumors was systematically investigated. The role of blood vessels in shaping the current distributions within the cortex during tDCS was well studied.

8.1. Major Contributions

1. The influence of brain shift caused by the gravity on the current distributions during tDCS was pre-validated and recognized based on real shaped human head models.
 - a. The importance of head orientation during tDCS was pointed out and pre-validated for precise application of tDCS.
 - b. The necessities of brain shift corrections for precise tDCS modelling were recognised and evaluated for the first time.
2. The precise applications of tDCS on the patients with brain tumors are investigated for the first time in tDCS modelling studies.
 - a. The safety concern on applying tDCS to the patients with brain tumor was cleared to modulate their neuropsychiatric conditions or control the acute and chronic pain caused by brain tumors.
 - b. The influence of brain tumor location and brain tumor grade on the induced current distribution patterns within the cortex during tDCS was evaluated, and the current distributions within the cancerized brain tissues and surrounding edematous tissues were also studied.
 - c. The role of brain tumors in shaping the current distribution patterns within the cortex during tDCS was identified and addressed.
3. The role of blood vessels in defining the current distributions within the brain during tDCS was quantitatively investigated for the first time.
 - a. The necessity of blood vessels to be included in the realistic head model and the influence of blood vessels in shaping the current distributions during tDCS were thoroughly studies and recognized.

- b. The value and cost by introducing blood vessels was addressed from model complexity aspect.
 - c. A new baseline for the model complexity requirement for precise tDCS studies and customized applications could be set by accommodating blood vessels in the model.
4. A new framework for constructing MRI and MRA image based multimodal high resolution realistic human head models with gyri precision was established.
 - a. The mask of blood vessels was obtained with accuracy and systematically presented in the tDCS modellings for this project.
 - b. A subject specific model had been constructed with 29 major compartments and 12 types of tissues. As for the gyri precision one, it can include 66 extra regions of interest for gyri.
 - c. This approach is repeatable for other stimulation studies that require precise prediction and validation, such as the precise modelling for TMS and DBS, which can save considerable time during the model construction.

8.2. Limitations and Future Directions

This dissertation improved the precise applications of tDCS in three areas: the influence of brain shift in shaping the current distributions, applications of tDCS on the patients with brain tumors and the role of blood vessels in shaping the current distributions of tDCS. Specifically, in this project, the head orientation influence on the precise application of tDCS was studied and pre-validated using a series of real shaped human head models. For precise application of tDCS on the patients with brain tumors, the influence on the current distributions within the cortex is investigated. Finally, this project followed the trend of increasing the head model complexity by introducing the blood vessels into high resolution realistic human head models.

However, there are more work to be done to further improve this research in the future.

Firstly, in this study, it is acceptable to use real shaped human head models to perform pre-validation studies on the influence of head orientation during tDCS. However, considering the positive pre-validation outcomes in supporting such investigations,

more precision studies could be followed up using MRI based high resolution realistic human head model and it would be even better if the MRI data could be obtained while the subject is in standing or seating position, rather than the traditional laying position with brain shift caused by the gravity.

Secondly, the brain and brain tumors utilized in chapter 5 are from separate subjects, the model was still unreal though both MRI datasets of the human head and brain tumors are real. Such a model was a comprised result due to the lack of data sources. Basically, it is possible to obtain the MRI datasets of healthy subjects who are free from brain tumors to construct the healthy control models to setup the baseline. In addition, it is also possible to access the MRI datasets of the patients with brain tumors to construct the proposed models with brain tumors. But to the best of our knowledge, it is not yet possible to get the healthy MRI datasets (free from brain tumors) and the target MRI datasets (with brain tumors) from the same subject to construct a real MRI based high resolution realistic human head model with no artificial facts. Though it is unlikely to bring too much difference, it would be still better than the current comprised solutions in this project.

Thirdly, this study investigated the influence of tumor locations, tumor grade and even the surrounding edema on the current distributions during tDCS, it did not cover the aspects of tumor size and growing though such work was briefly mentioned and hypothesis of the possible influence was also made in chapter 5. Based on the current results, the simulation with growing tumor grade and size would be more convincing and will be able to quantitatively and systematically address the influence of tumor in realistic situations.

This study also defined the role of blood vessels in shaping the current distribution during tDCS, and provided a value and cost analysis of increasing the model complexity by introducing blood vessels system. However, due to the MRA data quality, the segmentation and registration methodologies of blood vessels utilized in this study took considerably more time to ensure the accuracy and precision. Such work could be much easier with the application of the most recent 7T MRI scanners, which at the same time, provides the possibility to obtain more detailed anatomical features for the modelling with higher accuracy and precision in the tissue classifications and segmentations. Therefore, with the proliferation of 7T MRI

scanners, the application of such devices in the tDCS modelling should be a preferred direction for precision required tDCS studies in the future.

Due to the scope limitation of this project, the validation of computational tDCS models were not proposed as research interest initially. It was well reported that validation of computational tDCS models against the clinical experiments still remains as a challenge due to the lack of reliable method in measuring the in vivo current distributions (Bai et al., 2014, Lee et al., 2012). However, as pointed out in Chapter 3, the simulation workflow proposed in this project was highly consistent with the most recent studies, which were agreed and published as peer reviewed works. Specifically, both the computational theories and electrical properties used in this project were derived from reliable resources with solid reputations while the proposed realistic human head model constructions and calculations were performed on the published open access platforms and credited commercial software packages. After strictly following those protocols, the data obtained from the models constructed in this project were all in reasonable range and showed great agreement with the published results. Still, the customized tDCS model validation against the clinical observations are still expected as the future work. In the near future, the validation could be carried out by utilizing the fMRI-friendly tDCS devices or applying other real time imaging techniques to check the induced current distribution pattern within the patients.

REFERENCES

ABRAMS, R. 2002. *Electroconvulsive therapy*, Oxford University Press.

ADMINISTRATION, F. A. D. 2008. *Notification for NeuroStar® TMS Therapy System for Major Depressive Disorder* [Online]. Available: http://www.accessdata.fda.gov/cdrh_docs/pdf8/K083538.pdf [Accessed 10.6 2016].

ADMINISTRATION, F. A. D. 2009. FDA approves humanitarian device exemption for deep brain stimulator for severe obsessive-compulsive disorder.

ADMINISTRATION, F. A. D. 2015a. FDA approves brain implant to help reduce Parkinson's disease and essential tremor symptoms. June 12, 2015.

ADMINISTRATION, F. A. D. 2015b. *MagVita TMS Therapy System: Treatment of Major Depressive Disorder in adult patients who have failed to receive satisfactory improvement from prior antidepressant medication in the current episode* [Online]. Available: http://www.accessdata.fda.gov/cdrh_docs/pdf15/K150641.pdf [Accessed 10.6 2016].

AGAMANOLIS, D. 2016. *TUMORS OF THE CENTRAL NERVOUS SYSTEM* [Online]. Available: <http://neuropathology-web.org/chapter7/chapter7dMiscellaneous.html> [Accessed 31 May 2016].

ALDINI, G. 1804. *Essai theorique et experimental sur le galvanisme, avec une serie d'experiences... par Jean Aldini... avec planches*, De l'imprimerie de Fournier Fils.

ALEXANDRE F, D., MAGDALENA SARAH, V., MAROM, B. & FELIPE, F. 2011. Electrode positioning and montage in transcranial direct current stimulation. *Journal of Visualized Experiments*.

ALI, M. M., SELLERS, K. K. & FRÖHLICH, F. 2013. Transcranial alternating current stimulation modulates large-scale cortical network activity by network resonance. *The Journal of Neuroscience*, 33, 11262-11275.

ANTAL, A., BOROS, K., POREISZ, C., CHAIEB, L., TERNEY, D. & PAULUS, W. 2008a. Comparatively weak after-effects of transcranial alternating current stimulation (tACS) on cortical excitability in humans. *Brain stimulation*, 1, 97-105.

ANTAL, A., BREPOHL, N., POREISZ, C., BOROS, K., CSIFCSAK, G. & PAULUS, W. 2008b. Transcranial Direct Current Stimulation Over Somatosensory Cortex Decreases Experimentally Induced Acute Pain Perception. *The Clinical journal of pain*, 24, 56-63.

ANTAL, A., KEESER, D., PRIORI, A., PADBERG, F. & NITSCHKE, M. 2015. Conceptual and Procedural Shortcomings of the Systematic Review" Evidence That Transcranial Direct Current Stimulation (tDCS) Generates Little-to-no Reliable Neurophysiologic Effect Beyond MEP Amplitude Modulation in Healthy Human

Subjects: A Systematic Review" by Horvath and Co-workers. *Brain stimulation*, 8, 846.

ANTAL, A., KINCSES, T. Z., NITSCHKE, M. A., BARTFAI, O. & PAULUS, W. 2004a. Excitability changes induced in the human primary visual cortex by transcranial direct current stimulation: direct electrophysiological evidence. *Investigative ophthalmology & visual science*, 45, 702-707.

ANTAL, A., NITSCHKE, M. A., KINCSES, T. Z., KRUSE, W., HOFFMANN, K. P. & PAULUS, W. 2004b. Facilitation of visuo-motor learning by transcranial direct current stimulation of the motor and extrastriate visual areas in humans. *European Journal of Neuroscience*, 19, 2888-2892.

ANTAL, A. & PAULUS, W. 2013. Transcranial alternating current stimulation (tACS). *Frontiers in human neuroscience*, 7.

ANTAL, A., POLANIA, R., SCHMIDT-SAMOA, C., DECHENT, P. & PAULUS, W. 2011. Transcranial direct current stimulation over the primary motor cortex during fMRI. *Neuroimage*, 55, 590-596.

ANTAL, A., TERNEY, D., KÜHNEL, S. & PAULUS, W. 2010. Anodal transcranial direct current stimulation of the motor cortex ameliorates chronic pain and reduces short intracortical inhibition. *Journal of pain and symptom management*, 39, 890-903.

ARLE, J. E. & SHILS, J. L. 2011. *Essential neuromodulation*, Academic Press.

ARUL-ANANDAM, A. P. & LOO, C. 2009. Transcranial direct current stimulation: a new tool for the treatment of depression? *Journal of affective disorders*, 117, 137-145.

BAI, S., DOKOS, S., HO, K.-A. & LOO, C. 2014. A computational modelling study of transcranial direct current stimulation montages used in depression. *Neuroimage*, 87, 332-344.

BAI, S., LOO, C., AL ABED, A. & DOKOS, S. 2012. A computational model of direct brain excitation induced by electroconvulsive therapy: comparison among three conventional electrode placements. *Brain stimulation*, 5, 408-421.

BAI, S., LOO, C. & DOKOS, S. 2013a. A Review of Computational Models of Transcranial Electrical Stimulation. *Critical Reviews™ in Biomedical Engineering*, 41, 21-35.

BAI, S., LOO, C. & DOKOS, S. 2013b. A review of computational models of transcranial electrical stimulation. *Critical Reviews™ in Biomedical Engineering*, 41.

BAILEY, P. & BREMER, F. 1938. A sensory cortical representation of the vagus nerve: with a note on the effects of low blood pressure on the cortical electrogram. *Journal of Neurophysiology*, 1, 405-412.

- BAUER, S., WIEST, R., NOLTE, L.-P. & REYES, M. 2013. A survey of MRI-based medical image analysis for brain tumor studies. *Physics in medicine and biology*, 58, R97.
- BAUMANN, S. B., WOZNY, D. R., KELLY, S. K. & MENO, F. M. 1997a. The electrical conductivity of human cerebrospinal fluid at body temperature. *IEEE Transactions on Biomedical Engineering*, 44, 220-223.
- BAUMANN, S. B., WOZNY, D. R., KELLY, S. K. & MENO, F. M. 1997b. The electrical conductivity of human cerebrospinal fluid at body temperature. *Biomedical Engineering, IEEE Transactions on*, 44, 220-223.
- BELEHRADEK, M., DOMENGE, C., LUBOINSKI, B., ORLOWSKI, S., BELEHRADEK, J. & MIR, L. M. 1993. Electrochemotherapy, a new antitumor treatment. First clinical phase I-II trial. *Cancer*, 72, 3694-3700.
- BENABID, A., POLLAK, P., HOMMEL, M., GAIO, J., DE ROUGEMONT, J. & PERRET, J. 1988a. [Treatment of Parkinson tremor by chronic stimulation of the ventral intermediate nucleus of the thalamus]. *Revue neurologique*, 145, 320-323.
- BENABID, A. L. 2003. Deep brain stimulation for Parkinson's disease. *Current opinion in neurobiology*, 13, 696-706.
- BENABID, A. L., POLLAK, P., LOUVEAU, A., HENRY, S. & DE ROUGEMONT, J. 1988b. Combined (thalamotomy and stimulation) stereotactic surgery of the VIM thalamic nucleus for bilateral Parkinson disease. *Stereotactic and functional neurosurgery*, 50, 344-346.
- BENWELL, C. S., LEARMONTH, G., MINIUSSI, C., HARVEY, M. & THUT, G. 2015. Non-linear effects of transcranial direct current stimulation as a function of individual baseline performance: Evidence from biparietal tDCS influence on lateralized attention bias. *cortex*, 69, 152-165.
- BERNEY, A., VINGERHOETS, F., PERRIN, A., GUEX, P., VILLEMURE, J.-G., BURKHARD, P., BENKELFAT, C. & GHKA, J. 2002. Effect on mood of subthalamic DBS for Parkinson's disease A consecutive series of 24 patients. *Neurology*, 59, 1427-1429.
- BIJSTERBOSCH, J. D., LEE, K.-H., HUNTER, M. D., WILKINSON, I. D., FARROW, T., BARKER, A. T. & WOODRUFF, P. W. 2013. The effect of head orientation on subarachnoid cerebrospinal fluid distribution and its implications for neurophysiological modulation and recording techniques. *Physiological measurement*, 34, N9.
- BIKSON, M., RAHMAN, A. & DATTA, A. 2012a. Computational models of transcranial direct current stimulation. *Clinical EEG and Neuroscience*, 43, 176-183.
- BIKSON, M., RAHMAN, A., DATTA, A., FREGNI, F. & MERABET, L. 2012b. High-Resolution Modeling Assisted Design of Customized and Individualized Transcranial Direct Current Stimulation Protocols. *Neuromodulation: Technology at the Neural Interface*, 15, 306-315.

- BIKSON, M., TRUONG, D. Q., MOURDOUKOUTAS, A. P., ABOSERIA, M., KHADKA, N., ADAIR, D. & RAHMAN, A. 2015. Modeling sequence and quasi-uniform assumption in computational neurostimulation. *Progress in brain research*, 222, 1-23.
- BINDMAN, L. J., LIPPOLD, O. & REDFEARN, J. 1964a. The action of brief polarizing currents on the cerebral cortex of the rat (1) during current flow and (2) in the production of long-lasting after-effects. *The Journal of physiology*, 172, 369-382.
- BINDMAN, L. J., LIPPOLD, O. & REDFEARN, J. 1964b. Relation between the size and form of potentials evoked by sensory stimulation and the background electrical activity in the cerebral cortex of the rat. *The Journal of physiology*, 171, 1.
- BINI, L. 1938. 22. EXPERIMENTAL RESEARCHES ON EPILEPTIC ATTACKS INDUCED BY THE ELECTRIC CURRENT. *American Journal of Psychiatry*, 94, 172-174.
- BLANK, R. H. 2016. Introduction to Cognitive Enhancement. *Cognitive Enhancement: Social and Public Policy Issues*. Springer.
- BLAUS, B. 2014. *Cerebrospinal System* [Online]. Wikimedia. Available: https://commons.wikimedia.org/wiki/File:Blausen_0216_CerebrospinalSystem.png#mediaviewer/File:Blausen_0216_CerebrospinalSystem.png.
- BOGGIO, P. S., CASTRO, L. O., SAVAGIM, E. A., BRAITE, R., CRUZ, V. C., ROCHA, R. R., RIGONATTI, S. P., SILVA, M. T. & FREGNI, F. 2006a. Enhancement of non-dominant hand motor function by anodal transcranial direct current stimulation. *Neuroscience letters*, 404, 232-236.
- BOGGIO, P. S., FERRUCCI, R., RIGONATTI, S. P., COVRE, P., NITSCHKE, M., PASCUAL-LEONE, A. & FREGNI, F. 2006b. Effects of transcranial direct current stimulation on working memory in patients with Parkinson's disease. *Journal of the neurological sciences*, 249, 31-38.
- BOGGIO, P. S., NUNES, A., RIGONATTI, S. P., NITSCHKE, M. A., PASCUAL-LEONE, A. & FREGNI, F. 2007. Repeated sessions of noninvasive brain DC stimulation is associated with motor function improvement in stroke patients. *Restorative neurology and neuroscience*, 25, 123-129.
- BROWN, L. G. 1992. A survey of image registration techniques. *ACM computing surveys (CSUR)*, 24, 325-376.
- BRUNONI, A. R., NITSCHKE, M. A., BOLOGNINI, N., BIKSON, M., WAGNER, T., MERABET, L., EDWARDS, D. J., VALERO-CABRE, A., ROTENBERG, A. & PASCUAL-LEONE, A. 2012. Clinical research with transcranial direct current stimulation (tDCS): challenges and future directions. *Brain stimulation*, 5, 175-195.
- BULLOCK, T. H., HOPKINS, C. D. & FAY, R. R. 2006. *Electroreception*, Springer Science & Business Media.

- CHEN, Y., GUNAWAN, E., LOW, K. S., WANG, S.-C., SOH, C. B. & PUTTI, T. C. 2008. Effect of lesion morphology on microwave signature in 2-D ultra-wideband breast imaging. *Biomedical Engineering, IEEE Transactions on*, 55, 2011-2021.
- CHESLER, M. 2003. Regulation and modulation of pH in the brain. *Physiological reviews*, 83, 1183-1221.
- CLARK, G. & WARD, J. W. 1948. Responses elicited from the cortex of monkeys by electrical stimulation through fixed electrodes. *Brain*, 71, 332-342.
- CLARK, V. P. & PARASURAMAN, R. 2014. Neuroenhancement: enhancing brain and mind in health and in disease. *Neuroimage*, 85, 889-894.
- CLOCK JR, G. D. & LYTE, M. Potential uses of low-level direct current electrotherapy for the treatment of cancer. Engineering in Medicine and Biology Society, 1993. Proceedings of the 15th Annual International Conference of the IEEE, 1993. IEEE, 1515-1516.
- COCOSCO, C. A., KOLLOKIAN, V., KWAN, R. K.-S., PIKE, G. B. & EVANS, A. C. BrainWeb: Online interface to a 3D MRI simulated brain database. *NeuroImage*, 1997. Citeseer.
- DASILVA, A. F., VOLZ, M. S., BIKSON, M. & FREGNI, F. 2011a. Electrode positioning and montage in transcranial direct current stimulation. *Journal of visualized experiments: JoVE* [Online].
- DASILVA, A. F., VOLZ, M. S., BIKSON, M. & FREGNI, F. 2011b. Electrode positioning and montage in transcranial direct current stimulation. *JoVE (Journal of Visualized Experiments)*, e2744-e2744.
- DATTA, A., BAKER, J. M., BIKSON, M. & FRIDRIKSSON, J. 2011. Individualized model predicts brain current flow during transcranial direct-current stimulation treatment in responsive stroke patient. *Brain stimulation*, 4, 169-174.
- DATTA, A., BANSAL, V., DIAZ, J., PATEL, J., REATO, D. & BIKSON, M. 2009. Gyri-precise head model of transcranial direct current stimulation: improved spatial focality using a ring electrode versus conventional rectangular pad. *Brain stimulation*, 2, 201-207. e1.
- DATTA, A., BIKSON, M. & FREGNI, F. 2010. Transcranial direct current stimulation in patients with skull defects and skull plates: high-resolution computational FEM study of factors altering cortical current flow. *Neuroimage*, 52, 1268-1278.
- DATTA, A., ELWASSIF, M., BATTAGLIA, F. & BIKSON, M. 2008a. Transcranial current stimulation focality using disc and ring electrode configurations: FEM analysis. *Journal of neural engineering*, 5, 163-174.
- DATTA, A., ELWASSIF, M., BATTAGLIA, F. & BIKSON, M. 2008b. Transcranial current stimulation focality using disc and ring electrode configurations: FEM analysis. *Journal of neural engineering*, 5, 163.

DATTA, A., TRUONG, D., MINHAS, P., PARRA, L. C. & BIKSON, M. 2012. Inter-individual variation during transcranial direct current stimulation and normalization of dose using MRI-derived computational models.

DAVIES, A. M., WEINBERG, U. & PALTU, Y. 2013. Tumor treating fields: a new frontier in cancer therapy. *Annals of the New York Academy of Sciences*, 1291, 86-95.

DE OLIVEIRA, M. M., WEN, P. & AHFOCK, T. 2016. Heat transfer due to electroconvulsive therapy: influence of anisotropic thermal and electrical skull conductivity. *Computer Methods and Programs in Biomedicine*.

DELGADO, J. M., ROBERTS, W. W. & MILLER, N. E. 1954. Learning motivated by electrical stimulation of the brain. *American Journal of Physiology--Legacy Content*, 179, 587-593.

DELL, P. & OLSON, R. 1951. [Thalamic, cortical and cerebellar projections of vagal visceral afferences.]. *Comptes rendus des seances de la Societe de biologie et de ses filiales*, 145, 1084-1088.

DENG, Z.-D., LISANBY, S. H. & PETERCHEV, A. V. 2011. Electric field strength and focality in electroconvulsive therapy and magnetic seizure therapy: a finite element simulation study. *Journal of neural engineering*, 8, 016007.

DENG, Z.-D., PETERCHEV, A. V. & LISANBY, S. H. Coil design considerations for deep-brain transcranial magnetic stimulation (dTMS). Engineering in Medicine and Biology Society, 2008. EMBS 2008. 30th Annual International Conference of the IEEE, 2008. IEEE, 5675-5679.

DOTY, R. W. 1969. Electrical stimulation of the brain in behavioral context. *Annual review of psychology*, 20, 289-320.

DRECHSLER, F., WOLTERS, C. H., DIERKES, T., SI, H. & GRASEDYCK, L. 2009. A full subtraction approach for finite element method based source analysis using constrained Delaunay tetrahedralisation. *NeuroImage*, 46, 1055-1065.

EDWARDS, B. K., NOONE, A. M., MARIOTTO, A. B., SIMARD, E. P., BOSCOE, F. P., HENLEY, S. J., JEMAL, A., CHO, H., ANDERSON, R. N. & KOHLER, B. A. 2014. Annual Report to the Nation on the status of cancer, 1975-2010, featuring prevalence of comorbidity and impact on survival among persons with lung, colorectal, breast, or prostate cancer. *Cancer*, 120, 1290-1314.

ENDLER, N. S. 1988. The origins of electroconvulsive therapy (ECT). *The Journal of ECT*, 4, 5-23.

FARIA, P., HALLETT, M. & MIRANDA, P. C. 2011. A finite element analysis of the effect of electrode area and inter-electrode distance on the spatial distribution of the current density in tDCS. *Journal of neural engineering*, 8, 066017.

FEDOROV, A., BEICHEL, R., KALPATHY-CRAMER, J., FINET, J., FILLION-ROBIN, J.-C., PUJOL, S., BAUER, C., JENNINGS, D., FENNESSY, F. & SONKA,

M. 2012. 3D Slicer as an image computing platform for the Quantitative Imaging Network. *Magnetic resonance imaging*, 30, 1323-1341.

FERDJALLAH, M., BOSTICK, F. & BARR, R. 1996. Potential and current density distributions of cranial electrotherapy stimulation (CES) in a four-concentric-spheres model. *Biomedical Engineering, IEEE Transactions on*, 43, 939-943.

FERTONANI, A. & MINIUSI, C. 2016. Transcranial Electrical Stimulation What We Know and Do Not Know About Mechanisms. *The Neuroscientist*, 1073858416631966.

FIEDERER, L., VORWERK, J., LUCKA, F., DANNHAUER, M., YANG, S., DÜMPELMANN, M., SCHULZE-BONHAGE, A., AERTSEN, A., SPECK, O. & WOLTERS, C. 2016. The role of blood vessels in high-resolution volume conductor head modeling of EEG. *NeuroImage*, 128, 193-208.

FISHMAN, R. A. 1975. Brain edema. *New England Journal of Medicine*, 293, 706-711.

FORSYTH, P. A. & POSNER, J. B. 1993. Headaches in patients with brain tumors A study of 111 patients. *Neurology*, 43, 1678-1678.

FRASER, L. M., O'CARROLL, R. E. & EBMEIER, K. P. 2008. The effect of electroconvulsive therapy on autobiographical memory: a systematic review. *The journal of ECT*, 24, 10-17.

FRICKE, H. & MORSE, S. 1926. The electric capacity of tumors of the breast. *The Journal of Cancer Research*, 10, 340-376.

GABRIEL, C., GABRIEL, S. & CORTHOUT, E. 1996a. The dielectric properties of biological tissues: I. Literature survey. *Physics in medicine and biology*, 41, 2231.

GABRIEL, S., LAU, R. & GABRIEL, C. 1996b. The dielectric properties of biological tissues: II. Measurements in the frequency range 10 Hz to 20 GHz. *Physics in medicine and biology*, 41, 2251.

GANDIGA, P. C., HUMMEL, F. C. & COHEN, L. G. 2006. Transcranial DC stimulation (tDCS): a tool for double-blind sham-controlled clinical studies in brain stimulation. *Clinical Neurophysiology*, 117, 845-850.

GARCIA, P. A., ROSSMEISL, J. H. & DAVALOS, R. V. Electrical conductivity changes during irreversible electroporation treatment of brain cancer. Engineering in Medicine and Biology Society, EMBC, 2011 Annual International Conference of the IEEE, 2011. IEEE, 739-742.

GEDDES, L. & BAKER, L. 1967. The specific resistance of biological material—a compendium of data for the biomedical engineer and physiologist. *Medical and biological engineering*, 5, 271-293.

GEORGE, M. S. & ASTON-JONES, G. 2010. Noninvasive techniques for probing neurocircuitry and treating illness: vagus nerve stimulation (VNS), transcranial

magnetic stimulation (TMS) and transcranial direct current stimulation (tDCS). *Neuropsychopharmacology*, 35, 301-316.

GMBH, N. 2016. *neuroConn DC-STIMULATORs cover all requirements for transcranial stimulation*. [Online]. Available: http://www.neuroconn.de/dc-stimulator_plus_en/ [Accessed 1.6 2016].

GODDARD, G. V., MCINTYRE, D. C. & LEECH, C. K. 1969. A permanent change in brain function resulting from daily electrical stimulation. *Experimental neurology*, 25, 295-330.

GONÇALVES, S., DE MUNCK, J. C., VERBUNT, J., HEETHAAR, R. M. & DA SILVA, F. 2003. In vivo measurement of the brain and skull resistivities using an EIT-based method and the combined analysis of SEF/SEP data. *IEEE transactions on biomedical engineering*, 50, 1124-1128.

GRANDORI, F. & ROSSINI, P. 1988. Electrical stimulation of the motor cortex: theoretical considerations. *Annals of biomedical engineering*, 16, 639-652.

GRANT, R. 2004. Overview: brain tumour diagnosis and management/Royal College of Physicians guidelines. *Journal of Neurology, Neurosurgery & Psychiatry*, 75, ii18-ii23.

GREENBERG, R. M. & KELLNER, C. H. 2005. Electroconvulsive therapy: a selected review. *The American journal of geriatric psychiatry*, 13, 268-281.

GRIFFIN, D., DODD, N., MOORE, J. V., PULLAN, B. & TAYLOR, T. 1994. The effects of low-level direct current therapy on a preclinical mammary carcinoma: tumour regression and systemic biochemical sequelae. *British journal of cancer*, 69, 875.

GRILL-SPECTOR, K., KUSHNIR, T., HENDLER, T., EDELMAN, S., ITZCHAK, Y. & MALACH, R. 1998. A sequence of object-processing stages revealed by fMRI in the human occipital lobe. *Human brain mapping*, 6, 316-328.

GUNGOR, K. & EMPTING, L. 2016. (392) Effects of alternating current trans-cranial stimulation on pain related depression and neuropathic pain in industrial limb injuries including CRPS. *The Journal of Pain*, 17, S73.

HALTER, R. J., SCHNED, A. R., HEANEY, J. A. & HARTOV, A. 2011. Passive bioelectrical properties for assessing high-and low-grade prostate adenocarcinoma. *The Prostate*, 71, 1759-1767.

HARRIS, G. 1937. The induction of ovulation in the rabbit, by electrical stimulation of the hypothalamo-hypophysial mechanism. *Proceedings of the Royal Society of London. Series B, Biological Sciences*, 122, 374-394.

HE, B. 2004. *Modeling and Imaging of Bioelectrical Activity*. Springer.

HELLER, L. & VAN HULSTEYN, D. B. 1992. Brain stimulation using electromagnetic sources: theoretical aspects. *Biophysical journal*, 63, 129-138.

- HELLERHOFF. 2016. *Deep Brain Stimulation* [Online]. Wiki Pedia. Available: https://commons.wikimedia.org/wiki/File:Tiefe_Hirnstimulation_-_Sonden_RoeSchaedel_ap.jpg#/media/File:Tiefe_Hirnstimulation_-_Sonden_RoeSchaedel_seitl.jpg [Accessed 20.6 2016].
- HESSE, S., WERNER, C., SCHONHARDT, E., BARDELEBEN, A., JENRICH, W. & KIRKER, S. 2007. Combined transcranial direct current stimulation and robot-assisted arm training in subacute stroke patients: a pilot study. *Restorative neurology and neuroscience*, 25, 9-15.
- HO, M.-W. 1996. Bioenergetics and biocommunication. *Computation in Cellular and Molecular Biological Systems*, 251-264.
- HOLDEFER, R., SADLEIR, R. & RUSSELL, M. 2006. Predicted current densities in the brain during transcranial electrical stimulation. *Clinical neurophysiology*, 117, 1388-1397.
- HORVATH, J. C., FORTE, J. D. & CARTER, O. 2015a. Evidence that transcranial direct current stimulation (tDCS) generates little-to-no reliable neurophysiologic effect beyond MEP amplitude modulation in healthy human subjects: a systematic review. *Neuropsychologia*, 66, 213-236.
- HORVATH, J. C., FORTE, J. D. & CARTER, O. 2015b. Quantitative review finds no evidence of cognitive effects in healthy populations from single-session transcranial direct current stimulation (tDCS). *Brain stimulation*, 8, 535-550.
- HOY, K. E. & FITZGERALD, P. B. 2010. Brain stimulation in psychiatry and its effects on cognition. *Nature Reviews Neurology*, 6, 267-275.
- HU, J., JIN, X., LEE, J. B., ZHANG, L., CHAUDHARY, V., GUTHIKONDA, M., YANG, K. H. & KING, A. I. 2007. Intraoperative brain shift prediction using a 3D inhomogeneous patient-specific finite element model. *Journal of neurosurgery*, 106, 164-169.
- IKEDA, Y. & MATSUMOTO, K. 1999. Peritumoral Brain Edema. *The Showa University Journal of Medical Sciences*, 11, 149-154.
- INGRAM, A., SALING, M. M. & SCHWEITZER, I. 2008. Cognitive side effects of brief pulse electroconvulsive therapy: a review. *The journal of ECT*, 24, 3-9.
- JENKINSON, M., BECKMANN, C. F., BEHRENS, T. E., WOOLRICH, M. W. & SMITH, S. M. 2012. Fsl. *Neuroimage*, 62, 782-790.
- JHA, S. 2003. Cerebral edema and its management. *Medical Journal Armed Forces India*, 59, 326-331.
- KAAL, E. C. & VECHT, C. J. 2004. The management of brain edema in brain tumors. *Current opinion in oncology*, 16, 593-600.

- KADOSH, R. C., SOSKIC, S., IUCULANO, T., KANAI, R. & WALSH, V. 2010. Modulating neuronal activity produces specific and long-lasting changes in numerical competence. *Current Biology*, 20, 2016-2020.
- KATSCHER, U., KIM, D.-H. & SEO, J. K. 2013. Recent progress and future challenges in MR electric properties tomography. *Computational and mathematical methods in medicine*, 2013.
- KATSCHER, U., VOIGT, T., FINDEKLEE, C., VERNICKEL, P., NEHRKE, K. & DOSSEL, O. 2009. Determination of electric conductivity and local SAR via B1 mapping. *Medical Imaging, IEEE Transactions on*, 28, 1365-1374.
- KAUS, M. R., WARFIELD, S. K., NABAVI, A., BLACK, P. M., JOLESZ, F. A. & KIKINIS, R. 2001. Automated segmentation of MR images of brain tumors. *Radiology*, 218, 586-591.
- KELLAWAY, P. 1946. The part played by electric fish in the early history of bioelectricity and electrotherapy. *Bulletin of the History of Medicine*, 20, 112.
- KIM, J.-H., KIM, D.-W., CHANG, W. H., KIM, Y.-H., KIM, K. & IM, C.-H. 2014a. Inconsistent outcomes of transcranial direct current stimulation may originate from anatomical differences among individuals: electric field simulation using individual MRI data. *Neuroscience Letters*, 564, 6-10.
- KIM, S., STEPHENSON, M. C., MORRIS, P. G. & JACKSON, S. R. 2014b. tDCS-induced alterations in GABA concentration within primary motor cortex predict motor learning and motor memory: A 7T magnetic resonance spectroscopy study. *Neuroimage*, 99, 237-243.
- KIRSON, E. D., DBALÝ, V., TOVARYŠ, F., VYMAZAL, J., SOUSTIEL, J. F., ITZHAKI, A., MORDECHOVICH, D., STEINBERG-SHAPIRA, S., GURVICH, Z. & SCHNEIDERMAN, R. 2007. Alternating electric fields arrest cell proliferation in animal tumor models and human brain tumors. *Proceedings of the National Academy of Sciences*, 104, 10152-10157.
- KIRSON, E. D., GURVICH, Z., SCHNEIDERMAN, R., DEKEL, E., ITZHAKI, A., WASSERMAN, Y., SCHATZBERGER, R. & PALTÍ, Y. 2004. Disruption of cancer cell replication by alternating electric fields. *Cancer research*, 64, 3288-3295.
- KIRSON, E. D., SCHNEIDERMAN, R. S., DBALÝ, V., TOVARYŠ, F., VYMAZAL, J., ITZHAKI, A., MORDECHOVICH, D., GURVICH, Z., SHMUELI, E. & GOLDSHER, D. 2009. Chemotherapeutic treatment efficacy and sensitivity are increased by adjuvant alternating electric fields (TTFields). *BMC medical physics*, 9, 1.
- KLEIHUES, P., BURGER, P. C. & SCHEITHAUER, B. W. 1993. The new WHO classification of brain tumours. *Brain Pathology*, 3, 255-268.
- KOENIGS, M., UKUEBERUWA, D., CAMPION, P., GRAFMAN, J. & WASSERMANN, E. 2009. Bilateral frontal transcranial direct current stimulation:

failure to replicate classic findings in healthy subjects. *Clinical Neurophysiology*, 120, 80-84.

KRAWCZYK, A. & ŁADA-TONDYRA, E. 2010. The first experiments in magnetic stimulation—a history of discoveries within two parallel lives. *Acta Technica Jaurinensis*, 3, 153-160.

KROON, D.-J. 11 June 2009. *MathWorks File Exchange Hessian based Frangi Vesselness filter* [Online]. Available: <http://www.mathworks.com/matlabcentral/fileexchange/24409-hessian-based-frangi-vesselness-filter> [Accessed 5 February 2016].

KRYSTAL, A. D. & WEINER, R. D. 1994. ECT seizure therapeutic adequacy. *The Journal of ECT*, 10, 153-164.

KUBA, R. 2013. Effect of VNS on mood. *Epilepsy & Behavior*, 28, 316.

KWON, O. I., SAJIB, S. Z., SERSA, I., OH, T. I., JEONG, W. C., KIM, H. J. & WOO, E. J. 2016. Current Density Imaging During Transcranial Direct Current Stimulation Using DT-MRI and MREIT: Algorithm Development and Numerical Simulations. *Biomedical Engineering, IEEE Transactions on*, 63, 168-175.

LAAKSO, I., TANAKA, S., MIKKONEN, M., KOYAMA, S., SADATO, N. & HIRATA, A. 2016. Electric fields of motor and frontal tDCS in a standard brain space: A computer simulation study. *NeuroImage*.

LANSKA, D. J. 2002. JL Corning and vagal nerve stimulation for seizures in the 1880s. *Neurology*, 58, 452-459.

LEE, W. H., DENG, Z.-D., KIM, T.-S., LAINE, A. F., LISANBY, S. H. & PETERCHEV, A. V. 2012. Regional electric field induced by electroconvulsive therapy in a realistic finite element head model: influence of white matter anisotropic conductivity. *Neuroimage*, 59, 2110-2123.

LEFAUCHEUR, J.-P., ANTAL, A., AHDAB, R., DE ANDRADE, D. C., FREGNI, F., KHEDR, E. M., NITSCHKE, M. & PAULUS, W. 2008. The use of repetitive transcranial magnetic stimulation (rTMS) and transcranial direct current stimulation (tDCS) to relieve pain. *Brain Stimulation*, 1, 337-344.

LEIKNES, K. A., COOKE, M. J., JAROSCH-VON SCHWEDER, L., HARBOE, I. & HØIE, B. 2015. Electroconvulsive therapy during pregnancy: a systematic review of case studies. *Archives of women's mental health*, 18, 1-39.

LETTEBOER, M. M. J., WILLEMS, P. W., VIERGEVER, M. A. & NIESSEN, W. J. 2005. Brain shift estimation in image-guided neurosurgery using 3-D ultrasound. *Biomedical Engineering, IEEE Transactions on*, 52, 268-276.

LI, L. M., UEHARA, K. & HANAKAWA, T. 2015. The contribution of interindividual factors to variability of response in transcranial direct current stimulation studies. *Frontiers in cellular neuroscience*, 9, 181.

- LIEBETANZ, D., KOCH, R., MAYENFELS, S., KÖNIG, F., PAULUS, W. & NITSCHKE, M. A. 2009. Safety limits of cathodal transcranial direct current stimulation in rats. *Clinical Neurophysiology*, 120, 1161-1167.
- LIEBETANZ, D., NITSCHKE, M. A., TERGAU, F. & PAULUS, W. 2002. Pharmacological approach to the mechanisms of transcranial DC-stimulation-induced after-effects of human motor cortex excitability. *Brain*, 125, 2238-2247.
- LIER, A. L., RAAIJMAKERS, A., VOIGT, T., LAGENDIJK, J. J., LUIJTEN, P. R., KATSCHER, U. & BERG, C. A. 2014. Electrical properties tomography in the human brain at 1.5, 3, and 7T: a comparison study. *Magnetic Resonance in Medicine*, 71, 354-363.
- LININGTON, A. & HARRIS, B. 1988. Fifty years of electroconvulsive therapy. *BMJ: British Medical Journal*, 297, 1354.
- LISANBY, S. H. 2007. Electroconvulsive therapy for depression. *New England Journal of Medicine*, 357, 1939-1945.
- LOCKARD, J. S., CONGDON, W. C. & DUCHARME, L. L. 1990. Feasibility and safety of vagal stimulation in monkey model. *Epilepsia*, 31, S20-S26.
- LOO, C. K. & MITCHELL, P. B. 2005. A review of the efficacy of transcranial magnetic stimulation (TMS) treatment for depression, and current and future strategies to optimize efficacy. *Journal of affective disorders*, 88, 255-267.
- LULIC, D., AHMADIAN, A., BAAJ, A. A., BENBADIS, S. R. & VALE, F. L. 2009. Vagus nerve stimulation. *Neurosurgical focus*, 27, E5.
- MAGIS, D., JENSEN, R. & SCHOENEN, J. 2012. Neurostimulation therapies for primary headache disorders: present and future. *Current opinion in neurology*, 25, 269-276.
- MAI, J. K., MAJTANIK, M. & PAXINOS, G. 2016. *Atlas of the human brain*, Academic Press.
- MALAMUD, N. 1967. Psychiatric disorder with intracranial tumors of limbic system. *Archives of Neurology*, 17, 113-123.
- MALMIVUO, J. & PLONSEY, R. 1995. *Bioelectromagnetism: principles and applications of bioelectric and biomagnetic fields*, Oxford University Press, USA.
- MANOLI, Z., GROSSMAN, N. & SAMARAS, T. Theoretical investigation of transcranial alternating current stimulation using realistic head model. 2012 Annual International Conference of the IEEE Engineering in Medicine and Biology Society, 2012. IEEE, 4156-4159.
- MARANGELL, L. B., RUSH, A. J., GEORGE, M. S., SACKEIM, H. A., JOHNSON, C. R., HUSAIN, M. M., NAHAS, Z. & LISANBY, S. H. 2002. Vagus nerve stimulation (VNS) for major depressive episodes: one year outcomes. *Biological psychiatry*, 51, 280-287.

- MAYBERG, H. S., LOZANO, A. M., VOON, V., MCNEELY, H. E., SEMINOWICZ, D., HAMANI, C., SCHWALB, J. M. & KENNEDY, S. H. 2005. Deep brain stimulation for treatment-resistant depression. *Neuron*, 45, 651-660.
- MAZZIOTTA, J., TOGA, A., EVANS, A., FOX, P., LANCASTER, J., ZILLES, K., WOODS, R., PAUS, T., SIMPSON, G. & PIKE, B. 2001. A probabilistic atlas and reference system for the human brain: International Consortium for Brain Mapping (ICBM). *Philosophical Transactions of the Royal Society of London B: Biological Sciences*, 356, 1293-1322.
- MCCONNELL BRAIN IMAGING CENTRE, M. U. 2014. *BrainWeb: Simulated Brain Database (SBD)* [Online]. Available: <http://www.bic.mni.mcgill.ca/brainweb/>.
- MCLACHLAN, R. S. 1993. Suppression of interictal spikes and seizures by stimulation of the vagus nerve. *Epilepsia*, 34, 918-923.
- MENG, Z. J., SAJIB, S. Z., CHAUHAN, M., SADLEIR, R. J., KIM, H. J., KWON, O. I. & WOO, E. J. 2013. Numerical Simulations of MREIT Conductivity Imaging for Brain Tumor Detection. *Computational and mathematical methods in medicine*, 2013.
- MEYERS, C. A., WEITZNER, M. A., VALENTINE, A. D. & LEVIN, V. A. 1998. Methylphenidate therapy improves cognition, mood, and function of brain tumor patients. *Journal of Clinical Oncology*, 16, 2522-2527.
- MIKLAVČIČ, D., ŠEMROV, D., VALENČIČ, V., SERŠA, G. & VODOVNIK, L. 1997. Tumor treatment by direct electric current: computation of electric current and power density distribution. *Electro-and Magnetobiology*, 16, 119-128.
- MINHAS, P., BANSAL, V., PATEL, J., HO, J. S., DIAZ, J., DATTA, A. & BIKSON, M. 2010. Electrodes for high-definition transcutaneous DC stimulation for applications in drug delivery and electrotherapy, including tDCS. *Journal of neuroscience methods*, 190, 188-197.
- MIRANDA, P. C., FARIA, P. & HALLETT, M. 2009. What does the ratio of injected current to electrode area tell us about current density in the brain during tDCS? *Clinical Neurophysiology*, 120, 1183-1187.
- MIRANDA, P. C., LOMAREV, M. & HALLETT, M. 2006. Modeling the current distribution during transcranial direct current stimulation. *Clinical Neurophysiology*, 117, 1623-1629.
- MONAI, H., OHKURA, M., TANAKA, M., OE, Y., KONNO, A., HIRAI, H., MIKOSHIBA, K., ITOHARA, S., NAKAI, J. & IWAI, Y. 2016. Calcium imaging reveals glial involvement in transcranial direct current stimulation-induced plasticity in mouse brain. *Nature communications*, 7.
- MOORE, E. 2016. *Medical Illustration: Novel Treatments for Glioblastoma* [Online]. www.curetoday.com; Curetoday.com. Available: <http://www.curetoday.com/publications/cure/2016/winter-2016/medical-illustration-novel-treatments-for-glioblastoma> [Accessed 25.6 2016].

MYERS, D. G. 2004. *Exploring psychology*, Macmillan.

MYERS, D. G. 2010. *Psychology*, Worth Publishers.

NEUMANN, E., SCHAEFER-RIDDER, M., WANG, Y. & HOFSCHEIDER, P. 1982. Gene transfer into mouse lymphoma cells by electroporation in high electric fields. *The EMBO journal*, 1, 841.

NEUROSCIENCE, C. 2012. *TMS* [Online]. www.cognitiveneuroscience.it: Cognitive Neuroscience Section. Available: <http://www.cognitiveneuroscience.it/tms/?lang=en> [Accessed 5.6 2016].

NICHOLSON, P. W. 1965. Specific impedance of cerebral white matter. *Experimental neurology*, 13, 386-401.

NITSCHKE, M. & PAULUS, W. 2000. Excitability changes induced in the human motor cortex by weak transcranial direct current stimulation. *The Journal of physiology*, 527, 633-639.

NITSCHKE, M. A., COHEN, L. G., WASSERMANN, E. M., PRIORI, A., LANG, N., ANTAL, A., PAULUS, W., HUMMEL, F., BOGGIO, P. S. & FREGNI, F. 2008. Transcranial direct current stimulation: state of the art 2008. *Brain stimulation*, 1, 206-223.

NUNEZ, P. L. & SRINIVASAN, R. 2006. *Electric fields of the brain: the neurophysics of EEG*, Oxford university press.

O'SHEA, J. & WALSH, V. 2007. Transcranial magnetic stimulation. *Current Biology*, 17, R196-R199.

O'REARDON, J. P., SOLVASON, H. B., JANICAK, P. G., SAMPSON, S., ISENBERG, K. E., NAHAS, Z., MCDONALD, W. M., AVERY, D., FITZGERALD, P. B. & LOO, C. 2007. Efficacy and safety of transcranial magnetic stimulation in the acute treatment of major depression: a multisite randomized controlled trial. *Biological psychiatry*, 62, 1208-1216.

OJI, C. & ANI, J. 2010. Destruction of an advanced malignant tumour by direct electrical current-case report. *Health*, 2, 1049.

OLDS, J. & MILNER, P. 1954. Positive reinforcement produced by electrical stimulation of septal area and other regions of rat brain. *Journal of comparative and physiological psychology*, 47, 419.

OMAR, A. I. 2014. Tumor treating field therapy in combination with bevacizumab for the treatment of recurrent glioblastoma. *Journal of visualized experiments: JoVE*.

OOSTENDORP, T. F., DELBEKE, J. & STEGEMAN, D. F. 2000a. The conductivity of the human skull: results of in vivo and in vitro measurements. *Biomedical Engineering, IEEE Transactions on*, 47, 1487-1492.

- OOSTENDORP, T. F., DELBEKE, J. & STEGEMAN, D. F. 2000b. The conductivity of the human skull: results of in vivo and in vitro measurements. *IEEE transactions on biomedical engineering*, 47, 1487-1492.
- OPITZ, A., PAULUS, W., WILL, S., ANTUNES, A. & THIELSCHER, A. 2015. Determinants of the electric field during transcranial direct current stimulation. *Neuroimage*, 109, 140-150.
- PANTAZIS, D., JOSHI, A., JIANG, J., SHATTUCK, D. W., BERNSTEIN, L. E., DAMASIO, H. & LEAHY, R. M. 2010. Comparison of landmark-based and automatic methods for cortical surface registration. *Neuroimage*, 49, 2479-2493.
- PAPADOPOULOS, M., SAADOUN, S., BINDER, D., MANLEY, G., KRISHNA, S. & VERKMAN, A. 2004. Molecular mechanisms of brain tumor edema. *Neuroscience*, 129, 1009-1018.
- PARAZZINI, M., FIOCCHI, S., CANCELLI, A., COTTONE, C., LIORNI, I., RAVAZZANI, P. & TECCHIO, F. 2016. A Computational Model of the Electric Field Distribution due to Regional Personalized or Non-Personalized Electrodes to Select Transcranial Electric Stimulation Target.
- PARAZZINI, M., FIOCCHI, S., ROSSI, E., PAGLIALONGA, A. & RAVAZZANI, P. 2011. Transcranial direct current stimulation: estimation of the electric field and of the current density in an anatomical human head model. *Biomedical Engineering, IEEE Transactions on*, 58, 1773-1780.
- PARENT, A. 2004. Giovanni Aldini: from animal electricity to human brain stimulation. *The Canadian Journal of Neurological Sciences*, 31, 576-584.
- PENFIELD, W. & BOLDREY, E. 1937. Somatic motor and sensory representation in the cerebral cortex of man as studied by electrical stimulation. *Brain: A journal of neurology*.
- PERLMUTTER, J. S. & MINK, J. W. 2006. Deep brain stimulation. *Annual review of neuroscience*, 29, 229.
- PETERCHEV, A. V., ROSA, M. A., DENG, Z.-D., PRUDIC, J. & LISANBY, S. H. 2010. ECT stimulus parameters: rethinking dosage. *The journal of ECT*, 26, 159.
- PLESS, M. & WEINBERG, U. 2011. Tumor treating fields: concept, evidence and future. *Expert opinion on investigational drugs*, 20, 1099-1106.
- PLONSEY, R. & HEPPNER, D. B. 1967. Considerations of quasi-stationarity in electrophysiological systems. *The Bulletin of mathematical biophysics*, 29, 657-664.
- POREISZ, C., BOROS, K., ANTAL, A. & PAULUS, W. 2007. Safety aspects of transcranial direct current stimulation concerning healthy subjects and patients. *Brain research bulletin*, 72, 208-214.

- PURPURA, D. P. & MCMURTRY, J. G. 1965. Intracellular activities and evoked potential changes during polarization of motor cortex. *Journal of Neurophysiology*, 28, 166-185.
- RAE, C. D., LEE, V. H.-C., ORDIDGE, R. J., ALONZO, A. & LOO, C. 2013. Anodal transcranial direct current stimulation increases brain intracellular pH and modulates bioenergetics. *International Journal of Neuropsychopharmacology*, 16, 1695-1706.
- REHMAN, A. A., ELMORE, K. B. & MATTEI, T. A. 2015. The effects of alternating electric fields in glioblastoma: current evidence on therapeutic mechanisms and clinical outcomes.
- REITHMEIER, T., LÖHR, M., PAKOS, P., KETTER, G. & ERNESTUS, R.-I. 2005. Relevance of ICP and ptiO₂ for indication and timing of decompressive craniectomy in patients with malignant brain edema. *Acta neurochirurgica*, 147, 947-952.
- REYNOLDS, D. V. 1969. Surgery in the rat during electrical analgesia induced by focal brain stimulation. *Science*, 164, 444-445.
- RICHARDSON, D. E. & AKIL, H. 1977. Pain reduction by electrical brain stimulation in man: Part 1: Acute administration in periaqueductal and periventricular sites. *Journal of neurosurgery*, 47, 178-183.
- ROSSI, U. 2003. The history of electrical stimulation of the nervous system for the control of pain. *PAIN RESEARCH AND CLINICAL MANAGEMENT*, 15, 5-16.
- RUSH, S. & DRISCOLL, D. A. 1968. Current distribution in the brain from surface electrodes. *Anesthesia & Analgesia*, 47, 717-723.
- RUSHTON, J. G. & ROOKE, E. D. 1962. Brain tumor headache. *Headache: The Journal of Head and Face Pain*, 2, 147-152.
- SADLEIR, R. J., VANNORSDALL, T. D., SCHRETLEN, D. J. & GORDON, B. 2010. Transcranial direct current stimulation (tDCS) in a realistic head model. *Neuroimage*, 51, 1310-1318.
- SAYPOL, J., ROTH, B., COHEN, L. & HALLETT, M. 1992. A theoretical comparison of electric and magnetic stimulation of the brain. *Annals of Biomedical Engineering*, 20, 495-495.
- SAYPOL, J. M., ROTH, B. J., COHEN, L. G. & HALLETT, M. 1991. A theoretical comparison of electric and magnetic stimulation of the brain. *Annals of biomedical engineering*, 19, 317-328.
- SCHACHTER, S. C. & SAPER, C. B. 1998. Vagus nerve stimulation. *Epilepsia*, 39, 677-686.
- SCHALLER, B. & RÜEGG, S. J. 2003. Brain tumor and seizures: pathophysiology and its implications for treatment revisited. *Epilepsia*, 44, 1223-1232.

- SCHNEIDERMAN, R. S., SHMUELI, E., KIRSON, E. D. & PALTI, Y. 2010. TFields alone and in combination with chemotherapeutic agents effectively reduce the viability of MDR cell sub-lines that over-express ABC transporters. *BMC cancer*, 10, 229.
- SCHOLZ, B. & ANDERSON, R. 2000. On electrical impedance scanning—principles and simulations. *Electromedica*, 68, 35-44.
- SEEGER, P. G. & WOLZ, S. 1992. *Successful biological control of cancer by combat against the causes*, Neuwieder Verlagsgesellschaft.
- SEIZURES.DOLYAN.COM. 2016. *Vagus Nerve Stimulation As A Treatment For Grand Mal Seizures* [Online]. <http://seizures.dolyan.com/>. Available: <http://seizures.dolyan.com/vagus-nerve-stimulation-as-a-treatment-for-grand-mal-seizures/> [Accessed 16.6 2016].
- SEM-JACOBSEN, C. 1966. Depth-electrographic observations related to Parkinson's disease. Recording and electrical stimulation in the area around the third ventricle. *Journal of neurosurgery*, 24, Suppl: 388-402.
- SERŠA, G., ČEMAŽAR, M., MIKLAVČIČ, D. & RUDOLF, Z. 2006. Electrochemotherapy of tumours. *Radiology and Oncology*, 40.
- SERSA, G. & MIKLAVCIC, D. 1993. The feasibility of low level direct current electrotherapy for regional cancer treatment. *Regional cancer treatment*, 6, 31-31.
- SHAHID, S., WEN, P. & AHFOCK, T. 2012. Effects of model complexity and tissue anisotropic conductivity on cortical modulation during transcranial direct current stimulation. *IET Science, Measurement & Technology*, 6, 464-473.
- SHAHID, S., WEN, P. & AHFOCK, T. 2013a. Assessment of electric field distribution in anisotropic cortical and subcortical regions under the influence of tDCS. *Bioelectromagnetics*.
- SHAHID, S., WEN, P. & AHFOCK, T. 2013b. Numerical investigation of white matter anisotropic conductivity in defining current distribution under tDCS. *Computer methods and programs in biomedicine*, 109, 48-64.
- SHAHID, S., WEN, P. & AHFOCK, T. 2014a. Assessment of electric field distribution in anisotropic cortical and subcortical regions under the influence of tDCS. *Bioelectromagnetics*, 35, 41-57.
- SHAHID, S., WEN, P., AHFOCK, T. & LEIS, J. 2011. Effects of head geometry, coil position and CSF displacement on field distribution under transcranial magnetic stimulation. *Journal of Medical Imaging and Health Informatics*, 1, 271-277.
- SHAHID, S. S., BIKSON, M., SALMAN, H., WEN, P. & AHFOCK, T. 2014b. The value and cost of complexity in predictive modelling: role of tissue anisotropic conductivity and fibre tracts in neuromodulation. *Journal of neural engineering*, 11, 036002.

- SHAHID, S. S., SONG, B., SALMAN, H., DE OLIVEIRA, M. M. & WEN, P. 2015. Use of electric field orientation as an index for estimating the contribution of model complexity in transcranial direct current stimulation forward head model development. *IET Science, Measurement & Technology*, 9, 596-605.
- SHAMMI, P. & STUSS, D. T. 1999. Humour appreciation: a role of the right frontal lobe. *Brain*, 122, 657-666.
- SHATTUCK, D. W. & LEAHY, R. M. 2002. BrainSuite: an automated cortical surface identification tool. *Medical image analysis*, 6, 129-142.
- SHORTER, E. & HEALY, D. 2007. *Shock therapy: a history of electroconvulsive treatment in mental illness*, Rutgers University Press.
- SIEGEL, R., MA, J., ZOU, Z. & JEMAL, A. 2014. Cancer statistics, 2014. *CA: a cancer journal for clinicians*, 64, 9-29.
- SIEGEL, R. L., MILLER, K. D. & JEMAL, A. 2016. Cancer statistics, 2016. *CA: a cancer journal for clinicians*, 66, 7-30.
- SILVA, G., MIKSAD, R., FREEDMAN, S. D., PASCUAL-LEONE, A., JAIN, S., GOMES, D. L., AMANCIO, E. J., BOGGIO, P. S., CORREA, C. F. & FREGNI, F. 2007. Treatment of cancer pain with noninvasive brain stimulation. *Journal of pain and symptom management*, 34, 342.
- SIRONI, V. A. 2011. Origin and evolution of deep brain stimulation. *The development of deep brain stimulation for neurological and psychiatric disorders: clinical, societal and ethical issues*, 4.
- SMITH, S. M., JENKINSON, M., WOOLRICH, M. W., BECKMANN, C. F., BEHRENS, T. E., JOHANSEN-BERG, H., BANNISTER, P. R., DE LUCA, M., DROBNJAK, I. & FLITNEY, D. E. 2004. Advances in functional and structural MR image analysis and implementation as FSL. *Neuroimage*, 23, S208-S219.
- SMITH, S. R., FOSTER, K. & WOLF, G. L. 1986. Dielectric properties of VX-2 carcinoma versus normal liver tissue. *Biomedical Engineering, IEEE Transactions on*, 522-524.
- SOCIETY, N. B. T. 2016. *Understanding Brain Tumors* [Online]. National Brain Tumor Society. Available: <http://braintumor.org/brain-tumor-information/understanding-brain-tumors/> [Accessed 31 May 2016].
- SONG, B., WEN, P., AHFOCK, T. & LI, Y. 2016a. Numeric Investigation of Brain Tumor Influence on the Current Distributions During Transcranial Direct Current Stimulation. *Biomedical Engineering, IEEE Transactions on*, 63, 176-187.
- SONG, B., WEN, P., AHFOCK, T. & LI, Y. 2016b. Numeric Investigation of Brain Tumor Influence on the Current Distributions During Transcranial Direct Current Stimulation. *IEEE Transactions on Biomedical Engineering*, 63, 176-187.

- SPIEGEL, E. A., WYCIS, H. T., MARKS, M. & LEE, A. J. 1947. Stereotaxic Apparatus for Operations on the Human Brain. *Science*, 106, 349-50.
- STAGG, C. J., BEST, J. G., STEPHENSON, M. C., O'SHEA, J., WYLEZINSKA, M., KINCSES, Z. T., MORRIS, P. G., MATTHEWS, P. M. & JOHANSEN-BERG, H. 2009. Polarity-sensitive modulation of cortical neurotransmitters by transcranial stimulation. *The Journal of neuroscience*, 29, 5202-5206.
- SUH, H. S., KIM, S. H., LEE, W. H. & KIM, T.-S. Realistic simulation of transcranial direct current stimulation via 3-D high-resolution finite element analysis: effect of tissue anisotropy. Engineering in Medicine and Biology Society, 2009. EMBC 2009. Annual International Conference of the IEEE, 2009. IEEE, 638-641.
- SUH, H. S., LEE, W. H. & KIM, T.-S. 2012. Influence of anisotropic conductivity in the skull and white matter on transcranial direct current stimulation via an anatomically realistic finite element head model. *Physics in medicine and biology*, 57, 6961.
- TANG, T., WEISS, M. D., BORUM, P., TUROVETS, S., TUCKER, D. & SADLEIR, R. 2016. In vivo quantification of intraventricular hemorrhage in a neonatal piglet model using an EEG-layout based electrical impedance tomography array. *Physiological measurement*, 37, 751.
- THARYAN, P. & ADAMS, C. E. 2005. Electroconvulsive therapy for schizophrenia. *The Cochrane Library*.
- THOMPSON, S. P. 1910. A physiological effect of an alternating magnetic field. *Proceedings of the Royal Society of London. Series B, Containing Papers of a Biological Character*, 82, 396-398.
- TOSONI, A., ERMANI, M. & BRANDES, A. A. 2004. The pathogenesis and treatment of brain metastases: a comprehensive review. *Critical reviews in oncology/hematology*, 52, 199-215.
- TRUONG, D. Q., MAGEROWSKI, G., BLACKBURN, G. L., BIKSON, M. & ALONSO-ALONSO, M. 2013. Computational modeling of transcranial direct current stimulation (tDCS) in obesity: impact of head fat and dose guidelines. *NeuroImage: Clinical*, 2, 759-766.
- UTZ, K. S., DIMOVA, V., OPPENLÄNDER, K. & KERKHOFF, G. 2010. Electrified minds: transcranial direct current stimulation (tDCS) and galvanic vestibular stimulation (GVS) as methods of non-invasive brain stimulation in neuropsychology—a review of current data and future implications. *Neuropsychologia*, 48, 2789-2810.
- VAN LIER, A., HOOGRUIN, J., POLDERS, D., BOER, V., HENDRIKSE, J., ROBE, P., WOERDEMAN, P., LAGENDIJK, J., LUIJTEN, P. & VAN DEN BERG, C. Electrical conductivity imaging of brain tumours. Proceedings of the 19th Annual Meeting of ISMRM, Montréal, Canada, 2011. 4464.
- VOIGT, T., VATERLEIN, O., STEHNING, C., KATSCHER, U. & FIEHLER, J. In vivo glioma characterization using MR conductivity imaging. Proceedings of the 19th

Scientific Meeting of the International Society of Magnetic Resonance in Medicine (ISMRM'11), 2011.

WAGNER, A., KRACH, W., SCHICHO, K., UNDT, G., PLODER, O. & EWERS, R. 2002. A 3-dimensional finite-element analysis investigating the biomechanical behavior of the mandible and plate osteosynthesis in cases of fractures of the condylar process. *Oral Surgery, Oral Medicine, Oral Pathology, Oral Radiology, and Endodontology*, 94, 678-686.

WAGNER, S., RAMPERSAD, S., AYDIN, Ü., VORWERK, J., OOSTENDORP, T., NEULING, T., HERRMANN, C., STEGEMAN, D. & WOLTERS, C. 2013. Investigation of tDCS volume conduction effects in a highly realistic head model. *Journal of neural engineering*, 11, 016002.

WAGNER, T., FREGNI, F., EDEN, U., RAMOS-ESTEBANEZ, C., GRODZINSKY, A., ZAHN, M. & PASCUAL-LEONE, A. 2006. Transcranial magnetic stimulation and stroke: a computer-based human model study. *Neuroimage*, 30, 857-870.

WAGNER, T., FREGNI, F., FECTEAU, S., GRODZINSKY, A., ZAHN, M. & PASCUAL-LEONE, A. 2007a. Transcranial direct current stimulation: a computer-based human model study. *Neuroimage*, 35, 1113-1124.

WAGNER, T., VALERO-CABRE, A. & PASCUAL-LEONE, A. 2007b. Noninvasive Human Brain Stimulation. *Annual Review of Biomedical Engineering*, 9, 527-565.

WARFIELD, S. K., KAUS, M., JOLESZ, F. A. & KIKINIS, R. 2000. Adaptive, template moderated, spatially varying statistical classification. *Medical image analysis*, 4, 43-55.

WASSERMANN, E. M. 1998. Risk and safety of repetitive transcranial magnetic stimulation: report and suggested guidelines from the International Workshop on the Safety of Repetitive Transcranial Magnetic Stimulation, June 5–7, 1996. *Electroencephalography and Clinical Neurophysiology/Evoked Potentials Section*, 108, 1-16.

WASSERMANN, E. M. & LISANBY, S. H. 2001. Therapeutic application of repetitive transcranial magnetic stimulation: a review. *Clinical Neurophysiology*, 112, 1367-1377.

WEAVER, L., WILLIAMS, R. & RUSH, S. 1976. Current density in bilateral and unilateral ECT. *Biological psychiatry*, 11, 303-312.

WEINER, R., LISANBY, S. H., HUSAIN, M. M., MORALES, O. G., MAIXNER, D. F., HALL, S. E., BEEGLY, J. & GREDEN, J. F. 2013. Electroconvulsive therapy device classification: response to FDA advisory panel hearing and recommendations. *The Journal of clinical psychiatry*, 74, 38-42.

WOLTERS, C., ANWANDER, A., TRICOCHÉ, X., WEINSTEIN, D., KOCH, M. & MACLEOD, R. 2006. Influence of tissue conductivity anisotropy on EEG/MEG field and return current computation in a realistic head model: a simulation and visualization study using high-resolution finite element modeling. *NeuroImage*, 30, 813-826.

REFERENCES

WOODBURY, D. M. & WOODBURY, J. W. 1990. Effects of vagal stimulation on experimentally induced seizures in rats. *Epilepsia*, 31, S7-S19.

WWW.ABOUTCANCER.COM. 2016. *MRI Images of Brain Mets* [Online]. Available: http://www.aboutcancer.com/brain_met_mri_2.htm 28 May].

ZABARA, J. Time course of seizure control to brief, repetitive stimuli. *Epilepsia*, 1985. LIPPINCOTT-RAVEN PUBL 227 EAST WASHINGTON SQ, PHILADELPHIA, PA 19106, 518-518.

ZAGO, S., FERRUCCI, R., FREGNI, F. & PRIORI, A. 2008. Bartholow, Sciamanna, Alberti: pioneers in the electrical stimulation of the exposed human cerebral cortex. *The Neuroscientist*, 14, 521-528.

ZHANG, X., LIU, J. & HE, B. 2013. Magnetic Resonance Based Electrical Properties Tomography: A Review.

ZITOVA, B. & FLUSSER, J. 2003. Image registration methods: a survey. *Image and vision computing*, 21, 977-1000.

ZLATESCU, M. C., TEHRANIYAZDI, A., SASAKI, H., MEGYESI, J. F., BETENSKY, R. A., LOUIS, D. N. & CAIRNCROSS, J. G. 2001. Tumor location and growth pattern correlate with genetic signature in oligodendroglial neoplasms. *Cancer research*, 61, 6713-6715.

ZOU, Y. & GUO, Z. 2003. A review of electrical impedance techniques for breast cancer detection. *Medical engineering & physics*, 25, 79-90.

トマ トン 124. 2010. *Electrode locations of International 10-20 system for EEG (electroencephalography) recording* [Online]. Wikipedia: wikipedia.org. Available: https://en.wikipedia.org/wiki/File:21_electrodes_of_International_10-20_system_for_EEG.svg [Accessed 5.6 2016].